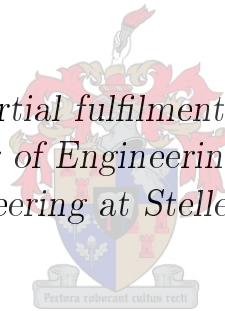# Effects of Modelling Simplifications in FEA of Railway Wheels

by

Jacobus Louwrens Cuperus

Thesis presented in partial fulfilment of the requirements for the degree of Master of Engineering (Mechanical) in the Faculty of Engineering at Stellenbosch University

Supervisor: Prof. G. Venter

March 2017

Declaration

By submitting this thesis electronically, I declare that the entirety of the work contained therein is my own, original work, that I am the sole author thereof (save to the extent explicitly otherwise stated), that reproduction and publication thereof by Stellenbosch University will not infringe any third party rights and that I have not previously in its entirety or in part submitted it for obtaining any qualification.

Signature: . . . .
                    J.L. Cuperus

                    March 2017
Date: . . . .

Abstract

Effects of Modelling Simplifications in FEA of Railway Wheels

J.L. Cuperus

Thesis: MEng (Mech)

March 2017

Typically, as part of the specifications outlining the requirements of railway wheels, the supplier must demonstrate through finite element analysis (FEA) that the design can withstand certain operational conditions and load cases. The specifications focused on in this study are the Transnet Freight Rail RS/ME/SP/008 specification for the supply of cast trailing stock wheels as well as the RS/ME/SP/021 specification for the supply of wrought wheels for tractive and trailing stock. These specifications contain a section pertaining to the finite element analysis of the wheel with respect to certain operational conditions. These conditions involve, however, complex interactions between loading and material non-linearities, superimposed onto a complex initial stress field. This stress field is laboriously obtained through a heat treatment schedule designed to induce compressive residual hoop stress in the rim of the wheel.

These complexities are ostensibly routinely ignored in the application of these (and similar) standards. This study aimed to provide some engineering and scientific reasoning to the simplification of these complex analyses in the future by investigating the effects of various assumptions and simplifications on the FEA.

The stress distribution of the normal contact loads are obtained through numerical simulation. The data is also used to derive a simple contact model for contact between two specific wheel and rail profiles.

Residual stresses of the new wheel was determined by simulating the heat treatment process. These models were also used to investigate the modelling details required to get accurate results from such a simulation by selectively applying various simplifications to the model.

The convective heat transfer to the atmosphere was investigated with computational fluid dynamic simulations and the data fitted to a non-dimensional heat transfer model. This data was then also compared to published heat

transfer models of simplified flow scenarios in order to determine if any of these is a viable option to determine heat transfer behaviour in the future.

Finally, all of the data gathered with the other analyses were used to determine the effect of various simplifications on the analysis as prescribed in the Transnet standards.

Uittreksel

Effekte van Modellering Vereenvoudigings in EEA van Spoorweg Wiele

("Effects of Modelling Simplifications in FEA of Railway Wheels")

J.L. Cuperus

Tesis: MIng (Meg)

Maart 2017

As deel van die spesifikasies waarin die vereistes van spoorweg wiele uitgelê word, word die verskaffer gewoonlik ook vereis om deur middel van eindige element analise (EEA) te demonstreer dat die ontwerp sekere operasionele omstandighede en las gevalle kan weerstaan. Die spesifikasies waarop hierdie studie fokus is die *Transnet Freight Rail* RS/ME/SP/008 spesifikasie vir die verskaffing van gegote wiele vir gesleepte voertuie asook die RS/ME/SP/021 spesifikasie vir die verskaffing van gesmeede wiele vir aangedrewe sowel as gesleepte voertuie. Hierdie spesifikasies bevat 'n seksie wat die eindige element analise van die wiel beskryf met betrekking tot sekere operasionele omstandighede. Hierdie toestande behels komplekse interaksies tussen die belasting en materiaal nie-lineariteit wat inwerk op 'n komplekse aanvanklike spanningsveld. Hierdie spanningsveld is moeisaam verkry deur 'n hitte behandeling skedule, ontwerp om druk hoepel resspanning te skep in die rand van die wiel.

Hierdie kompleksiteit word oënskynlik gereeld geïgnoreer in die toepassing van hierdie (en soortgelyke) standaarde. Hierdie studie is daarop gemik om ingenieurs- en wetenskaplike motivering te gee vir die toekomstige vereenvoudiging van hierdie komplekse analises deur die uitwerking van verskillende aannames en vereenvoudigings op die EEA te ondersoek.

Die druk verspreiding van die normaal kontak laste is verkry deur numeriese simulasie. Die data word ook gebruik om 'n eenvoudige kontak model af te lei vir kontak tussen twee spesifieke wiel en spoor profiele.

Resspanning van die nuwe wiel is bepaal deur die hitte behandeling proses te simuleer. Hierdie modelle is ook gebruik om die modellerings tegnieke wat nodig is om akkurate resultate van so 'n simulasie te kry, te ondersoek deur selektiewe vereenvoudigings op die model toe te pas.

Die konvektiewe hitte-oordrag na die atmosfeer is ondersoek met numeriese vloei dinamika simulasies en die data was op 'n nie-dimensionele hitte-oordrag model gepas. Hierdie data is dan ook vergelyk met gepubliseerde hitte-oordrag modelle van eenvoudige vloei gevalle ten einde vas te stel of enige van hierdie 'n werkbare opsie bied om hitte-oordrag in die toekoms te bepaal.

Ter afsluiting is al die versamelde data vanaf die ander analises gebruik om die effekte te bepaal van verskillende vereenvoudigings op die analises soos voorgeskryf in die Transnet standaarde.

Acknowledgements

I would like to sincerely thank Professor Gerhard Venter for his guidance and, above all else, his endless patience, which I have tested beyond any reasonable limit. Was it not for your management of my naïve exuberance, I certainly would not have succeeded in this endeavour.

I would furthermore like to thank Professor Neels Fourie and the PRASA Chair for maintenance and engineering management for funding and supporting this project. From the Chair, I would like to thank Pieter Conradie in particular for the assistance and support throughout.

Dedications

This thesis is dedicated to my parents for all of their sacrifices in the pursuit of my education and otherwise.

Contents

CONTENTS   xi

List of Figures

List of Tables

Chapter 1

Introduction

1.1   Project Background

In 2012, the Passenger Rail Agency of South Africa (PRASA) contracted the Department of Mechanical and Mechatronic Engineering of Stellenbosch University to perform the finite element analysis (FEA) portion of the validation of a new railway wheel. The validation was done according to the Transnet Freight Rail (TFR) RS/ME/SP/008 standard (Matjeke and Mabaso, 2011), typically used throughout South Africa for the evaluation of cast railway wheels. The section of interest to this study is also common to the TFR (formerly Spoornet) RS/ME/SP/021 standard (Spoornet, 1997) which applies to wrought wheels. It is similar to the UIC 510-5 (2003) (and by extension the BS EN 13979-1 (2011)). Some concerns were raised as to the open ended direction given by the standard as well as the common practices when these analyses are performed. Some assumptions and simplifications commonly seen are made due to economic and time constraints instead of scientific or engineering reasoning.

To suggest that economic and time constraints should not influence engineering projects would be naïve and/or disingenuous. However, it must be considered a priority to understand where and how one could save on limited resources in future projects without compromising the engineering outcomes and safety. This study aims to provide some technical background for this challenge in the future.

1.2   Test Standard Requirements

The TFR standard calls for two types of finite element analyses to be completed. The first is a static structural analysis, meant to simulate the contact loading between the wheel and rail. The second is structural/thermal analyses of two specified braking scenarios relating to wheels that are subjected to tread braking. It is meant to test whether the wheel will be able to withstand

the tremendous thermal load on the tread surface and the associated thermal stresses induced in the wheel.

1.3   Assumptions/Simplifications Investigated

The purpose of this research is to investigate some of the assumptions and simplifications commonly made during these evaluations of railway wheels with the purpose of establishing the effect of these simplifications and assumptions on the results. This information can then be used by analysts to evaluate whether it is necessary to commit the required effort and/or resources to obtain more representative boundary conditions or input data, given the desired outcomes of the analysis.

1.3.1   Wheel/Rail Contact

The contact loading as required by the TFR standard is investigated in Chapter 3. The Transnet standard provides very little direction as to how the contact loading should be applied. The locations are specified as points on the tread surface, leading some analysts to apply either point loads or arbitrarily defined contact patches and pressure distributions. Saint-Venant's principle states that at a sufficient distance from the applied load the difference between two statically equivalent loads become negligible. In other words, if the analyst is only interested in results far from the contact area, even the extreme simplification of a point load would be equivalent to the exact pressure distribution. On the other hand, it would be trivial to say that a point load would not be appropriate if rolling contact fatigue on the tread surface is of interest.

By using more representative contact loads to simulate the wheel/rail contact, the results will be acceptable and useful much closer to the applied loading and would provide more insight to the expected behaviour of the wheel. Importantly, it could allow the analyst to predict and avoid failure mechanisms in the wheel rim, which remains unsolicited in any wheel specification to my knowledge.

Since the fidelity of the contact load mostly determines how close to the contact patch the results remain of use, the focus was less on quantifying the error resulting from simplistic loads, but rather to make it easier to obtain realistic loads for future use. Contact between the wheel and rail was simulated using both the non-linear FEM as well as the boundary element method. The data was then fitted to a power law equation which can be used to obtain the contact parameters for contact between the same profiles for any realistic wheel diameter and load. The process is also outlined to allow future analysts to construct the same meta-model for other wheel and rail profile combinations.

1.3.2   Residual Stress

During the manufacturing of monobloc wheels, a great deal of effort goes into introducing compressive residual hoop stresses into the rim of the wheel. This compressive stress is an important factor in inhibiting the formation and propagation of any cracks in the rim, especially in the radial direction.

Residual stress is still widely ignored during FEA. To gauge the impact of ignoring the residual stress pattern, a representative stress field first needs to be obtained. Chapter 4 reports on the simulation of the heat treatment process (spray quenching of the tread) and the resultant residual stress field. During the process of obtaining the residual stress state, the important parameters and considerations for such an analysis are also investigated.

1.3.3   Heat Transfer Analysis

During braking analyses, the rate at which the thermal energy can be dissipated to the atmosphere may have a significant impact on the thermal stresses and maximum temperatures. It would be much more time and cost efficient to use known and established heat transfer models. The problem with this is that these heat transfer models are typically for idealised cases such as a flat plate in parallel flow.

In Chapter 5, a computational fluid dynamics (CFD) analysis is performed and used as a baseline to compare with established heat transfer models. The CFD data is also fitted to a non-dimensional heat transfer model which can be used to determine the heat transfer rates without repeating the simulations.

1.3.4   Evaluation of Different Assumptions and Simplifications

Chapter 6 investigates the effect of some of the common simplifications on the outcome of the TFR specification's simulations. First, the impact of various contact loads are investigated with respect to the peak equivalent stress. The main focus of the investigation focusses on the braking analyses. These analyses are done with various simplifications made to the thermal boundary conditions, two mechanical (load) variations and finally a number of simplifications to the material model.

1.4   External Publications

Chapter 3 was published in the Proceedings of the Institution of Mechanical Engineers, Part F: Journal of Rail and Rapid Transit (Cuperus and Venter, 2016b).

The work of Chapter 4 was presented at the 10th South African Conference on Computational and Applied Mechanics, held in Pothefstroom from 3-5 October 2016 (Cuperus and Venter, 2016a).

At the time of submission, an abstract relating to the work of Chapter 5 has been accepted to the 11th International Heavy Haul Association Conference to be held in Cape Town from 02 to 06 September 2017. The full paper is still to be submitted.

Chapter 2

Technical Background

2.1 Operational Environment of Railway Wheels

Railway wheels need to withstand tremendous contact stresses, guiding forces and retardation of the train. Most railway wheels are also subjected to tread applied braking. This means that the wheel is responsible for absorbing and dissipating the tremendous amount of thermal energy associated with braking.

Due to the obvious critical role of the wheel in the operation of a rail going vehicle, it is generally regarded as a priority by most operators to understand and avoid the failure mechanisms of railway wheels. Apart from wear and shallow rolling contact fatigue, the failure mechanisms are often catastrophic and can result in a derailment. As such, the wheels are generally subject to a host of technical specification, often relying heavily on physical testing. As already indicated, this study stems from the application of the numerical modelling section of one such specification.

2.2 Terminology and Operation of the Wheel and Rail

Figure 2.1 shows some of the terminology associated with the wheelset and the track. The main method through which a rail vehicle negotiates curves is with conicity of the wheel profile. In its simplest form, the wheel profile has a conical angle of γ. When the wheelset shifts laterally on the track, due to a curve, the outer wheel will have a larger rolling radius than the inside wheel. With both wheels being connected with a solid axle, the wheelset is then forced to roll in an arc. Contrary to popular believe, a rail vehicle does not negotiate curves purely due to the constraining action of the flange.

The rails are mounted to the sleeper at an angle, β, generally similar to the angle of conicity, γ. The sleeper then distributes the load of the train to

5
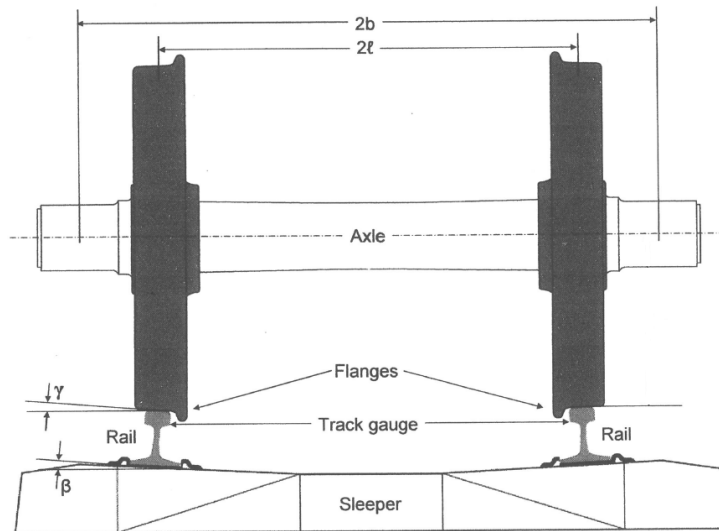
Figure 2.1: Wheelset on track (TFR Chair in Railway Engineering, 2015)

the supporting civil works.

Figures 2.2 and 2.3 show the different regions and parameters associated with a wheel and rail profile, respectively.
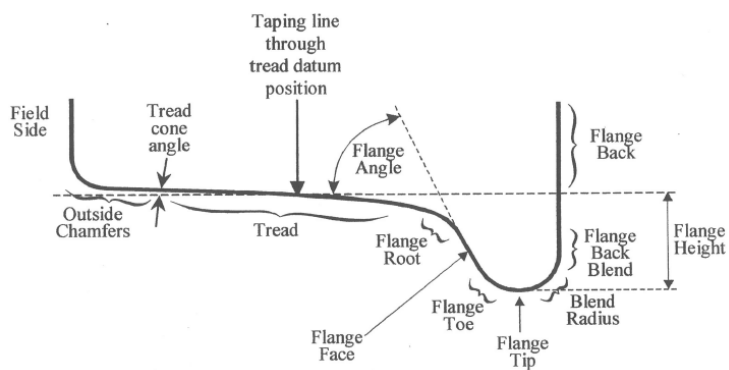
Figure 2.2: Wheel tread profile terminology (TFR Chair in Railway Engineering, 2015)
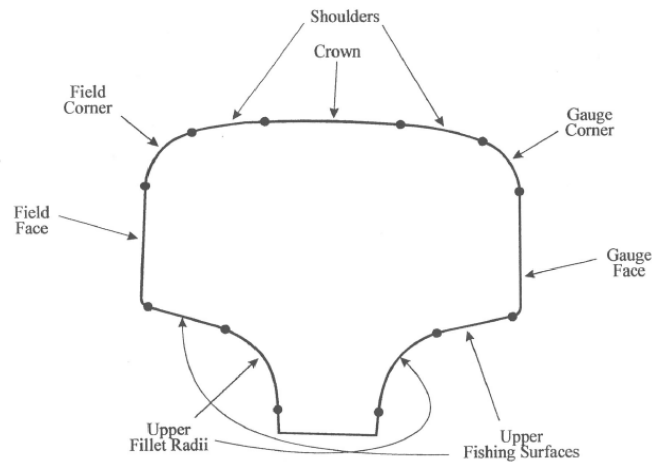
Figure 2.3: Rail head profile terminology (TFR Chair in Railway Engineering, 2015)

2.3 Railway Wheel Manufacturing

2.3.1 Wheel Types

Two types of railway wheels are in common use. The first is a tyred wheel where the outer rim area is shrink fitted to the wheel core. This design has the advantage that once the lower limit of the wheel diameter is reached, the tyre is simply replaced and the wheel is returned to service. The disadvantages of this configuration is that the heat of tread applied braking relaxes the interference and since the tyre is under tensile hoop stresses, cracks can propagate rapidly.

The other type is a monobloc (solid) wheel that can be either cast or forged. Once these wheels reach the minimum diameter (condemning limit) they are typically scrapped. Tyred wheels are largely being phased out in favour of monobloc wheels.

The different web configurations of the wheel can also broadly be grouped as either a straight web (Figure 2.4a) or an s-dish (Figure 2.4b). The main benefit of the s-dish design is its greater tolerance of the thermal load associated with severe brake applications. Figure 2.5 shows the relationship between the web offset and the peak thermal stress in the web as presented by Okagata (2013).

2.3.2 Quenching

During the manufacturing of monobloc wheels, they are typically subjected to a spray quenching process applied to the tread (see Figure 2.6). This is done, among other metallurgical reasons, to induce compressive residual hoop stress in the rim of the wheel. This acts as a preferential starting point for the tensile stresses that can be created by severe tread braking applications as well as the

(a) Straight web   (b) S-dish
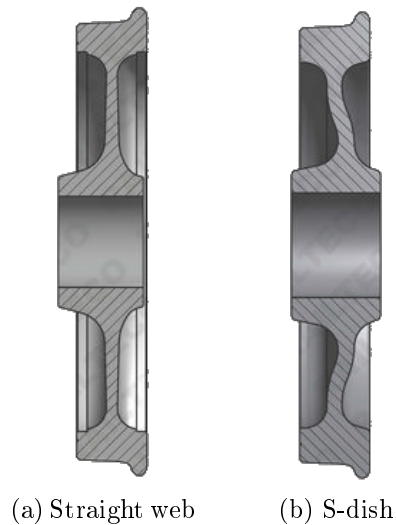
Figure 2.4: Railway wheel web configurations (Wheels World, 2012)

suppression of crack initiation and growth.

There exists a considerable body of research on heat transfer from a hot surface to a boiling fluid, as would be applicable to the tread surface during spray quenching. Nukiyama (1934) (translated to English in 1966) investigated the heat transfer from heated wires. Bromley (1950) investigated the heat transfer in the film boiling regime on both horizontal and vertical surfaces. Investigations into the heat transfer during spray quenching seem to have started in the late 1960's (Gaugler, 1966) and has been an active field to date (Aamir *et al.*, 2016; Guo *et al.*, 2016), with renewed interest for cooling of
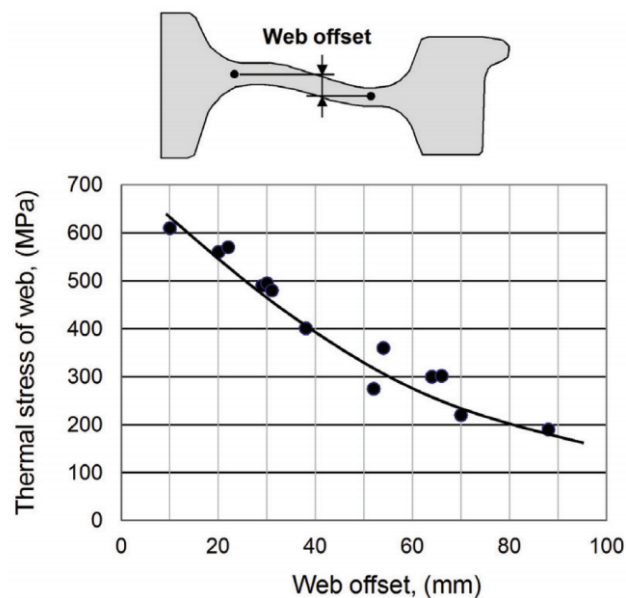
Figure 2.5: Effect of web offset on thermal stress (Okagata, 2013)

Figure 2.6: Spray quenching operation (MG-Valdunes, n.d.)

electronics (Cheng *et al.*, 2016).

When a hot surface is quenched, five distinct heat transfer regimes can be observed (see Figure 2.7). Starting from a sufficiently high temperature, the first regime is that of film boiling. During this regime the surface is covered by a vapour blanket which acts to restrict the heat transfer. As the temperature drops, the "departure from film boiling" point (point A) will be reached which separates the film boiling and film wetting regimes. The vapour blanket is now intermittent and partial liquid contact with the surface is established. Upon further cooling, the heat flux continues to decrease until the minimum heat flux point (point B) is reached, which separates the film wetting and transition boiling regions. During the transition boiling regime, a decrease in the surface temperature acts to increase the heat flux. Due to this positive feedback nature, this regime is typically very short lived. As the temperature continues to decrease, the point of maximum heat flux, or critical heat flux, (point C) is reached, which separates the transition and nucleate boiling regimes. As the surface cools down further, it enters the single-phase cooling regime (point D) (Hall *et al.*, 1997).

The heat transfer correlations used in this work was developed by the research group of Issam Mudawar. The model as reported in Hall *et al.* (1997) was used and is shown in Appendix D.

2.4   Wheel/Rail Contact

Two established approaches to solving the normal rail wheel contact problem will be briefly discussed. The first, and oldest, is the Hertz contact theory. The second is the software program known as CONTACT.
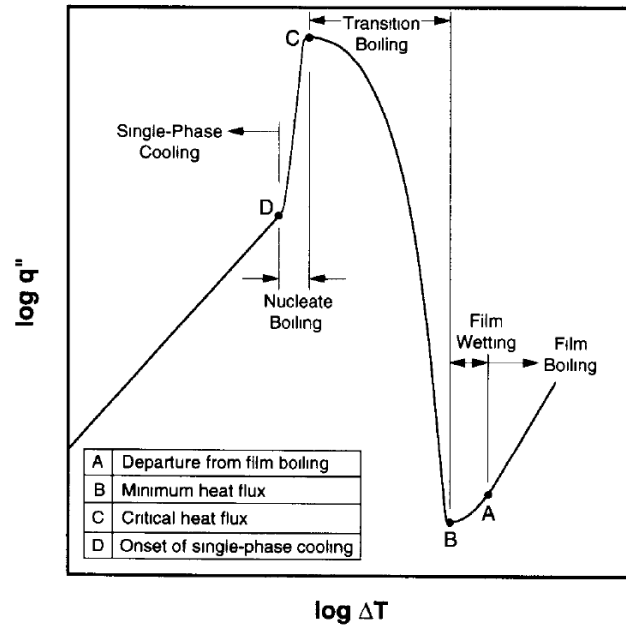
Figure 2.7: Boiling curve (Hall *et al.*, 1997)

2.4.1   Hertz Contact Theory

In 1881, Heinrich Hertz published his work on non-adhesive, non-conforming contact between two elastic bodies. This became the standard in evaluating common contact phenomena such as found in roller bearing, between two gears, and, of course, between railway wheels and the rails. Hertz's method employs the theory of potential to calculate the normal surface displacement of an infinite half-space due to pressure on the surface. The assumption that the elastic surface response of the contact geometries is that of an infinite body is much less restrictive than it might appear. Provided that the smallest geometric feature near the contact area is larger than the dimensions of the contact area, the assumption is deemed acceptable. In the field of wheel/rail interaction, this assumption is generally considered justified for contact away from the flange and flange root area.

In Hertzian contact theory, it is assumed that the surfaces of the contact geometries can be described with a quadratic function. The vertical (in the direction of loading) separation between the two contacting geometries is described by:

$$d(x, y) = Ax^2 + By^2 \tag{2.4.1}$$

A and B are referred to as the relative curvatures and are obtained by averaging the contact geometries' curvatures. They are mathematically defined as:

$$A = \frac{1}{2}\left(\frac{1}{R_{1x}} + \frac{1}{R_{2x}}\right), \quad B = \frac{1}{2}\left(\frac{1}{R_{1y}} + \frac{1}{R_{2y}}\right) \tag{2.4.2}$$

where the radii $(R_{\#\#})$ are the radii of contact body 1 and 2, respectively, in the x and y direction.

In order to calculate the contact patch dimensions, the Hertz coefficients (denoted m and n) need to be determined. The relevant coefficients from Ayasse and Chollet (2005) are shown in Table 2.1, where θ is obtained with:

$$\cos\left(\theta\right) = \frac{|B - A|}{B + A} \tag{2.4.3}$$

Table 2.1: Hertz coefficients

$\theta°$	0	5	10	30	60	90	120	150	170	175	180
m	∞	11.238	6.612	2.731	1.486	1	0.7171	0.4931	0.311	0.2381	0
n/m	0	0.0212	0.0470	0.1806	0.4826	1	2.0720	5.5380	21.26	47.20	∞

The contact patch dimensions can now be calculated as:

$$a = m\sqrt[3]{\frac{3Q\left(1 - \nu^2\right)}{2E\left(A + B\right)}}, \quad b = n\sqrt[3]{\frac{3Q\left(1 - \nu^2\right)}{2E\left(A + B\right)}} \tag{2.4.4}$$

where Q is the normal load, E the Young's modulus, and ν is the Poisson's ratio. Note that a and b represent the contact patch half-length and half-width instead of the full dimensions (see Figure 2.8). In the traditional Hertzian sense, a is taken as the greater of the two orthogonal dimensions. However, in the wheel/rail interaction context, it is customary to refer the dimension in direction of travel (length) as a and in the lateral direction (width) as b (see Figure 2.8).
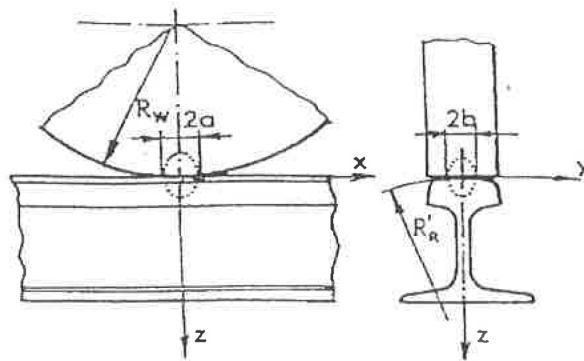
Figure 2.8: Hertzian contact patch dimensions (TFR Chair in Railway Engineering, 2015)

The pressure distribution over the contact patch is then given by:

$$P(x,y) = P_m \left[1 - \left(\frac{x}{a}\right)^2 - \left(\frac{y}{b}\right)^2 \right]^{1/2} \tag{2.4.5}$$

With the peak contact pressure:

$$P_m = \frac{3Q}{2\pi ab} \tag{2.4.6}$$

2.4.2 CONTACT

In 1926, Carter considered the effects of tangential forces transmitted through the contact area, particularly the effect of longitudinal traction forces. Carter solved the two-dimensional problem of longitudinal creep exactly and showed that for any finite traction force, the circumferential velocity is not equal to the translational velocity. Carter's two-dimensional theory was expanded to three dimensions to include lateral and spin creep through contributions by De Pater, Johnson, Vermeulen and Kalker (see Kalker (1991) for overview). Kalker spent most of his career on contact mechanics and developed many influential theories, models and computer programs to solve various aspects of the contact problem, including the program CONTACT (Vollebregt, 2013), which employs the boundary element method (BEM).

CONTACT solves the normal contact problem on a discretised surface using the boundary element method and minimisation of elastic strain energy, reformulated in terms of complementary energy (Kalker, 1982). This gives CONTACT the very important ability to solve non-Hertzian contact problems. CONTACT still employs the elastic half-space assumption, which is not necessarily acceptable in the flange root area.

Although the true power of CONTACT lies in its ability to solve the tangential contact problem, it is still a very powerful tool for the analysis of non-Hertzian (i.e., non-elliptical contact patch and/or non-ellipsoidal pressure distribution) normal contact situations.

2.5 TFR RS/ME/SP/008 Standard

The implementation of the finite element analysis (FEA) section of Transnet Freight Rail (TFR) specification RS/ME/SP/008 (Matjeke and Mabaso, 2011) is investigated in this project. This standard regulates the supply of cast wheels for trailing stock. The relevant section is identical to that in TFR (formerly Spoornet) specification RS/ME/SP/021 (Spoornet, 1997), which is aimed at wrought wheels for tractive and trailing stock. The Transnet standards are also similar to the UIC 510-5 (2003) (and by extension the BS EN 13979-1 (2011)) and similar in function at least to that of AAR S-660 (Association of American Railroads, 2009). The standard requires a "detailed stress analysis"

of the wheel design with the goal of providing the necessary information to predict the in-service behaviour of the wheel.

The standard does not indicate any criteria by which the wheel should be judged. This might seem curious at first, however, it does accord with the stated purpose of the FEA in the first place. According to the standard, the analysis "is for the purpose of evaluating the wheel design and not for rejection criteria of the wheel once the wheel design has been accepted". The standard does, however, state that the axial rim displacement as well as the change in residual stress of the rim should be reported.

The FEA section of the standard is broken up into two sections. The first is the mechanical load section, which deals with the contact loads. The second is the thermo-mechanical analysis which investigates the wheel's performance under two different braking scenarios.

2.5.1   Contact Loading

The standard prescribes three loading conditions utilising different combinations of four contact loads (see Figure 2.9). Load D is a 5-ton lateral load that should be combined with all three of the vertical loads. The vertical loads are 15 tons each. Load A is applied in the root of the wheel flange and represents the outside wheel in a curve. Load B is applied on the taping line of the wheel and represents the wheel travelling on tangent (straight) track. Load C is applied on the field side of the wheel, representing a load that can be encountered when the wheel is negotiating turn-outs.
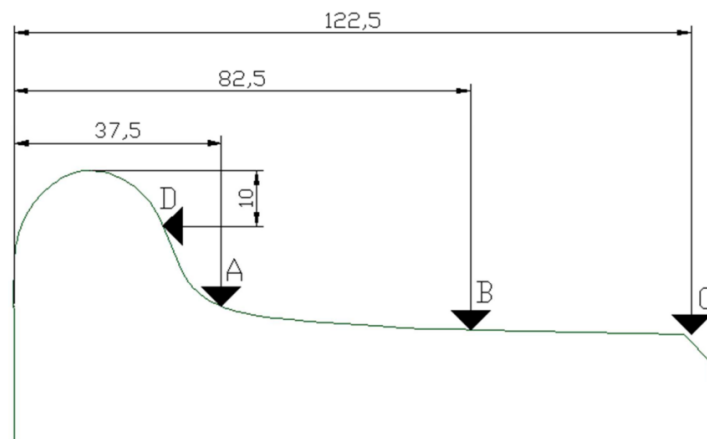
Figure 2.9: Contact locations. A: Flange root, B: Taping line, C: Field side, D: Flange lateral

One concern that lead to this project is the lack of detail in the directive for the contact loading. Among other things, the standard does not specify how the contact loading should be applied, leading some analysts to use loads

as primitive as point loads. Albeit the simplest way of applying the loading, it does render inaccurate any results close to the tread surface. Even though the contact can be simulated explicitly using non-linear finite element methods, it is a very expensive and technically challenging solution to the problem and would not be conducive to expedient investigations in the future. The first and possibly easiest response to this problem is to use Hertz's theory to determine the contact properties analytically. However, it is known that the contact is not necessarily Hertzian, especially for flange and flange root contact due to the invalid infinite half-space assumption. Notwithstanding its shortcomings, Hertzian contact is still an effective and fast solution if the accuracy of the contact stresses is not of great importance.

2.5.2 Thermal Loading

The thermal loading cases describe two different braking scenarios. The first is a drag-stop scenario where braking at constant speed (drag braking) takes place for a short period followed by constant deceleration to rest. The second is a drag braking case where the train is applying friction braking without a reduction in speed, typical of long descents.

2.5.2.1 Drag-Stop Braking

The first braking scenario consists of a 35 kW drag braking effort at 80 km/h for 10 minutes, followed by constant deceleration at 0.3 m/s^2, resulting in a 74 second deceleration period. It is stated that additional braking effort is required to effect the deceleration. Using the axle load limit of 18 tons, the additional braking power is calculated to be 60 kW. It is assumed that a constant braking torque is applied during the deceleration period. Braking power therefore reduces linearly from 95 kW to 0 kW at rest. Upon coming to rest, a cool-down period of 5 minutes is applied. This sequence is repeated six times for this test.

2.5.2.2 Drag Braking

Brake applications take place four consecutive times for 45 minutes each at a speed of 80 km/h, separated by 45 minutes of cooling periods at 80 km/h. The first brake application is at a rate of 20 kW with each subsequent application increasing with 10 kW.

2.6 Conclusion

This chapter discussed some basic and fundamental technical background to the railway wheel. More recondite aspects are discussed where relevant throughout the thesis.

Chapter 3

Normal Wheel/Rail Contact

3.1   Introduction

This chapter addresses the contact section of the prescribed finite element analyses. The contact is simulated at the four locations in Figure 2.9 using the non-linear finite element method (FEM). Locations A, B, and C are also investigated using the boundary element method (BEM). Furthermore, we demonstrate a method which can be used to set up a normal contact table, such as shown in Appendix A, for a specific wheel and rail profile combination. This table can then be used to quickly and easily calculate an equivalent Hertzian contact condition which can then be used in a finite element analysis (FEA). This should provide good quality results up to close proximity with the actual contact location, or even accurate approximations of the peak deviatoric stress beneath the contact.

As a test case for reducing the numerical load in future evaluations, the contact parameters for contact between a class 5M2A wheel with a TFR no. 22 wheel tread profile (Hettasch and Fröhling, 2011) and an SAR 57 rail (Suid-Afrikaanse Spoorpendelkorporasie Beperk, 2000) was calculated using CON-TACT and fitted to a multivariate power law equation (see Section 3.4). These empirical relationships can then be used in future to determine the normal contact parameters for contact between any wheel with a no. 22 wheel tread profile and an SAR 57 rail profile more accurately than from Hertzian theory, with simpler calculations requiring less information.

Finite element analyses were done both for validation of the boundary element method results as well as to obtain results in the areas where the boundary element method is not advised. The technical challenges with regard to finite element simulations are discussed as it is a very useful tool for analysing complex contact cases. Contact induced plasticity was also briefly explored. For the parametric study, boundary element simulations were used because of the reduced computational cost of obtaining the large amount of data needed. Finally, the equivalent Hertzian contact method is briefly

discussed in view of its applicability to use the empirical correlations here obtained in future work.

3.2 Finite Element Analysis

The contact problem was solved at all four locations as specified for contact both over a sleeper and midway between two sleepers. The analyses were performed using MSC Marc with the material properties set out in Table 3.1. The material data in Table 3.1 is for the class 5M2A wheel from data of the Pasanger Rail Agency of South Africa (PRASA Rail Chair for Maintenance and Engineering Management, 2012) and was also used for the rail material. Analyses with plasticity were merely done to gain qualitative insights into the effect of plasticity; hence simple bilinear plasticity and perfect plastic models were used.

Table 3.1: Wheel properties

Description	Value
Young's Modulus (E)	205 GPa
Poison's Ratio (ν)	0.29
Yield Stress (σ_y)	600 MPa
Tangent Modulus (E_T)	14 GPa
Taping Line Radius (R_T)	0.4315 m

3.2.1 Finite Element Mesh

The mesh was constructed in 2D using predominately four node quadrilateral elements and then extruded or revolved to create hexahedron elements forming the rail and wheel respectively. This was done to avoid the poor performance of constant strain tetrahedrons and the force reversal problems associated with higher order elements in contact.

Mesh density was controlled by defining different regions that were meshed independently and then glued together (see Figure 3.1). Elements in the contact area were created with a nominal edge length of 1 mm in order to capture the contact characteristics at a sufficient resolution (mesh convergence was also established). In the area close to the flange root, it was however found that the mesh resolution was still too coarse, especially at location D in Figure 2.9. The mesh resolution in the flange root area was addressed using dynamic mesh refinement.

Four models were considered. A distinction was drawn between contact over and between sleepers as well as contact in and away from the flange and

(a) Wheel 2D mesh

(b) Rail 2D mesh

(c) Inter-sleeper complete model

(d) Contact region
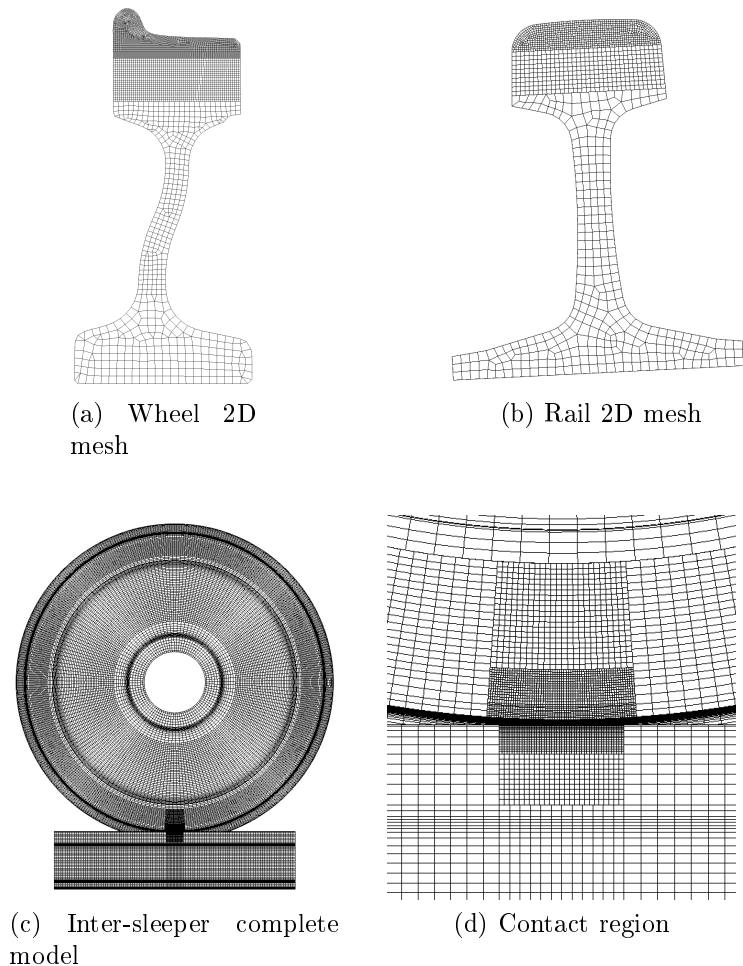
Figure 3.1: Finite element mesh

flange root area. For contact at location A and D, dynamic mesh refinement was used on both the wheel and rail. To ensure the linear interpolation of the mesh refinement does not distort the contact profile, and therefore the contact stresses, the newly created surface nodes were associated with a geometric surface of the tread profile.

For inter-sleeper contact outside of the flange root area, the model had 842 712 elements and 918 503 nodes. The model for contact over the sleeper and outside the flange root area had 894 334 elements and 979 029 nodes. Inter-sleeper contact at positions A and D had around 1.3 million elements and 1.45 million nodes at the end of the simulation. Contact over the sleeper at positions A and D had around 1.45 million elements with 1.6 million nodes at the end of the simulation.

The contact problem is very stiff in that small displacements in the contact zone produce very high stresses. The model is thus extremely sensitive to the accuracy of the nodal coordinates. This problem was encountered with the

wheel mesh which was produced by revolution. Initial simulations produced spurious contact stress distributions as shown in Figure 3.2a. In order to fix the nodal coordinates, the surface nodes were projected onto a geometric surface of the tread profile (see Figure 3.2b).

(a) Pre-projection

(b) Post-projection
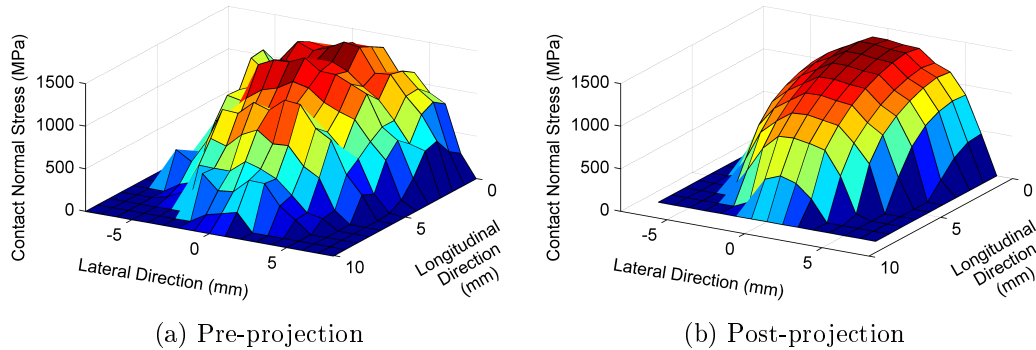
Figure 3.2: Normal contact stress profiles showing the effect of nodal coordinate inaccuracies

3.2.2   Finite Element Boundary Conditions
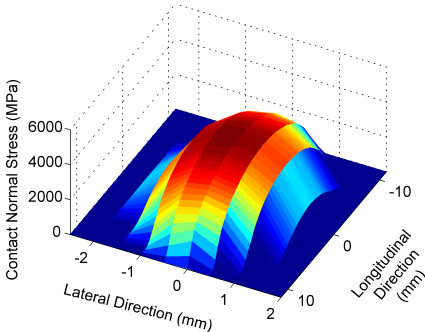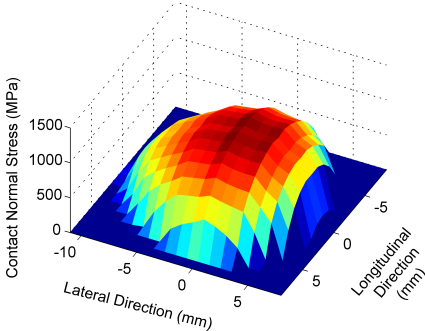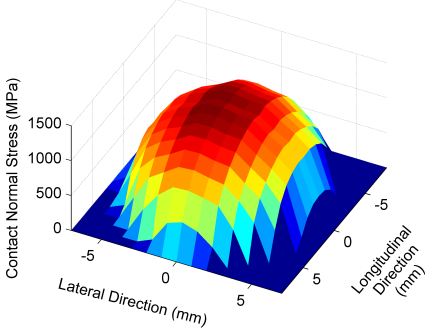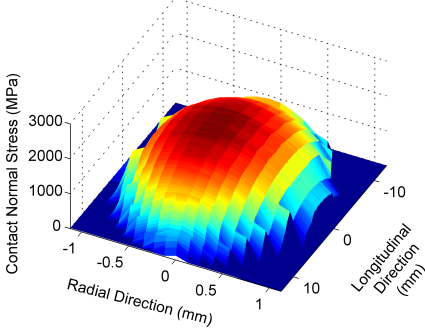
All nodes on the inside surface of the wheel hub were constrained in the two directions orthogonal to the loading direction. The load was applied to the same nodes on the inside of the hub. The rail was constrained at the locations of the tie-downs, 700 mm apart over a width of 200 mm (100 mm for rail sectioned over the sleeper). For contact over the sleeper, the rail spanned two gaps and for contact between sleepers only one span was used. A symmetry boundary condition was applied to the ends of the rail. Only normal contact is considered, as such the contact is approximated as frictionless. Including friction in the finite element analysis does not seem to have a marked effect on the stress state.

3.2.3   Finite Element Results

Tables 3.2 and 3.3 show the results obtained from the finite element simulations. Plastic deformation is only expected close to the contact location and the rail is not expected to deform plastically due to bending between sleepers under normal conditions. Due to long solving times, plasticity was therefore only included for analyses of contact over a sleeper.

It is well known that a large component of the contact stress is in fact hydrostatic, allowing contact stresses far in excess of the material's yield stress (Vasauskas *et al.*, 2005). It is also well established that, for normal loading, the peak deviatoric stress occurs below the surface (Johnson, 1989). In Figure 3.3, the surface shows the periphery of the volume where von Mises stress exceeds
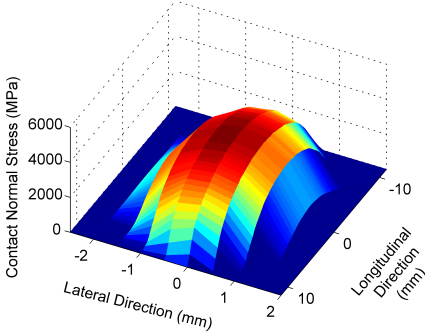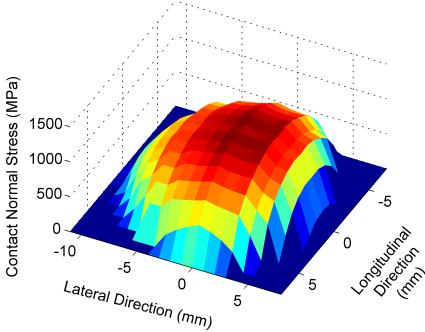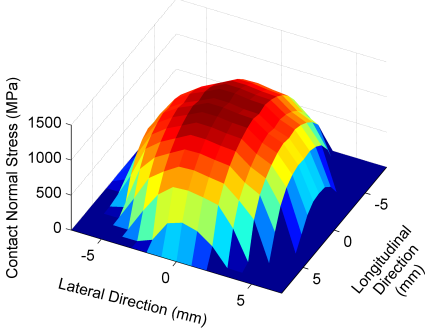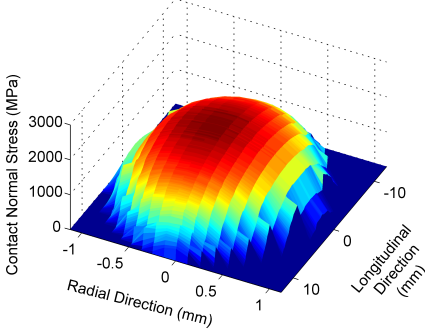
Table 3.2: Finite element results between sleepers

Load Case	Contact Stress Profile	Elastic Contact Properties
Flange Root (Fig. 2.9: A)		Max. Stress = 4 055 MPa $2a = 23$ mm $2b = 4.5$ mm
Taping Line (Fig. 2.9: B)		Max. Stress = 1 170 MPa $2a = 17$ mm $2b = 19$ mm
Field Side (Fig. 2.9: C)		Max. Stress = 1 408 MPa $2a = 17$ mm $2b = 14$ mm
Flange Lateral Contact (Fig. 2.9: D)		Max. Stress = 2 060 MPa $2a = 26.125$ mm $2b = 2.25$ mm

Where $2a$ is the contact patch length in the rolling direction
and $2b$ is the contact patch width in the lateral direction.

Table 3.3: Finite element results over sleeper

Load Case	Contact Stress Profile	Contact Properties
Flange Root (Fig. 2.9: A)		**Elastic** Max. Stress = 4 103 MPa $2a = 23$ mm $2b = 4.5$ mm **Plastic** Max. Stress = 2 259 MPa $2a = 26.5$ mm $2b = 5.25$ mm
Taping Line (Fig. 2.9: B)		**Elastic** Max. Stress = 1 166 MPa $2a = 15$ mm $2b = 19$ mm **Plastic** Max. Stress = 1 111 MPa $2a = 16$ mm $2b = 19$ mm
Field Side (Fig. 2.9: C)		**Elastic** Max. Stress = 1 403 MPa $2a = 17$ mm $2b = 14$ mm **Plastic** Max. Stress = 1 217 MPa $2a = 18$ mm $2b = 14$ mm
Flange Lateral Contact (Fig. 2.9: D)		**Elastic** Max. Stress = 2 042 MPa $2a = 26$ mm $2b = 2.25$ mm **Plastic** Max. Stress = 1 480 MPa $2a = 27$ mm $2b = 2.7$ mm

Where $2a$ is the contact patch length in the rolling direction
and $2b$ is the contact patch width in the lateral direction.

the yield stress (600 MPa). Figure 3.3 shows that for contact outside the flange root area, the plastic zone is completely surrounded by elastic material, thus acting to restrict plastic strains to very low levels (see Table 3.4). Table 3.4 also shows that outside of the flange root area, there is not much difference in the plastic strains between cases where no work hardening was considered (perfect plastic) and for a tangent modulus of 14 GPa. This suggests that the work hardening characteristics of the steel have very little effect on the equilibrium state and that high fidelity plasticity data are not needed in cases where the plastic zone is fully contained within elastic material.

(a) Flange root (location A)	(b) Taping line (location B)
(c) Field side (location C)	(d) Flange lateral (location D)
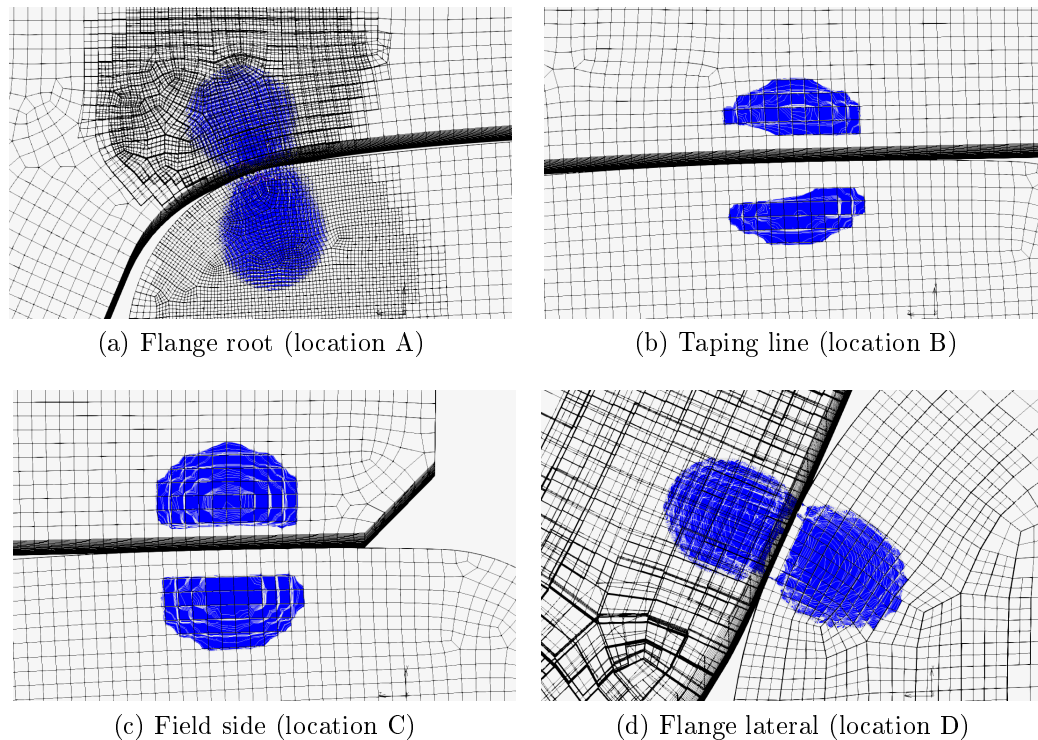
Figure 3.3: 600 MPa von Mises stress boundary indicating the boundary between elastic/plastic behaviour

3.3   Boundary Element Method

The normal contact problem was then solved using the program CONTACT by VORtech computing. This program solves the normal contact problem on a discretised surface using the boundary element method and minimisation of elastic strain energy, reformulated in terms of complementary energy (Kalker, 1982). This gives CONTACT the very important ability to solve non-Hertzian

Table 3.4: Plastic behaviour

Load Case	Plasticity	Peak Contact Stress (MPa)	$\epsilon_p(10^{-3})$	ϵ_p/ϵ_Y
Flange Root	$E_T = 14$ GPa	2 259	18.75	6.406
	Perfect Plastic	1 789	34.87	11.91
Taping Line	$E_T = 14$ GPa	1 111	0.861	0.294
	Perfect Plastic	1 096	1.039	0.355
Field Side	$E_T = 14$ GPa	1 217	2.108	0.72
	Perfect Plastic	1 188	2.414	0.825
Flange Lateral	$E_T = 14$ GPa	1 480	6.91	2.36
	Perfect Plastic	1 387	9.04	3.09

Where E_T is the tangent modulus of the material,
ϵ_p is the plastic strain,
and ϵ_Y is the yield strain of the material.

contact problems. CONTACT still employs the elastic half-space assumption, which is not necessarily acceptable in the flange root area.

3.3.1 Preparatory Calculations

A track based coordinate system was used. For each lateral displacement of the wheelset relative to the track, the wheel profile had to be transformed to the track based coordinate system by adding the necessary shift in the lateral direction. The wheel and rail profiles were then interpolated to common lateral positions in order to find the minimum separation. Finally, the distance between the axis of rotation and the contact patch in the direction normal to the contact plane (termed effective rolling radius) is required. Using basic trigonometry it can be shown that:

$$R' = \frac{R_0}{cos(\delta)} \tag{3.3.1}$$

where R' is the effective rolling radius, R_0 represents the wheel radius at contact location, δ is the angle between surface normal and the vertical (contact angle).

3.3.2 BEM/FEM Cross Validation

Because of the difficulty of validating the numerical models with physical testing, numerical cross validation between the FEM and BEM was done instead. The two different methods were used to solve the normal contact

Table 3.5: Graphic comparison of FEM and BEM results (in MPa)

Load Case	FEM	BEM
Flange Root Contact		
Taping Line Contact		
Field Side Contact		
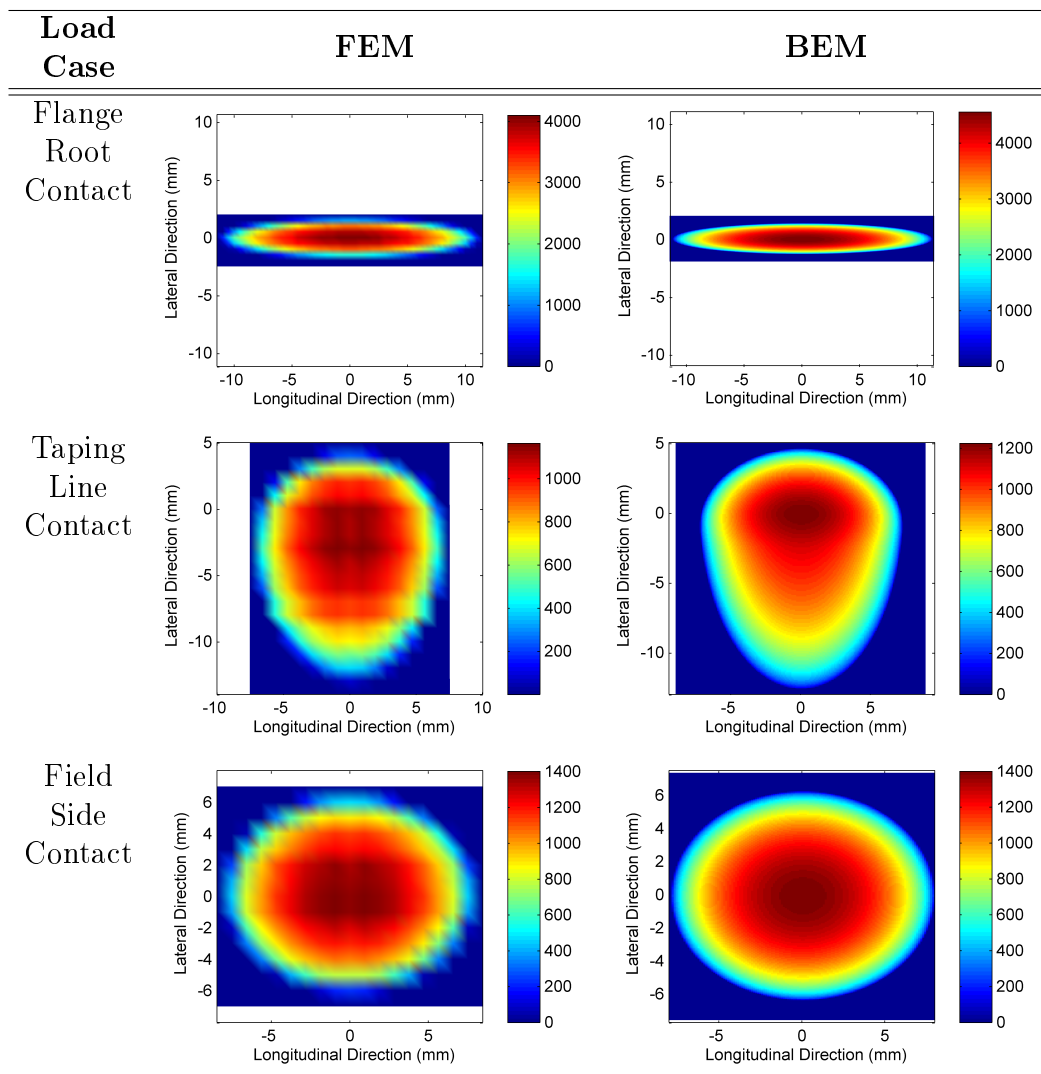
problem for the three vertical loads of Figure 2.9 and is also compared to Hertz's theory. Lateral loading cases were not considered with the CONTACT simulations because the infinite half-space assumption is known *a priori* to be invalid.

The graphic comparison in Table 3.5 shows very good agreement in the size and shape of the contact patch between the two methods. Table 3.6 suggests a good correlation with just under 5% difference (using FEM as reference) in peak stress, except in the flange root area (13.26% difference) where the boundary element method is not advisable because of the infinite half-space assumption.

It can be seen that the major advantage of the BEM solution over that of Hertz is the ability of the BEM to resolve more complex geometries by

Table 3.6: Quantitative comparison of FEM, BEM, and Hertzian results

Load Case	FEM	BEM	Hertz's Theory
Flange Root	Max. Stress = 4 103 MPa $2a = 23$ mm $2b = 4.5$ mm	Max. Stress = 4 647 MPa $2a = 22.7$ mm $2b = 2.7$ mm	Max. Stress = 4 357 MPa $2a = 21.9$ mm $2b = 2.94$ mm
Taping Line	Max. Stress = 1 166 MPa $2a = 15$ mm $2b = 19$ mm	Max. Stress = 1 223 MPa $2a = 14.5$ mm $2b = 17.1$ mm	Max. Stress = 1 397 MPa $2a = 16$ mm $2b = 12.6$ mm
Field Side	Max. Stress = 1 403 MPa $2a = 17$ mm $2b = 14$ mm	Max. Stress = 1 339 MPa $2a = 15.8$ mm $2b = 12.5$ mm	Max. Stress = 1 397 MPa $2a = 16$ mm $2b = 12.6$ mm

using numerically defined separation between the two bodies. This becomes apparent at the taping line where a radius of 450 mm meets the linear taper of the outer region of the wheel. For Hertzian calculations, the analyst is faced with a decision of whether to base the calculations on the linear region or the curved region, with the former offering the conservative solution.

3.4 Parametric Study

Instead of limiting the investigation to contact locations in Figure 2.9, the parametric investigation entailed executing hundreds of CONTACT simulations for different wheel radii and normal loads over a common range of lateral displacements of the wheelset relative to the track. CONTACT was used for both the reduced computational cost (26.5 seconds for all three vertical loads of Figure 2.9 versus 18 834 seconds with FEM) as well as easier data extraction.

3.4.1 CONTACT Simulations

Figure 3.4 shows the contact position on the wheel for the range of lateral displacements. The large jump in contact position from 42.72 mm to 63.57 mm (indicated by the squares in Figure 3.4) is due to the mismatch between a small 70 mm radius section on the wheel and the 305 mm radius of the rail profile.

For the nominal load and wheel radius, any lateral displacement between 4 and 6 mm (taking positive displacement as moving the wheel flange closer to the rail) results in two point contact at the respective locations. As expected, an increase in normal load and a decrease in wheel diameter acts to increase the range over which the two point contact occurs. The lateral displacement then acts to distribute the load between the two points.

Due to the appreciable difference in wheel radius at these different contact locations creep forces and wear will be high. This will most likely eliminate the conditions causing the two point contact fairly quickly in the service life
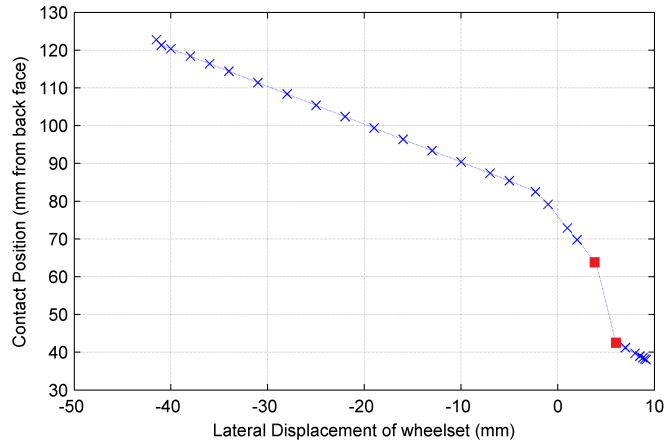
Figure 3.4: Contact position for lateral displacement range.

of the rail and wheel. Any researcher interested in contact within this range is advised to simulate it explicitly, especially since the applicability of the BEM is questionable for contact on the flange side of this two-point area. If necessary, a single equivalent contact condition can be established using the method described by Pascal and Sauvage (1992). From Pascal and Sauvage it can also be seen that the load distribution between the two contact locations vary nearly linearly with lateral wheelset displacement (except when the wheel goes into a flanging condition). Contact parameters can then be calculated for each contact location using the empirical formulations and the load carried by each contact patch.

From correlations derived using Hertzian theory, it can be seen that the contact parameters follow a power law correlation with the normal load, wheel diameter, and Young's modulus (see Johnson (1982) as example). In this case Young's modulus is treated as a constant with a value of 205 GPa. To establish how the contact characteristics (half-length, half-width, area, and peak stress) react to changes in the wheel diameter and vertical load, 36 simulations were executed for each contact location of the lateral displacement range using a dense six by six design of experiments with respect to normal load and wheel radius. The response for all parameters under consideration at a specific contact position were assumed to follow the form:

$$Y = mQ^{n_1}R^{n_2} \tag{3.4.1}$$

where Q is the vertical load, R is the taping line radius, m represents the coefficient of proportionality while n_1 and n_2 are the sensitivity exponents

A least-squares fit was then done to fit the simulation results to this equation. The coefficient and exponents to equation 3.4.1 for the test case can be found in Table A.1 in Appendix A. Figure 3.5 shows (for the nominal load case) the comparison between the length, width, area, and peak contact stress from the boundary element method and the recalculated results using

Table A.1. Equation 3.4.1 seems well suited to the problem at hand, producing a maximum fitting error of 4.5% (not for the nominal case shown in Figure 3.5). The only locations where any error exceeds 1% are for contact at the flange side of the two-point contact, and at the field side of the wheel where the contact patch starts to depart from the running surface of the wheel. Both of these locations then have geometric features that force the contact to react differently to how it does normally.

(a) Contact length (a)

(b) Contact width (b)

(c) Contact area (A)

(d) Peak contact stress (P_m)
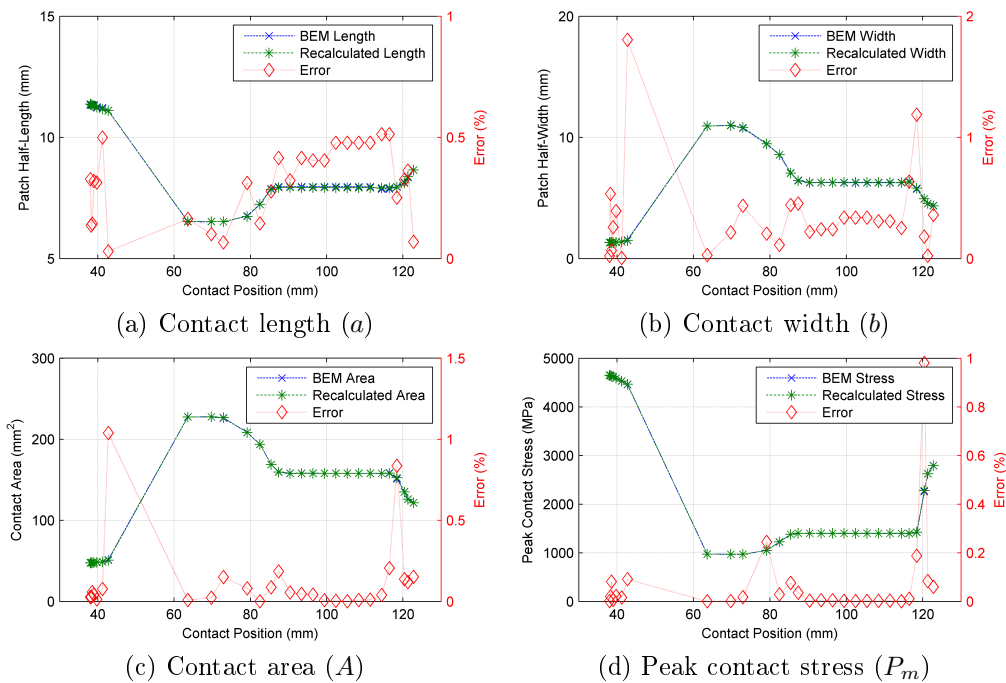
Figure 3.5: Contact parameters of nominal load case

3.4.2 Equivalent Hertzian Load

Using the non-Hertzian results from the boundary element solutions for an FEA or other work can be difficult if the exact contact area and pressure distribution are to be replicated. The numerical results would have to be used as produced by the simulations and scaled for wheel radius and normal load in question. This is rarely practical. Common practice of dealing with non-Hertzian loading is to define an equivalent Hertzian load instead; i.e., an elliptic contact patch with semi-ellipsoidal normal pressure distribution. To ensure equivalence, the contact area of the equivalent ellipse must be the same as the actual contact area and the length to width ratio of the contact patches must be equal (Piotrowski and Kik, 2008). It is also possible to use the original peak contact stress while changing the contact area to ensure the same normal load, or using both the original contact area and peak contact stress which

results in a different normal load. The normal contact stress is then defined as in equation 2.4.5 and 2.4.6.

Figure 3.6 shows, for the nominal load case, the error involved in approximating the original contact condition with an equivalent Hertzian representation. The last three contact positions show the contact patch reaching the edge of the tread profile and encountering a small geometric anomaly at the end of the linear taper region. As can be seen in Figure 3.6a, this geometric anomaly causes a sharp increase in the peak contact stress.

(a) Original area and normal load

(b) Original peak stress and normal load

(c) Original area and peak stress
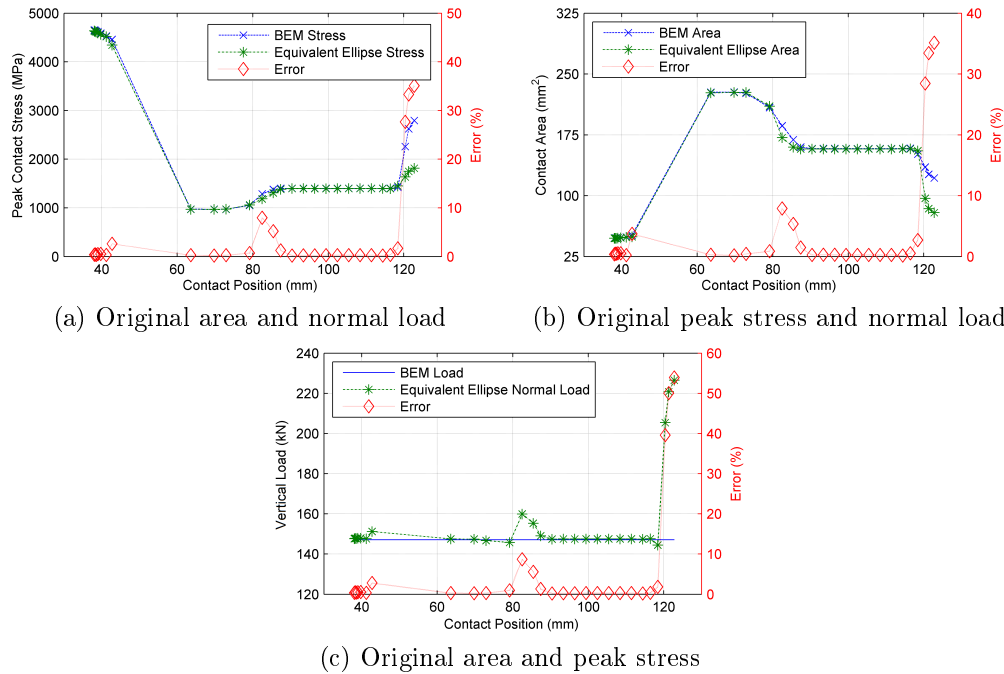
Figure 3.6: Accuracy of equivalent Hertzian contact

Considering equation 3.4.1, the theoretical Hertzian values for n_1 are 1/3 for the geometric half-lengths and contact pressure, and 2/3 for the contact area. The theoretical value for n_2 is dependent on the aspect ratio of the contact patch and therefore would also be a function of the contact position. The regions showing appreciable errors from the equivalent Hertzian approximation are also where the value of n_1 tends to deviate from the theoretical Hertzian value, indicating the non Hertzian nature of the profiles in those areas.

The largest errors, excluding the last three contact positions, are shown in Table 3.7. These errors occur on the taping line where the curved tread found on the flange side meets the linear taper of the outer region. Theoretically the errors for the two methods where the original load is maintained should be exactly the same, with the third one only different due to the base effect of the load deviating in the opposite direction than the stress and area. The difference

Table 3.7: Equivalent Hertz errors

Method	Error (%)
Original Area and Normal Load	8.88
Original Peak Stress and Normal Load	8.63
Original Area and Peak Stress	9.60

in errors observed here is due to the errors of the data fitting operation also affecting the accuracy of the final equivalent Hertzian contact.

Given that the error involved in the equivalent Hertzian approximation is strongly influenced by the contact location, it would be reasonable to expect that the maximum errors would also be very dependent on the specific profiles involved. Vollebregt *et al.* (2011) found much larger discrepancies between the peak contact stresses of CONTACT and an equivalent Hertzian description. It is, however, important to note that Vollebregt *et al.* compared the CONTACT results with an equivalent Hertzian description of a contact solution obtained with an interpenetration method rather than with CONTACT.

As long as the two contacting bodies have similar elastic properties and the elastic half-space assumption holds, the normal problem is independent of the tangential problem (Kalker, 1990). This enables the results obtained from this parametric investigation to be used regardless of the tangential contact conditions. The tangential contact problem can simply be superimposed onto the normal contact problem solved with the current method. The ellipticised normal contact can also be used with Kalker's simplified theory (Kalker, 1973) to solve the tangential problem. This would have the advantage of being much faster than the complex, but more accurate, CONTACT algorithm. According to Kalker (1991), ellipticised contact works well with the simplified theory, especially when the solution is sought for use in vehicle dynamics simulations.

3.5 Conclusion

The work presented in this chapter attempted to find simple boundary conditions that can account for wheel-rail normal contact in finite element analyses without the need for gross assumptions or simulating the contact explicitly. For a case study, the contact between a class 5M2A wheel with a Transnet Freight Rail no. 22 wheel profile and an SAR 57 rail was simulated using both non-linear finite element methods (MSC Marc) and the boundary element method (CONTACT) for the contact conditions described in Transnet Freight Rail specification RS/ME/SP/008. This served as a cross validation of the two methods and provided finite element results for the lateral flange contact, which was not investigated with CONTACT.

To provide more general boundary conditions between the no. 22 wheel

profile and the SAR 57 rail profile, the contact was simulated in CONTACT for a range of wheel diameters and normal loads at 28 locations. The contact length, width, area, and peak contact stress were fitted to power law equations which can be used to determine an equivalent elliptical contact for use in finite element analyses. The maximum error with the equivalent elliptical contact (excluding one area with a geometric anomaly) is 9.6% with respect to the normal load if both the original area and peak stress are maintained.

Chapter 4

Heat Treatment Simulation

4.1   Introduction

As part of the manufacturing process, a lot of effort goes into inducing the desired residual stress pattern to the wheel. However, due to the difficulty of including phase transformation effects and the need for material data that are typically not available, standards and specifications usually do not explicitly require that the initial residual stress field be taken into account (BS EN 13979-1, 2011; UIC 510-5, 2003; Matjeke and Mabaso, 2011). Consequently, many analysts ignore the initial residual stress pattern when finite element analyses are performed, even when fatigue and final residual stress fields are investigated (Portesi *et al.*, 2005; Ha and Kang, 2012). To ascertain the effect of this simplification, a complete residual stress state first needs to be obtained to include in a finite element model as an initial state.

The only standard for the evaluation of railway wheels that explicitly requires that the residual stress field be determined (as far as the author is aware) is the AAR S-669 standard (Association of American Railroads, 2011). AAR S-699, however, only explicitly requires that viscoelastic creep be taken into account when the residual stress simulation is performed. This leaves room for considerable simplification of the analysis, with possible detrimental effects on the fidelity of the results.

In this chapter, tread quenching is simulated on a class 5M2A wheel using MSC Marc. By running various simulations - taking different boundary conditions and metallurgical effects into account - the parameters and physical phenomena that are important to consider during these simulations, and those that can be ignored in future, are established.

In order to predict the residual stress state through simulating the heat treatment process, a comprehensive material model, that covers the entire temperature range of the process, is required. As this material data is not available for the wheel in question, and constitutes a prohibitively vast undertaking (within the scope of this project) to obtain experimentally, published material

data were used instead. Since the purpose of this study is to determine how sensitive the model is to various parameters and metallurgical phenomena and to obtain a representative (or plausible) residual stress field for further work, only a representative material model is required.

4.2 Simulation Parameters

The simulations were performed with MSC Marc, using the heat treatment process as well as particular material properties from Gordon and Perlman (1998), in which a commuter car wheel was analysed. The wheel starts at a uniform initial temperature of 870 °C, at which point the entire wheel is assumed to be fully austenised. A water spray tread quenching operation is then applied for two minutes. This is followed by a four minute dwell at room temperature during which the wheel is handled between operations. The four minute dwell is followed by a sub-critical annealing stage at 500 °C for 5 hours, after which the entire microstructure is assumed to be pearlite. Finally, the wheel is left to cool to room temperature, taken as 25 °C.

Accounting for all the interactions pertinent to the heat treatment process is a very complex simulation problem that is a current research topic (see Ariza *et al.* (2014); Song *et al.* (2014), for example). See Mackerle (2003) for an extensive bibliography covering 25 years.

For the purposes of this discussion, material data are divided into general material data and data accounting for the effects of phase transformation. Most of the major technical challenges in this work were associated with the effects of phase transformation.

4.2.1 General Material Data

From Gordon and Perlman (1998), the thermal properties of the material are shown in Table 4.1, with the mechanical properties in Table 4.2. The material model from Gordon and Perlman was used as it was the only source that covered the entire temperature range for the relevant material parameters. It was not possible to establish how similar the material is to the wheel being simulated, other than it also being a railway wheel. As stated before, only a representative or plausible material model is required given the goal of the study.

Note that the specific heat capacity and the coefficient of thermal expansion (CTE) from Gordon and Perlman were not used for the nominal case, but only to investigate the results of omitting transformation effects. Specific heat capacity and CTE data for the nominal case (which takes all phase transformation effects into account) are discussed in Section 4.2.2.

Table 4.1: Thermal material properties for railway wheel from Gordon and Perlman (1998)

Temp (°C)	Specific Heat c_p (J/kg.K)	Thermal Conductivity (W/m.K)
0	419.5	59.71
350	629.5	40.88
703	744.5	30.21
704	652.9	30.18
710	653.2	30.00
800	657.7	25.00
950	665.2	27.05
1200	677.3	30.46

Table 4.2: Mechanical material oroperties for railway wheel from Gordon and Perlman (1998)

Temp (°C)	Young's Modulus E (GPa)	Poisson's Ratio ν	Yield Stress σ_y (MPa)	Tangent Modulus E_T (GPa)	Tangent CTE α (µm/m.K)
24	213	0.295	422.9	21.66	5.3
230	201	0.307	424.7	25.73	8.81
358	193	0.314	366.7	20.29	10.25
452	172	0.320	291.0	14.89	10.95
567	102	0.326	132.3	5.93	11.38
704	50	0.334	39.4	0.92	11.3
900	43	0.345	11.7	0.085	11.25

A simple bilinear strain hardening model is used. The Young's modulus describes the stress-strain relationship for any stress less than the yield stress, while the tangent modulus is applicable for any stress equal to the yield stress.

Due to the high temperature and the presence of a sub-critical annealing stage, it is clear that material creep could have a marked effect on the residual stress field. This was investigated and confirmed by Kuhlman *et al.* (1988) by performing finite element analyses on a 40 inch railway wheel. As the creep data for the wheel material in question is not available, the material creep as given by Kuhlman *et al.* (also used by Gordon and Perlman) was used. Kuhlman's viscoelastic creep strain (rate) equation was converted to metric units to obtain:

$$\dot{\varepsilon} = 1.5305(10^{-93})\sigma_{eq}^{12.5}e^{\left(\frac{-29840}{T+273}\right)} \tag{4.2.1}$$

with the equivalent stress (σ_{eq}) in Pascal and the temperature (T) in degrees

Celsius.

4.2.2 Material Property Dependence on Phase Transformation

Modelling the phase transformations is a complex problem that can rarely be performed with the pre-defined options in non-linear finite element packages. Figure 4.1 shows the general interactions during phase changing heat treatment. Since the microstructure is not of interest, it would be preferable to artificially account for the effects of phase transformation. This is simplified in the current study by the fact that the final phase of the steel throughout the wheel is known to be pearlite (PRASA Rail Chair for Maintenance and Engineering Management, 2012).
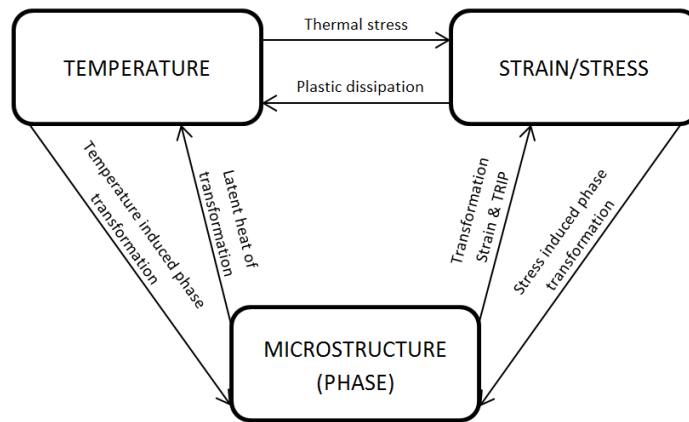
Figure 4.1: Metallo-thermo-mechanical coupling

4.2.2.1 Latent Heat of Phase Transformation

The latent heat of transformation can be accounted for in the specific heat capacity of the material. The drawback to this approach is that it is not possible to account for the changes in the temperature range over which the transformation takes place as a result of supercooling or the stress in the component. The temperature dependent specific heat capacity accounting for austenite to pearlite transformation of eutectoid (1078) steel from ASM International (1990), also used by Kuhlman *et al.* (1988), was used and is shown in Table 4.3. Here the specific heat capacity is given as the average value over a temperature range. To avoid numerical instabilities, the latent heat was ramped up and down as shown in Figure 4.2a.

Table 4.3: Specific heat of eutectoid (1078) steel (ASM International , 1990)

Temp (°C)	Specific Heat c_p (J/kg.K)
50-100	490
150-200	532
200-250	548
250-300	565
300-350	586
350-400	607
450-500	670
550-600	712
650-700	770
700-750	2081
750-800	615

4.2.2.2   Phase Transformation Induced Strains

During phase transformations, the incremental strain $d\varepsilon_{ij}$ can be broken down as:

$$d\varepsilon_{ij} = d\varepsilon_{ij}^e + d\varepsilon_{ij}^p + d\varepsilon_{ij}^{th} + d\varepsilon_{ij}^{pt} + d\varepsilon_{ij}^{trip} \tag{4.2.2}$$

where ε_{ij}^e is the elastic strain, ε_{ij}^p the plastic strain, ε_{ij}^{th} the thermal strain, ε_{ij}^{pt} the phase transformation strain, and ε_{ij}^{trip} is the transformation induced plasticity (TRIP).

The first of the transformation induced strains, the phase transformation strain, is driven by a difference in the specific volume of the parent and product phases. Thus it is a purely spherical (isotropic) strain tensor. Similarly to the latent heat of transformation, this transformation induced change in volume (as a result of crystal structure alone) can be included by modifying the coefficient of thermal expansion, as this too is a spherical tensor. According to Lement (1959), the change in volume (percent) from the face-centred cubic (FCC) structure of austenite to pearlite, a combination of body-centred cubic (BCC) ferrite and orthorhombic cementite, at 20 °C (based on measured lattice parameters) is:

$$\triangle V\% = (4.64 - 2.21 \times \%C)\,\% \tag{4.2.3}$$

where $\%C$ denotes the percentage carbon content.

As equation 4.2.3 is only valid at 20 °C, and the austenite to pearlite transformation takes place at a much higher temperature, the equation is modified in order to take into account the different thermal expansion coefficients of austenite and pearlite. Using the temperature invariant CTE values for

austenite and pearlite, respectively, by Jung *et al.* (2012), $\alpha_A = 24$ µm/m.K and $\alpha_P = 15$ µm/m.K, it is possible to extrapolate the change in volume given by equation 4.2.3 to another desired temperature. For this extrapolation, the same temperature range over which the phase transformation is captured in the specific heat capacity data (as indicated by the spike between 700 and 750 °C) is used. The transformation induced volume change was calculated for the middle of this range (725 °C) and then converted from a volume change to an equivalent linear dimensional change. This relationship between volume and linear expansion is typically approximated as:

$$\triangle V \approx 3 \triangle L \qquad\qquad (4.2.4)$$

This change in length was then superimposed onto the conventional coefficient of thermal expansion. The resultant CTE as a function of temperature is shown in Figure 4.2b. To avoid numerical instabilities owing to discontinuities at both 700 and 750 °C, linear ramps were used instead of an even distribution. The temperature invariant coefficients of thermal expansion by Jung *et al.* are used for all analyses accounting for transformation effects rather than that of Gordon and Perlman (given in Table 4.2) as the data by Gordon and Perlman do not distinguish between the different microstructures. Between 700 and 750 °C, the conventional CTE value was taken as the average of that of austenite and pearlite.

(a) Specific heat capacity   (b) Coefficient of thermal expansion
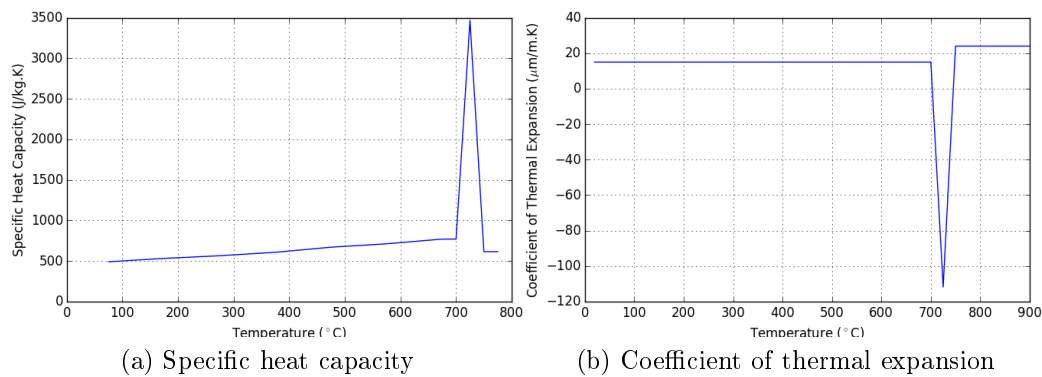
Figure 4.2:   Modifications to specific heat and CTE to account for transformation effects

The second of the transformation induced strains, TRIP, is the inelastic deformation at a low stress state (below the yield stress) during the phase transformation and is a traceless tensor. Two mechanisms for TRIP have been put forward and are both widely accepted. The first is known as the Greenwood-Johnson (1965) effect. As already stated, the parent and product phases have different specific volumes and as such there is a change of volume associated with the phase transformation. This volume change can quickly

cause the softer material, typically the austenite in the case of steel, to yield in order to accommodate the change in volume. This is particularly true for diffusive transformations where the transformation starts at a nucleation site and propagates outwards, yielding the surrounding austenite matrix. The second mechanism is known as the Magee effect and is only associated with displacive transformations. As such, it is not of interest in this work as the product phase is pearlite. The interested reader is directed to the bibliography by Mackerle (2003).

The TRIP model used in this work was developed by Leblond over four publications (Leblond *et al.*, 1986*a*,*b*, 1989; Leblond, 1989). It is itself broken up into three terms, with the incremental strains proportional to the stress increment, temperature increment, and product phase fraction increment, respectively. Written as rate of change:

$$\dot{\varepsilon}^{trip} = \dot{\varepsilon}(\dot{\sigma}_{eq}) + \dot{\varepsilon}(\dot{T}) + \dot{\varepsilon}(\dot{z}) \tag{4.2.5}$$

where σ_{eq} is the equivalent stress, T is the temperature, and z is the phase fraction of the product phase. For the detailed models covering different material strain hardening models, see Appendix B.

Similar to Simsir and Gür (2008), TRIP was calculated in Marc's ANEXP (anisotropic thermal expansion) user subroutine, adding the traceless TRIP strain tensor to the spherical thermal strain tensor. Given the material data available, some approximations had to be made to use LeBlond's models. Firstly, phase transformation was assumed to take place at a constant rate from 750 to 700 °C. The global (macroscopic average of all phases) yield stress and strain hardening characteristics are based on the data given in Table 4.2 at the current temperature and sum of plastic strain and TRIP strain. The yield stress and strain hardening characteristics of austenite were approximated as that of the global material (given in Table 4.2) at 750 °C throughout the entire transformation period.

During the transformation, all or most of the strain hardening accumulated in the austeninte is lost. For this reason it is acceptable to include TRIP into the thermal strain tensor as most, if not all, of the plasticity is confined to the austenite matrix. As the temperature at an integration point passes through a pre-set temperature, the plastic strain tensor as well as equivalent plastic strain scalar are reset to zero. Marc's NEWSV (new state variable) user subroutine was used to set the temperature at which plasticity is to be reset. Once the plasticity at a particular integration point is reset, the state variable for that integration point is changed to an unattainably low temperature to ensure that it is only reset once.

The Fortran codes to calculate the TRIP strain as well as reset the plastic strain information are shown in Appendix C.

4.2.3 Finite Element Mesh & Boundary Conditions

As with the contact simulations, a fine mesh was used in order to obtain a high resolution and not for the purpose of mesh convergence. An axisymmetric mesh (Figure 4.3) with 5 327 elements and 16 616 nodes was used.
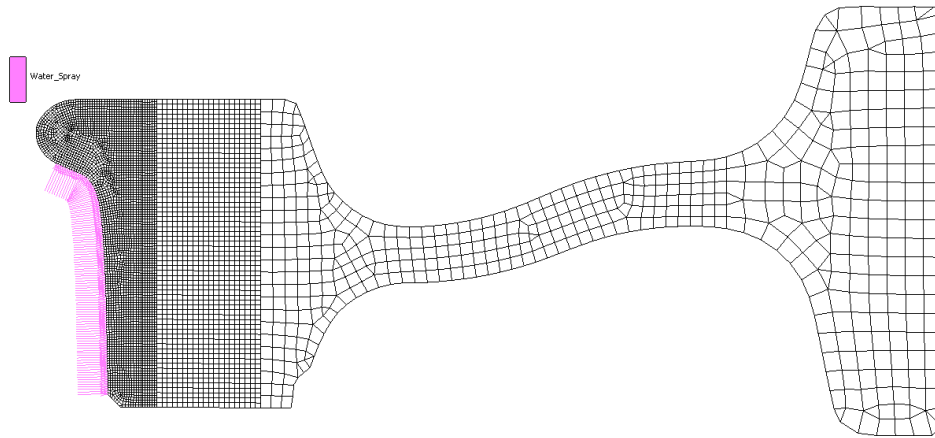
Figure 4.3: Axisymmetric mesh

The heat transfer coefficients (HTC) from Kuhlman *et al.* (1988) were used. Quenching was applied using a convection coefficient of 3066 W/m^2.K and water temperature of 23 °C (see Figure 4.3 for quenching area). Natural convection was implemented in the remaining wheel surface with a convection coefficient of 28 W/m^2.K and an ambient temperature of 25 °C. Radiation was included using an emissivity of $\varepsilon = 0.81$ (Çengel and Ghajar (1998)) to space at the relevant ambient temperature for the stage in the heat treatment process.

The constant heat transfer coefficient of Kuhlman *et al.* was thought to potentially be a primitive approximation of the actual heat transfer, warranting more detailed investigation. The boundary condition representing the spray quenching was then also calculated using the model published by Mudawar's group, specifically the one reported by Hall *et al.* (1997). These correlations can be found in Appendix D.

The spray characteristics used during the rim quenching of the wheel used in this study are not known as the information is proprietary. The spray characteristics used for the simulations were chosen such that they do not violate the limitations of the published heat transfer correlations while extracting roughly the same amount of thermal energy during the quenching process as the temperature invariant HTC by Kuhlman *et al.*. The spray properties are shown in Table 4.4. The resultant temperature dependent heat transfer coefficient is shown in Figure 4.4. No radiation was applied to the sprayed surface during the quenching stage as radiation was not accounted for during the studies of Mudawar's group or Kuhlman *et al.*

Table 4.4: Spray properties

Description	Value
Mean drop velocity U_m	20 m.s^{-1}
Sauter mean diameter d_{32}	7.44(10^4) m
Volumetric spray flux Q''	9(10^3) m^{3}s^{-1}m^{-2}
Thermal conductivity k_f	0.679 W.m^{-1}K^{-1}
Dynamic viscosity μ_f	282(10^{-6}) kg.m^{-1}s^{-1}
Fluid density ρ_f	957.9 kg.m^{-3}
Steam density ρ_g	0.5978 kg.m^{-3}
Heat of vaporisation h_{fg}	2 257 kJ.kg^{-1}
Surface tension σ	58.9(10^{-3}) N.m^{-1}
Specific heat C_p	4 217 J.kg^{-1}.K^{-1}
Subcooling $\triangle T_{sub}$	77 °C
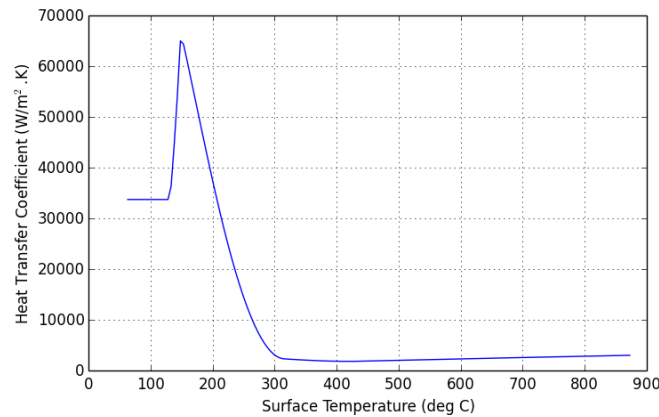
Figure 4.4: Spray quenching heat transfer coefficient

4.3   Sensitivity to Material Parameters and Boundary Conditions

The axisymmetric model is used to investigate variations in parameters relating to material behaviour, phase transformations and boundary conditions (summarised in Table 4.5). Since one of the major objectives of the heat treatment is to induce residual compressive hoop stress in the rim of the wheel, it is used as the metric to judge the effect of the various changes.

The nominal (reference) case in this study uses kinematic hardening and takes all transformation effects into account. These include transformation strain, transformation induced plasticity, latent heat of transformation, and the loss of strain hardening during phase transformation. The heat generated by plastic deformation is also taken into account. The quenching heat transfer is calculated using the work by Mudawar's group and radiation is included on all surfaces being cooled by natural convection. The resultant residual stress

Table 4.5: Model parameter configuration

Case	Hardening Law	Creep Model	Latent Heat	Transf. Strain	TRIP Strain	Plastic Heat	Radiation	Quench HTC
Isotropic	isotropic	incl.	incl.	incl.	incl.	incl.	incl.	Mudawar
Kinematic (Nominal)	kinematic	incl.	incl.	incl.	incl.	incl.	incl.	Mudawar
No Creep	kinematic	omtd	incl.	incl.	incl.	incl.	incl.	Mudawar
Perfect Plastic	N/A	incl.	incl.	incl.	incl.	incl.	incl.	Mudawar
No Transf. Strain	kinematic	incl.	incl.	omtd	omtd	incl.	incl.	Mudawar
No Transf. Heat	kinematic	incl.	omtd	incl.	incl.	incl.	incl.	Mudawar
No TRIP	kinematic	incl.	incl.	incl.	omtd	incl.	incl.	Mudawar
No Transf. Kinetics	kinematic	incl.	omtd	omtd	omtd	incl.	incl.	Mudawar
No Radiation	kinematic	incl.	incl.	incl.	incl.	incl.	omtd	Mudawar
Constant HTC	kinematic	incl.	incl.	incl.	incl.	incl.	incl.	Kuhlman
No Plastic Heat	kinematic	incl.	incl.	incl.	incl.	omtd	incl.	Mudawar

incl.: included
omtd: omitted

field is shown in Figure 4.5.

On the material side, isotropic and kinematic hardening models are compared. Isotropic hardening is faster to solve, most likely due to the delay in reverse plasticity as the wheel returns to a uniform temperature after the quench. For the remaining simulations, kinematic hardening is used since Kuhlman *et al.* (1988) and Rammerstorfer *et al.* (1981) reported it to be more representative. The effect of omitting creep as well as strain hardening is also investigated.

To investigate the various transformation effects, a number of combinations of model parameters are considered, as summarised in Table 4.5. The transformation strain is ignored (as well as the transformation induced plasticity as it is caused by the transformation strain) by using the temperature dependent thermal expansion coefficient of Gordon and Perlman (given in Table 4.2) which does not include transformation effects. This temperature dependent CTE is also compared to a constant CTE (taken as 12 µm/m.K rather than 15 µm/m.K as given by Jung *et al.* to better match the data by Gordon and Perlman). This is done in order to gauge the importance of the temperature dependence since constant values were used to construct the CTE accounting for phase transformation. The latent heat of transformation is also excluded by using the specific heat capacity from Gordon and Perlman (given in Table 4.1).

(a) Circumferential stress

(b) Axial stress

(c) Radial stress
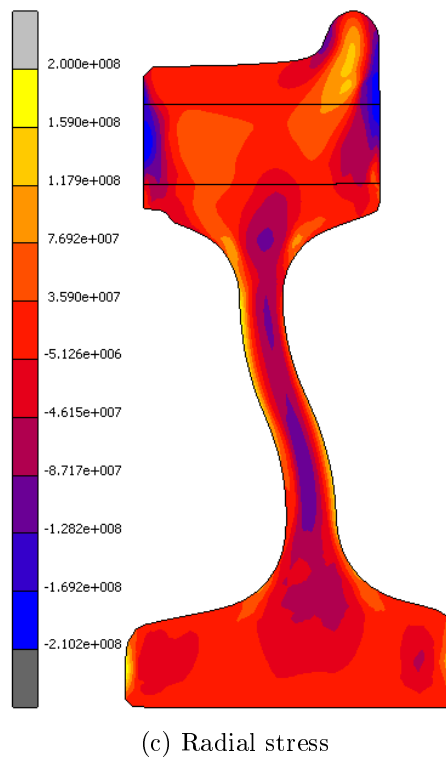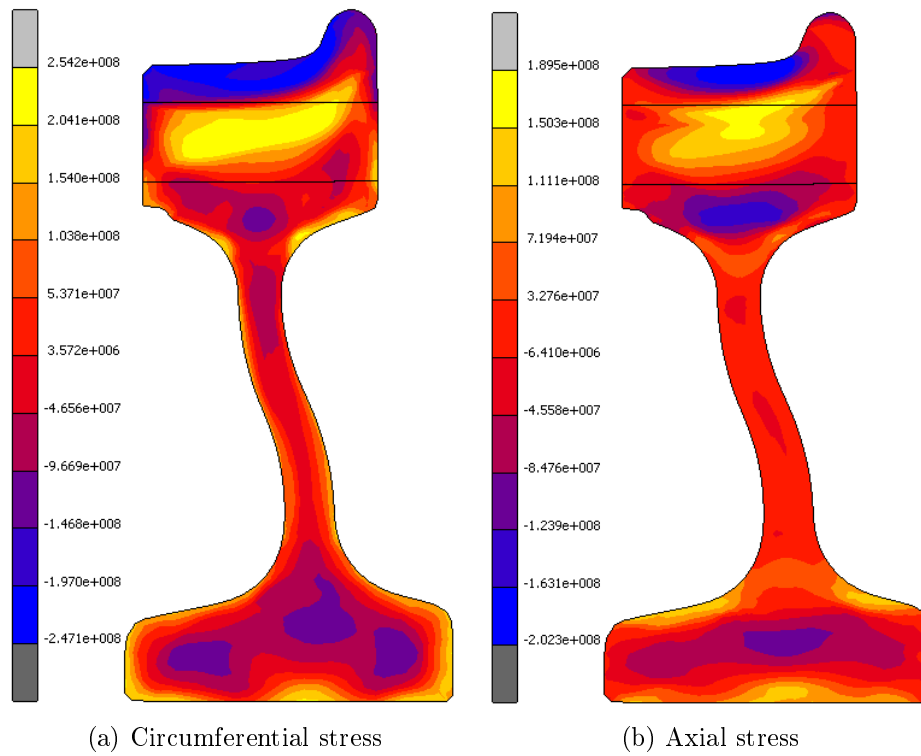
Figure 4.5: Residual stress for nominal case (Units in Pa)

Transformation induced plasticity is then omitted while still including the volumetric transformation strain and the latent heat of phase transformation. Finally all transformation effects are ignored simultaneously.

Different boundary conditions are also investigated. Radiative heat transfer is excluded. The effect of approximating the spray quenching process with a constant HTC is investigated by using the value used by Kuhlman *et al.* The heat generated by plastic deformation is also excluded.

Figure 4.6 shows the hoop stress along a line from the tread surface on the taping line, extending 63 mm radially down into the rim. Figure 4.6c excludes the curve associated with the exclusion of plastic heat generation since the curve is coincident with the reference curve.

(a) Material model variations

(b) Phase transformation considerations

(c) Boundary condition variations
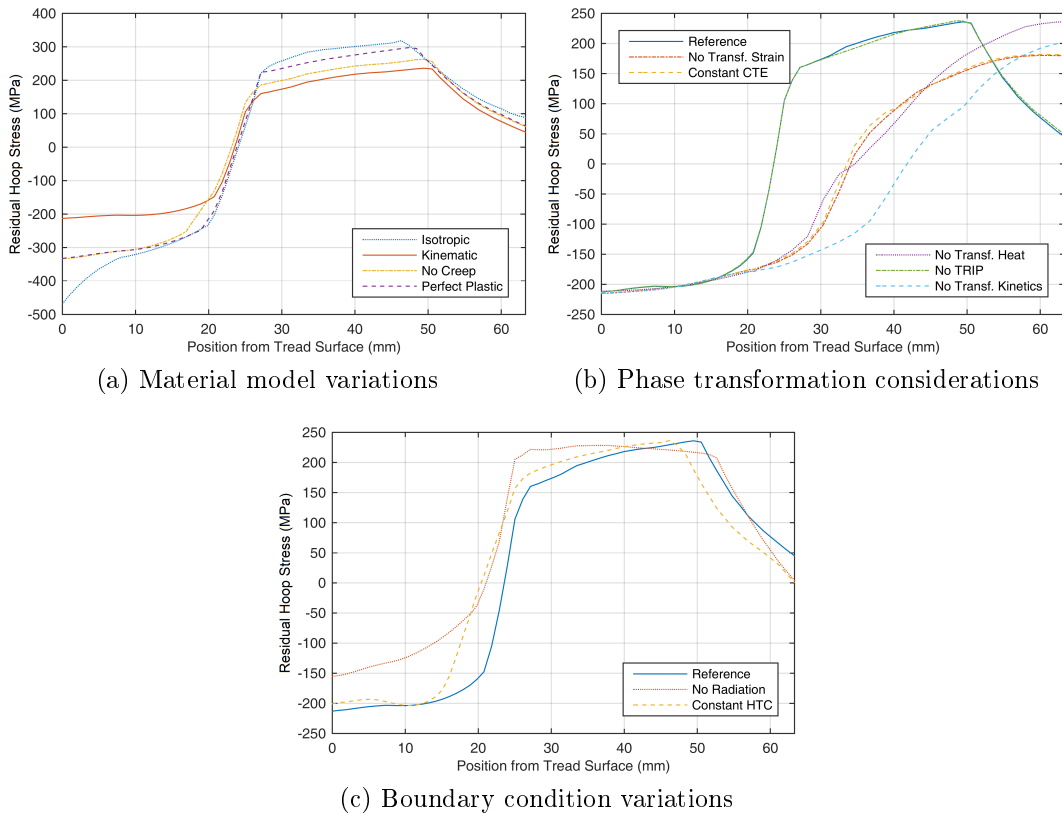
Figure 4.6: Hoop stress comparison at process end

Figures 4.7 through 4.10 show the hoop stress histories for the different material variations, transformation kinetics and boundary conditions respectively. The hoop stress is extracted at two nodes, one on the tread surface on the taping line and one 63 mm below that. The data are also separated at 360 s elapsed time, with the first time span covering the quenching and dwell periods and the second covering the annealing and cooling to room temperature. The reason for the temporal split being the dramatic difference in the rates of change for the hoop stress.

4.3.1   Material Effects

Figure 4.6a shows that there is an appreciable difference in the stress fields produced by the isotropic and kinematic hardening laws, particularly at the tread surface where the hoop stress is more than 100% higher for the isotropic model. Creep and strain hardening also seem to have a much more pronounced effect close to the surface than deeper into the wheel, although not to the same degree as the isotropic hardening model. Given the strong influence of the hardening behaviour of the material, a simple bilinear strain model (consisting of Young's and tangent modulii) might be insufficient to make accurate predictions. Figure 4.7b and 4.7d show that creep starts to exert a strong influence early during the annealing stage; thus it is imperative to include creep, using Equation 4.2.1, if quantitative results are desired.

(a) Surface - quench and dwell

(b) Surface - anneal and cooling

(c) 63mm - quench and dwell

(d) 63mm - anneal and cooling
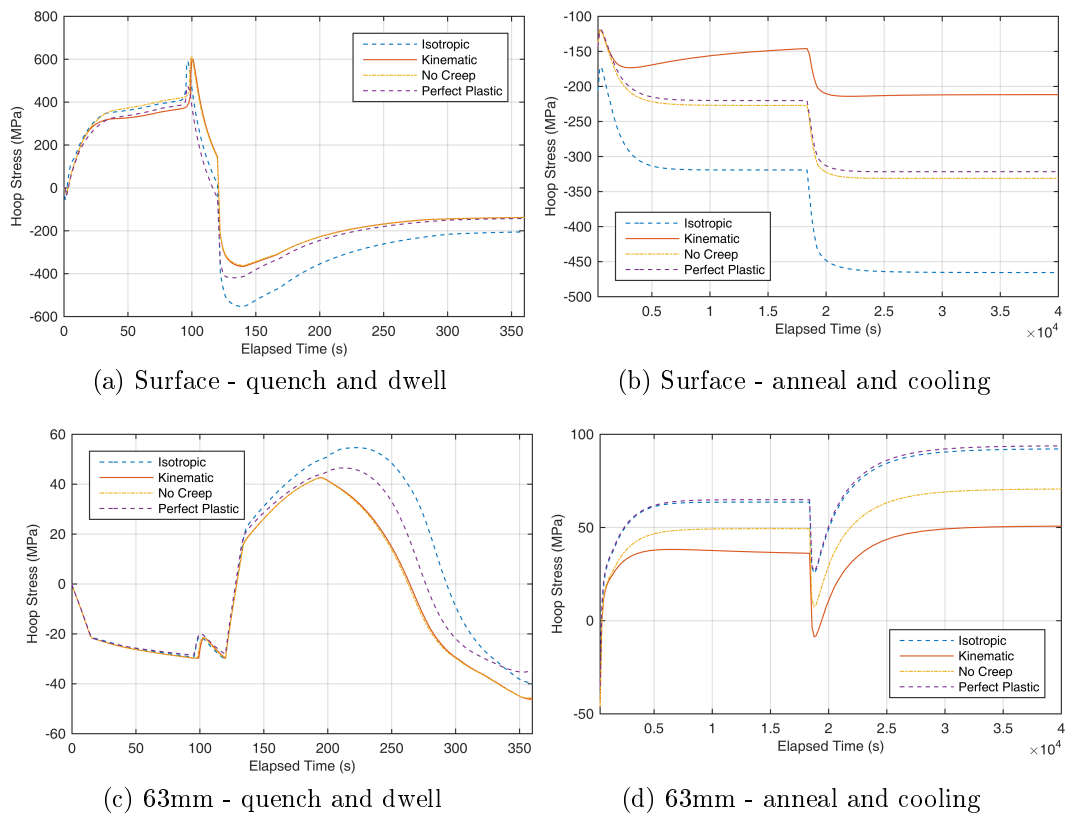
Figure 4.7: Hoop stress history for different material properties

4.3.2   Phase Transformation Effects

From Figure 4.6b it can be seen that TRIP has a very limited impact on the residual hoop stress; albeit with a slightly compromised implementation due to the lack of austenite specific material data. Given the complexity of including

TRIP, it would not be worthwhile to include it in future analyses, especially when considering the uncertainty already accrued throughout such a complex model. Furthermore, resetting the plastic strain tensor and equivalent strain scalar was also omitted with no discernible difference. Without TRIP and resetting the plastic strain, there is no need for user defined subroutines in MSC Marc, providing that explicit phase transformation is not simulated.

Figure 4.6b also shows that, when excluding phase transformation influences, there is only a small difference between the temperature dependent CTE from Table 4.2 (annotated as *no transformation strain*) and a constant CTE. Thus it seems acceptable to construct CTE values from temperature invariant CTE data if necessary.

The phase transformation kinetics on a whole play a crucial role in predicting the residual hoop stress. Figure 4.6b shows that omitting phase transformation effects almost doubles the depth to which the residual stress remains compressive (see also Figure 5.1). The transformation strain and latent heat of transformation can both be seen to have a significant influence on the residual stress. Omitting the latent heat of transformation can also be seen from Figure 4.8a to advance the collapse of the vapour blanket, causing an increase in the heat extracted during the quenching stage.

(a) Surface - quench and dwell (b) Surface - anneal and cooling

(c) 63mm - quench and dwell (d) 63mm - anneal and cooling
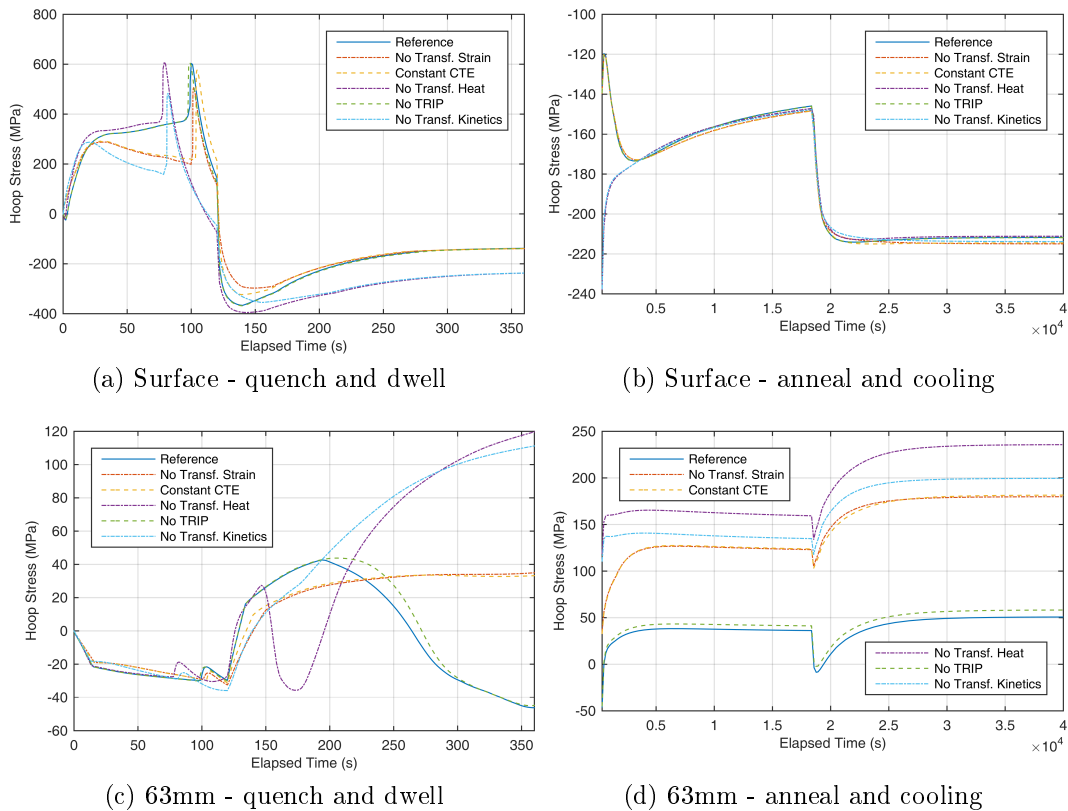
Figure 4.8: Hoop stress history for different transformation kinetics considerations

(a) Reference   (b) No transformation kinetics
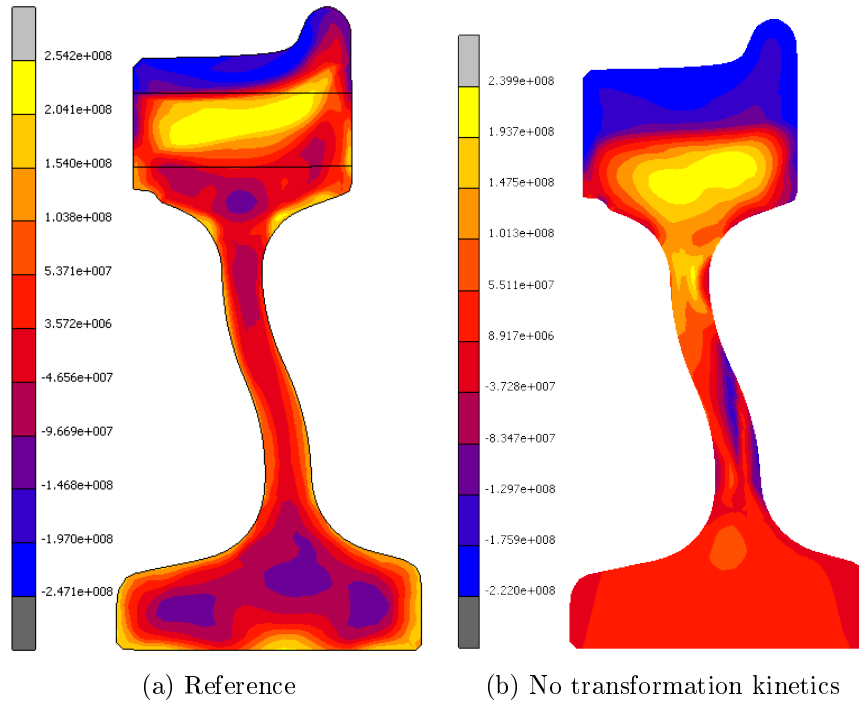
Figure 4.9: Effect of transformation kinetics on residual hoop stress (Units in Pa)

4.3.3 Boundary Conditions

Insofar as boundary condition variations are concerned, the absence of radiation seems to produce the greatest distortion to the residual stress (see Figure 4.6c). The use of a constant HTC also has a marked influence and seems to shift the entire stress curve closer to the surface. The greatest deviation can be seen in the range from 15 mm to 25 mm below the tread surface. The heat generation due to plastic deformation has a negligible effect and it would not be necessary to consider this in future simulations, allowing a decoupled analysis.

4.3.4 Important Parameters

It is clear that certain approximations and simplifications are more detrimental to accurate results than others.

As already observed by Kuhlman *et al.* (1988), material creep plays an important part in predicting the residual stress level. Creep does not seem to have a great influence over the stress pattern, only the actual stress values. The hardening model, as well as the stress strain curve, exert a great influence, especially close to the tread. Due to the importance of strain hardening, the simple bilinear hardening model used in this work might be inadequate for

(a) Surface - quench and dwell

(b) Surface - anneal and cooling

(c) 63mm - quench and dwell

(d) 63mm - anneal and cooling
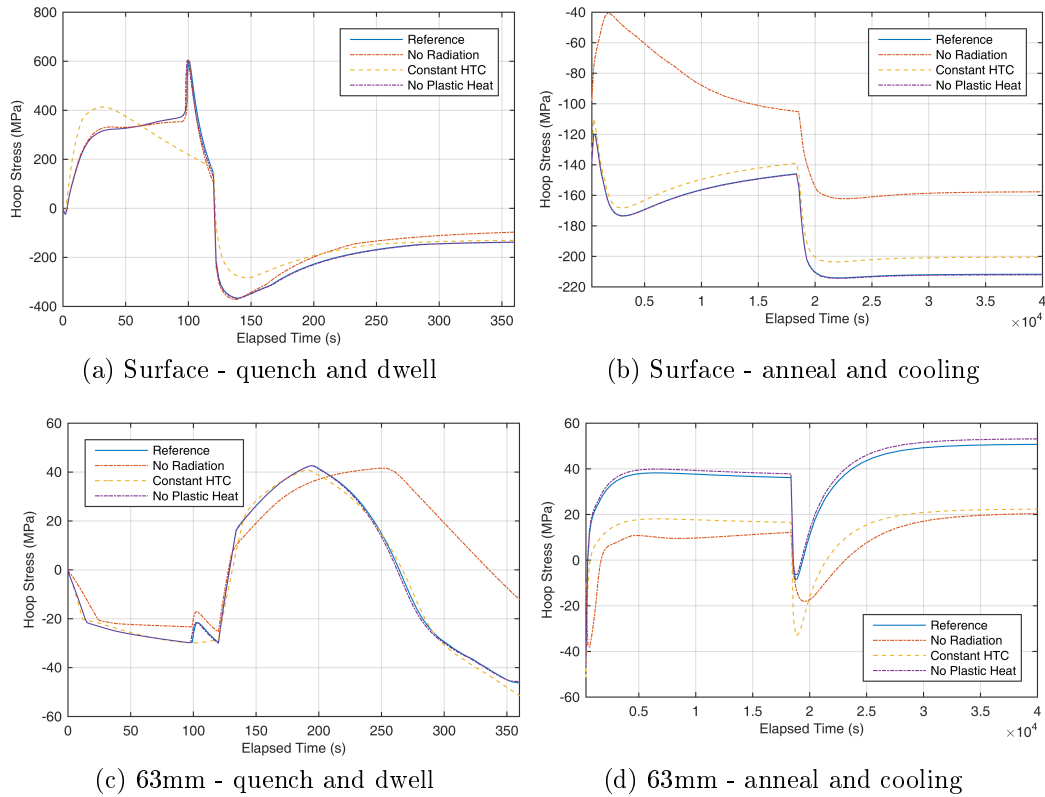
Figure 4.10: Hoop stress history for different boundary conditions

quantitative predictions if the material exhibit highly non-linear hardening behaviour.

The only transformation parameters that exhibit a strong influence on the residual stress are the latent heat of phase transformation and the volume change associated with phase transformation. It is important to note that these transformation effects are even important for qualitative indications of the stress pattern. Given the challenges of including transformation induced plasticity and its almost non discernible impact, together with the build up of uncertainty in complex models like these, it does not seem worthwhile to include transformation induced plasticity when only the residual stress is of interest.

Radiation can be seen to have a significant effect and should be included even for merely qualitative results. Approximating the spray quenching HTC with a constant value is seen to have a marked effect, albeit over a relatively narrow radial zone. Furthermore, due to the wildly varying heat flux and cooling rates close to the tread, it might have a significant effect if the phase transformation is explicitly simulated.

4.4   Conclusion

A nominal case for simulating the development of the residual stress field due to tread quenching of a railway wheel is presented. Variations in model parameters relating to material behaviour, phase transformations and boundary conditions are thereafter implemented and the results of these simulations are presented. Phase transformation effects appear to exert the highest influence on the residual stress field, with transformation strain and latent heat of transformation being very important. The strain hardening and creep behaviour of the material also have a significant influence on the residual stress field. The hardening models evaluated were only adequate for qualitative simulations and further research is needed in which a more accurate stress-strain relationship is used. The heat transfer boundary conditions exhibit a marked influence on the simulation results.

The residual stress field at the end of the entire process as found in the *reference* load case (shown in Figure 4.5) shall be used as the initial stress state for further work in Chapter 6.

Chapter 5

Heat Transfer Characteristics

5.1 Introduction

The rate of heat transfer to the atmosphere is a key factor in the performance of wheels that are subjected to tread braking. The Transnet standard that is the fundamental departure point for this research, as well as the UIC-510 and AAR S-660 standards, focus heavily on the behaviour of railway wheels under braking applications. Under heavy braking, the wheel rim on s-dish wheels tend to displace axially and therefore change the gauge of the wheelset. Heavy braking can even cause yielding which acts to offset and even reverse the compressive residual stress in the rim. This residual stress is laboriously induced during the manufacturing process and is a key feature of the wheel, meant to suppress potential crack growth and catastrophic failure.

5.2 Heat Transfer Predictions

Four different methods of calculating the heat transfer coefficients are compared. First, the heat transfer coefficient is calculated by approximating the wheel as a circular flat plate exposed to parallel flow. Secondly, two models for a rotating body in stationary air is used. The third method approximates the wheel as a flat rotating disc in parallel flow. Finally, computational fluid dynamic (CFD) simulations with the actual wheel geometry are performed with the wheel rotating in a parallel flow field. The CFD results will serve as the baseline with which to compare the other methods.

In the following subsections, the background for the first three approximations are discussed. Data from various researchers are reported as they presented it. Note that some of the data are for local Nusselt numbers, whereas other researchers only report the mean (spatially averaged) Nusselt numbers.

5.2.1 Non-dimensional Heat Transfer Analysis

Convective heat transfer is typically described in non-dimensional form using the Nusselt number. By converting the problem into a non-dimensional form, the data is more transferable to similar problems, even if there are large differences in the scale of the problem. The Nusselt number is a non-dimensional number representing the ratio between convective and conductive heat transfer across a boundary between two media. The Nusselt number is defined as:

$$Nu = \frac{hL}{k} \qquad (5.2.1)$$

where h is the heat transfer coefficient, L is the characteristic length, and k represents the conductivity of the fluid.

Experimental heat transfer data is often presented in the non-dimensional form:

$$Nu = CRe^m Pr^n \qquad (5.2.2)$$

where C is a constant of proportionality, Re is the Reynolds number, Pr shows the Prandtl number, and m and n are the fitted exponents for Re and Pr, respectively.

The heat transfer changes considerably when the flow transitions from laminar to turbulent flow. It is therefore sometimes necessary to have two separate equations for laminar and turbulent heat transfer. If equation 5.2.2 is for the local Nusselt number, it needs to be integrated and averaged over the length of the flow path to obtain the average heat transfer coefficient. The average Nusselt number over length L for flow that changes from laminar (subscript 1) to turbulent (subscript 2) at a critical Reynolds number (Re_{cr}) is shown in Appendix E.1 to be:

$$Nu_L = \frac{C_1}{m_1} Re_{cr}^{m1} Pr^{n1} + \frac{C_2}{m_2} \left(Re_L^{m2} - Re_{cr}^{m2} \right) Pr^{n2} \qquad (5.2.3)$$

For fluids with Prandtl number in excess of 0.6, it can be shown that the Nusselt number for heat transfer from a flat plate is proportional to $Pr^{1/3}$ (Çengel and Ghajar, 1998; Kays *et al.*, 1966). Dorfman (1963) states that for rotating discs in stationary fluid, $Nu \propto Pr^{0.6}$. This is often enforced explicitly in equation 5.2.2 when experimental data is fitted to the equation, rather than having n as an additional dimension to fit.

5.2.2 Parallel Flow Over Flat Plate

It was shown by Pohlhausen (1921) (as reported by Schlichting (1955)) that for incompressible laminar flow over an isothermal flat plate with $0.6 < Pr < 10$, the non-dimensional heat transfer equation is:

$$Nu_x = 0.332 Re_x^{0.5} Pr^{1/3} \qquad (5.2.4)$$

The related equation for turbulent flow is given by Schlichting (1955) to be:

$$Nu_x = 0.0296 Re_x^{0.8} Pr^{1/3} \tag{5.2.5}$$

Substituting equations 5.2.4 and 5.2.5 into the form of equation 5.2.3 for flow changing from laminar to turbulent at Re_{cr} yields:

$$Nu_L = 0.664 Re_{cr}^{0.5} Pr^{1/3} + 0.037 \left(Re_L^{0.8} - Re_{cr}^{0.8} \right) Pr^{1/3} \tag{5.2.6}$$

subject to $0.6 < Pr < 10$.

5.2.2.1   Critical Reynolds Number

It is clear that a fundamental requirement for using the combined regime equation 5.2.6 is the critical Reynolds number. Unfortunately the solution is not that simple. In the comparison to follow, it is assumed that anyone using one of the three basic models discussed here as an approximation for a railway wheel will also use the recommended critical Reynolds number that is typically reported with the heat transfer correlations. However, it is important to understand that the critical Reynolds number is dependent on the characteristics of the flow field, particularly the free stream turbulence. Free stream turbulence intensity can be defined as the ratio of the velocity fluctuations to the mean velocity. Expressed as:

$$Ti = \frac{u'}{U} \tag{5.2.7}$$

where u' is the root-mean-square of the velocity fluctuations and U is the mean velocity at the same location

The cumulative (and therefore average) heat transfer from a surface can be markedly influenced by these variations. This is also clear from the history of the research aimed at establishing the heat transfer from a flat plate in parallel flow.

According to Schlichting (1955), researchers initially thought that the critical Reynolds number is in the range of $3.5(10^5)$ to $5(10^5)$. In the early days, the turbulence intensity of the free stream was not measured, however according to Schlichting it would have typically been around 1%. Van der Hegge Zijnen (1924) then observed that if disturbances in the free stream were increased, through the addition of a wire screen, the transition in the boundary layer occurs at a much lower Reynolds number. A comprehensive study at the National Bureau of Standards in the United States was undertaken on the transition of boundary layers from laminar to turbulent. From this study, Dryden (1936) reports a critical Reynolds number of $1.1(10^6)$ at $Ti = 0.5\%$. In comparison, Schlichting (1955) states that for $Ti \approx 0.5\%$, $Re_{cr} = 3.5(10^5)$ to 10^6. Schubauer and Skramstad (1943), also from the National Bureau of Standards study, show that the critical Reynolds number reaches an upper limit of around $2.8(10^6)$ for any turbulence intensity less than 0.08%.

5.2.3   Rotating Bodies in Stationary Fluid

Investigations for both the fundamental case of an isothermal disc as well as railway wheels on brake dynamometers have been published. Here the local Reynolds number is defined as:

$$Re_r = \frac{\rho \omega r^2}{\mu} \tag{5.2.8}$$

where ρ is the fluid density, ω is the rotational velocity, r shows the radius, and μ represents the dynamic viscosity of the fluid.

5.2.3.1   Rotating Disc in Stationary Air

The experiments by Cobb and Saunders (1956), using air as working fluid ($Pr \approx 0.7$), found for a laminar boundary layer, the average Nusselt number up to radius R is:

$$Nu_R = 0.36 Re_R^{0.5} \tag{5.2.9}$$

Cobb observed a critical Reynolds number of around $240\,(10^3)$. For a turbulent boundary layer, the average Nusselt number up to radius R was found as:

$$Nu_R = 0.015 Re_R^{0.8} \tag{5.2.10}$$

Rewriting equations 5.2.9 and 5.2.10 into the form of equation 5.2.3 (specifically for air with $Pr \approx 0.7$) for the mean Nusselt number of combined laminar and turbulent flow yields:

$$Nu_R = 0.36 Re_{cr}^{0.5} + 0.015 \left(Re_R^{0.8} - Re_{cr}^{0.8} \right) \tag{5.2.11}$$

5.2.3.2   Rotating Railway Wheel in stationary Air

Vernersson ($2007b$) obtained heat transfer data for a railway wheel on a brake dynamometer for speeds of 50, 75, and 100 km/h. Fitting the data to equation 5.2.2 (with $n = 1/3$ fixed) for the local Nusselt number in different wheel regions, he obtained the parameters as shown in Table 5.1.

Table 5.1: Vernersson local heat transfer parameters

Parameter	Wheel Web	Sides of Wheel Rim	Wheel Tread
C braking	0.02	0.01	0.03
C cooling	0.02	0.01	0.02
m	0.8	0.8	0.8

5.2.4 Rotating Disc in Parallel flow

A rotating disc in parallel flow was investigated by Aus der Wiesche (2007) using large eddy simulations with air as the fluid. The average Nusselt number for this combined flow condition is:

$$Nu = Nu\left(Pr, Re_u, Re_\Omega\right) \tag{5.2.12}$$

where Re_u is the linear Reynolds number and Re_Ω the rotational Reynolds number. Aus der Wiesche also investigated the two limit cases of a circular flat plate in parallel flow and a rotating disc in stationary air.

5.2.4.1 Limit Case: Stationary Disc in Parallel Flow

For parallel flow, the average Nusselt number Aus der Wiesche found was:

$$Nu_R = 0.417Re_{uR}^{0.5} \quad \text{for } Re_{uR} \leq 5 \times 10^4 \tag{5.2.13}$$
$$Nu_R = 0.0127Re_{uR}^{0.8} \quad \text{for } Re_{uR} \geq 5 \times 10^4 \tag{5.2.14}$$

Aus der Wiesche used the characteristic length $Lc = R$, rather than the usual $Lc = \frac{Area}{Width} = \frac{1}{2}\pi R$. It is worth noting the considerably lower critical Reynolds number for turbulence intensity of just 0.82% (reported as turbulent kinetic energy $= 10^{-4}.u_{in}^2$) compared to that discussed in section 5.2.2.1.

5.2.4.2 Limit Case: Rotating Disc in Stationary Air

In the case of a rotating disc in stationary air, the mean Nusselt number was found as:

$$Nu_R = 0.33Re_{\Omega R}^{0.5} \quad \text{for } Re_{\Omega R} \leq 2 \times 10^5 \tag{5.2.15}$$
$$Nu_R = 0.015Re_{\Omega R}^{0.8} \quad \text{for } Re_{\Omega R} \geq 2 \times 10^5 \tag{5.2.16}$$

This result is very similar to that reported by Cobb and Saunders as discussed in section 5.2.3.1.

5.2.4.3 Rotating Disc in Parallel Flow

For a rotating isothermal flat disc in parallel flow, the average Nusselt numbers as reported by Aus der Wiesche are:
For $10^3 \leq Re_{uR} \leq 5 \times 10^4$

$$Nu_R = \begin{cases} 0.417Re_{uR}^{0.5} & \text{for } Re_{\Omega R}/Re_{uR} \leq 1.4 \\ 0.33Re_{\Omega R}^{0.5} & \text{for } Re_{\Omega R}/Re_{uR} > 1.4 \end{cases} \tag{5.2.17}$$

For $Re_{uR} > 5 \times 10^4$

$$Nu_R = \begin{cases} \sqrt{(0.0127Re_{uR}^{0.8})^2 + (0.33Re_{\Omega R}^{0.5})^2} & \text{for } Re_{\Omega R} < 2 \times 10^5 \\ \sqrt{(0.0127Re_{uR}^{0.8})^2 + (0.015Re_{\Omega R}^{0.8})^2} & \text{for } Re_{\Omega R} > 2 \times 10^5 \end{cases} \tag{5.2.18}$$

5.3 Computational Fluid Dynamics Simulations

Convective heat transfer from the wheel was simulated using Mentor Graphics' FloEFD package. The code uses an immersed boundary Cartesian mesh. This is to say that the Cartesian computational domain, rather than the geometry, is used to build the mesh. Wherever a cell is intersected by a geometric boundary, the cell is split to form a fluid cell and a solid cell along the intersection. To obviate the need for a body fitted mesh, the code uses a "two-scale wall function approach" with a thick- and thin boundary layer approach (Mentor Graphics, 2011). The thick layer approach is used for $y^+ < 300$ and the thin layer approach for coarse wall-adjacent cells with $y^+ > 300$. Generally, the thin layer approach is more reliant on empirical and semi-empirical corrections (including the effect of the free stream turbulence on the boundary layer) (Mentor Graphics, 2011).

5.3.1 CFD Validation

As no experimental validation of the final results was performed, a validation problem was first solved and compared to well established empirical formulations. This was done to demonstrate the relevant capabilities of the code. The validation problem used here is a modified version of a problem published by Mentor Graphics (2013). It aims to replicate the parallel flow over a flat plate as described in Section 5.2.2. Flow is simulated in two dimensions over a 1 m flat plate for a variety of velocities (used to control Reynolds number) and free stream turbulence levels. Ambient temperature is taken as 20 °C with the wall temperature at 30 °C. The mesh independence study is discussed in Section F.1 of Appendix F.

To judge the quality of the heat transfer predicted by the CFD code, the one-dimensional spatial distribution of the heat transfer coefficient (HTC) is compared to the experimental model discussed in section 5.2.2.

The results of an investigation into the upper limit of the critical Reynolds number is shown in Figure 5.1a. Clearly the CFD code captures the limit at more or less the same level of free stream turbulence ($Ti < 0.05\%$ compared to 0.08%) as observed by Schubauer and Skramstad, albeit that the upper limit of the critical Reynolds number is 12.5% lower than what they reported.

Figure 5.1b compares the heat transfer coefficient for three different free stream turbulence levels. The simulation with $Ti = 0.0001\%$ was performed with $v = 60$ m.s^{-1} and the other two at 20 m.s^{-1}. It is evident that at the higher turbulence levels the data from the CFD simulations correspond exceptionally well to that of the experimental model. One possible reason for the poorer correlation at the lower turbulence level is that the Reynolds number is considerably higher and is raised to the power of only a single significant

digit exponent in the experimental model. For $Ti = 0.5\%$, the critical Reynolds number, for all practical purposes, exactly match what Dryden reports. In the case of $Ti = 1\%$, the critical Reynolds number, at $5.4(10^5)$, exceeds the upper limit given by Schlichting with 8%; although the turbulence levels during those early experiments are not absolutely known.

(a) Critical Reynolds number upper limit   (b) One-dimensional spatial HTC
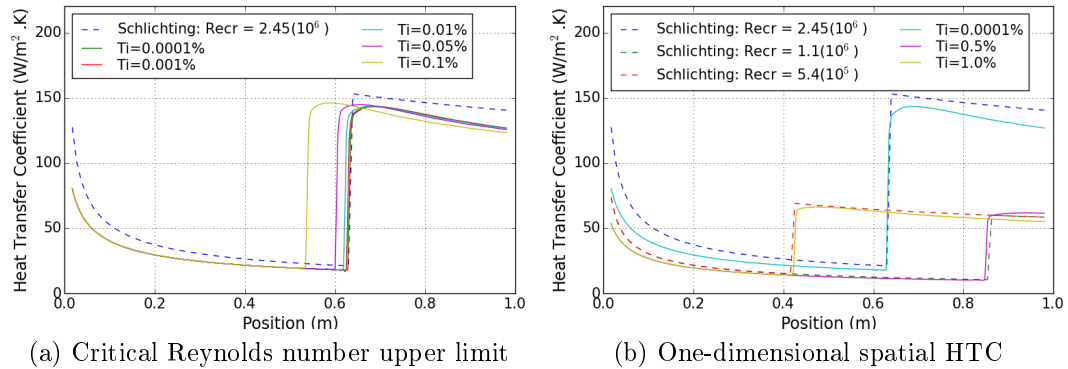
Figure 5.1: Validation problem results

Note that from the definition of the local Nusselt number, the local heat transfer coefficient would tend to infinity as the length goes to zero. It is expected that the numerical (discretised) results would not match this and that there would be an appreciable discrepancy between analytic and numerical results close to the leading edge. With this said, FloEFD consistently under predicts the laminar heat transfer (relative to Pohlhausen's analytical prediction) for low levels of free stream turbulence, albeit with diminishing error with increasing distance from the leading edge.

The data suggest that FloEFD is able to predict the critical Reynolds number as well as the turbulent heat transfer with fair accuracy, especially for higher free stream turbulence. At lower levels of free stream turbulence, FloEFD seems to consistently under predict the heat transfer coefficients, especially close to the leading edge and for the turbulent boundary layer.

5.3.2   CFD Simulation of Railway Wheel

The full 5M2A wheel was analysed to determine the heat transfer characteristics. The CFD data is then also compared to the heat transfer correlations, discussed in 5.2, to determine whether some of these could reasonably be used in future work to predict heat transfer from railway wheels in lieu of dedicated CFD analyses. The mesh independence study is discussed in Section F.2 of Appendix F.

5.3.2.1 Forced Convection

The heat transfer from the wheel was simulated under zero gravity for 31 different velocities, ranging from 0.1 to 100 m/s. As before, the atmospheric temperature is 20 °C. Two wall temperatures of 70 and 670 °C were used.

From Figure 5.2 it can be seen that the boundary layer changes from laminar to turbulent at $Re \approx 40 \, (10^3)$. A least squares fit was performed to obtain the non dimensional heat transfer equations of the form of equation 5.2.2. This yields for laminar:

$$Nu_{Lc} = 0.664 Re_{Lc}^{0.5} Pr^{1/3} \tag{5.3.1}$$

and for turbulent:

$$Nu_{Lc} = 0.0244 Re_{Lc}^{0.8} Pr^{1/3} \tag{5.3.2}$$

Combined laminar/turbulent:

$$Nu_{Lc} = \left\{ 0.664 Re_{cr}^{0.5} + 0.0244 \left(Re_{Lc}^{0.8} - Re_{cr}^{0.8} \right) \right\} Pr^{1/3} \tag{5.3.3}$$

Where $L_c = \frac{1}{2}\pi R$ and $Re_{cr} = 40(10^3)$.
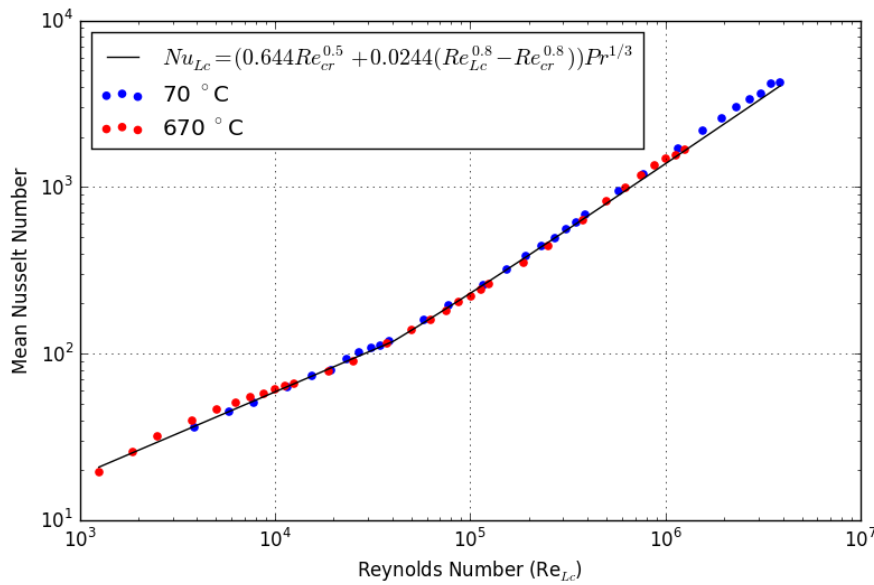
Figure 5.2: Forced convection data fit

5.3.2.2 Natural Convection

The heat transfer under natural convection conditions was simulated at seven surface temperatures, ranging from 70 °C to 670 °C (100 °C steps).

Figure 5.3 shows the predicted (from non-dimensional equation) versus simulated (from CFD) heat transfer coefficients and heat flux for each of the seven temperatures (the black line showing perfect agreement). Comparing

the simulation results to the predicted natural convection from a vertical flat plate shows significant disparity. In fact, an equation of the same form could not be fitted to the simulation data with satisfactory fidelity. An equation of the form that is used for natural convection from a sphere was used instead with good results. The obtained non-dimensional heat transfer equation is:

$$Nu_{Lc} = \frac{0.586 Ra_{Lc}^{0.25}}{\left[1 + (0.469/Pr)^{(9/16)}\right]^{(4/9)}} - 1.44 \quad \text{for } L_c = R \qquad (5.3.4)$$

$$Nu_{Lc} = \frac{0.656 Ra_{Lc}^{0.25}}{\left[1 + (0.469/Pr)^{(9/16)}\right]^{(4/9)}} - 1.44 \quad \text{for } L_c = \frac{1}{2}\pi R \qquad (5.3.5)$$

where Ra is the non-dimensional Rayleigh number.

(a) Heat transfer coefficient   (b) Heat flux
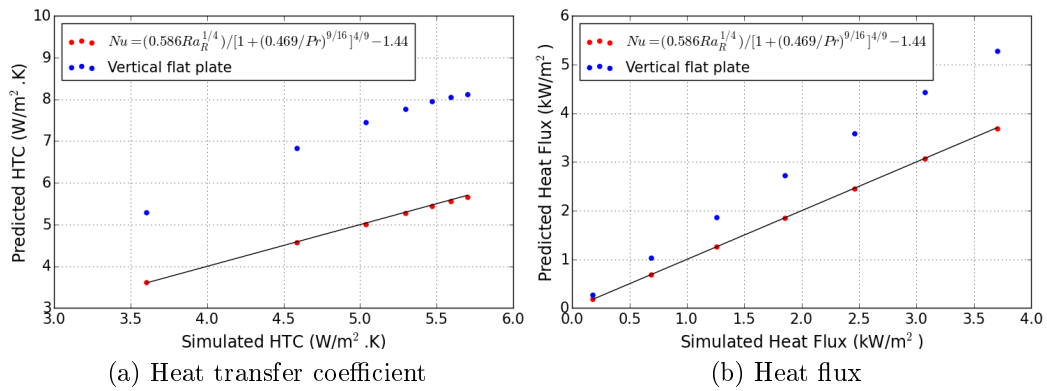
Figure 5.3: Railway wheel natural convection

5.4 Heat Transfer Comparison

The heat transfer from the wheel to the atmosphere was simulated for five velocities ranging from 0 to 80 km/h (20 km/h steps) and the same temperature range as before. The heat transfer equations discussed in Section 5.2 were then used to predict the heat transfer coefficient to ascertain whether some are suitable for railway wheels.

In order to account for the effect of gravity, the combined forced and natural convection non dimensional heat transfer coefficient was calculated using (Çengel and Ghajar, 1998):

$$Nu_{combined} = \sqrt[3]{Nu_{forced}^3 + Nu_{natural}^3} \qquad (5.4.1)$$

Figure 5.4 again shows the predicted versus simulated HTC and heat flux, with the line representing a perfect correlation. All but the the equations obtained in this study were combined with the natural convection for a flat

plate. This clearly produces an over prediction of the HTC, as can be seen by
the bottom left cluster in Figure 5.4a. This is clearly to be expected given the
results shown in Figure 5.3.

(a) Heat transfer coefficient   (b) Heat flux
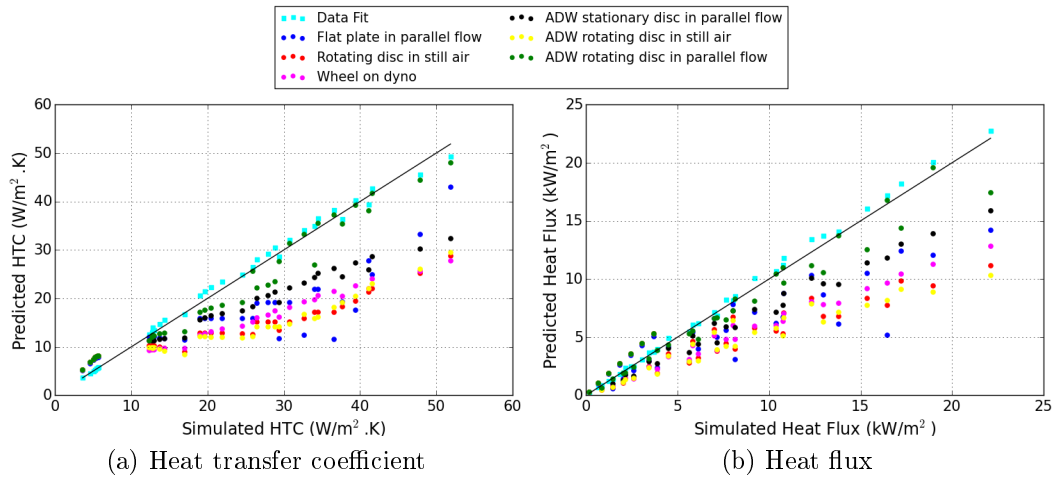
Figure 5.4: Heat transfer comparison

Figure 5.4 shows that Aus der Wiesche's model for a rotating disc in
parallel flow provides a fair approximation to the problem of a railway wheel
in a free stream, with the other models all falling way short of a reasonable
representation. Aus der Wiesche's model seems to under predict the HTC for
lower velocities (20, 40, and 60 km/h) and then captures the heat transfer for
80 km/h with markedly better accuracy. When changing the critical value for
the rotational Reynolds number to $Re_{\Omega R} = 5(10^4)$, the same as the critical
value for the linear Reynolds number, and by combining the model with the
natural convection model obtained in Section 5.3.2.2, the result as shown in
Figure 5.5 is obtained. This modification renders the Aus der Wiesche model
even more accurate than the model obtained by the data fit in Section 5.3.2.1
for many of the data points.

(a) Heat transfer coefficient   (b) Heat flux
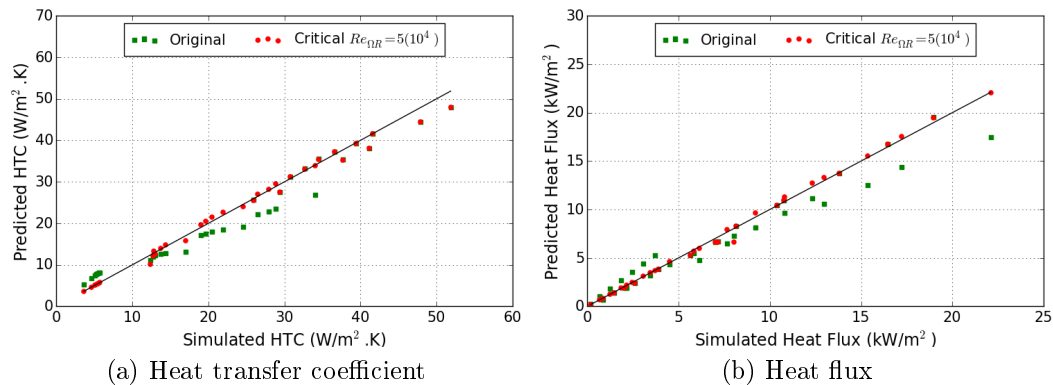
Figure 5.5: Modified Aus der Wiesche model of a rotating disc in parallel flow

5.5   Conclusion

In answering the fundamental question of this chapter, namely which heat transfer models are appropriate for predicting the heat transfer from a railway wheel, we can conclude that either Aus der Wiesche's model for a rotating disc in parallel flow or the new model obtained in this chapter (Sections 5.3.2.1 and 5.3.2.2) can be used. For heat transfer under stationary or low velocity conditions, it is recommended that these models are combined (using equation 5.4.1) with the natural convection correlation derived in this chapter (Section 5.3.2.2).

The close correlation between Aus der Wiesche's model and the one obtained in this chapter with the actual geometry of a railway wheel suggest that the specifics of the flow field, rather than the geometry, has the greatest influence. It is therefore likely that the model obtained in this chapter (and that of Aus der Wiesche) can also be used for other axisymmetric wheels without a great loss of accuracy.

5.5.0.3   New Natural Convection Model

$$Nu_{Lc} = \frac{0.586 Ra_{Lc}^{0.25}}{\left[1 + (0.469/Pr)^{(9/16)}\right]^{(4/9)}} - 1.44 \quad \text{for } L_c = R$$

$$Nu_{Lc} = \frac{0.656 Ra_{Lc}^{0.25}}{\left[1 + (0.469/Pr)^{(9/16)}\right]^{(4/9)}} - 1.44 \quad \text{for } L_c = \frac{1}{2}\pi R$$

5.5.0.4   New Forced Convection Model

For $Re_{Lc} \leq 4 \times 10^4$

$$Nu_{Lc} = 0.664 Re_{Lc}^{0.5} Pr^{1/3}$$

For $Re_{Lc} > 4 \times 10^4$

$$Nu_{Lc} = \left\{0.664(4 \times 10^4)^{0.5} + 0.0244\left(Re_{Lc}^{0.8} - (4 \times 10^4)^{0.8}\right)\right\} Pr^{1/3}$$

Where $L_c = \frac{1}{2}\pi R$.

5.5.0.5   Modified Aus der Wiesche Model

For $10^3 \leq Re_{vR}, Re_{\Omega R} \leq 5 \times 10^4$

$$Nu_R = 0.417 Re_{vR}^{0.5}$$

For $Re_{vR}, Re_{\Omega R} > 5 \times 10^4$

$$Nu_R = \sqrt{(0.0127 Re_{vR}^{0.8})^2 + (0.015 Re_{\Omega R}^{0.8})^2}$$

Chapter 6

Effects of Simplifications on Prescribed FEA

6.1   Introduction

This chapter investigates the effect of common assumptions and simplifications employed in the analysis of railway wheels. We shall try to establish, under various conditions, which assumptions are acceptable and which should be avoided. On many occasions, only qualitative derivations can be made due to the lack of fidelity in the input data available.

6.2   Material Data

Similar to the heat treatment analysis in Chapter 4, the purpose of the analysis here is to provide qualitative insight into the sensitivity of the relevant models to typical assumptions and simplifications. To this end, we do not need the material data for the specific wheel or brake blocks, but rather representative data. Since the high temperature data for the 5M2A wheel material is not available, the material data from Chapter 4 will be used here as well and is shown in Tables 4.1 and 4.2. For these analyses the yield stress was scaled in order for the yield stress at room temperature to match that of the actual wheel material. This was done to allow the wheel to cope with the contact loads more like it actually would and also as was simulated in Chapter 3.

Creep is also taken into account with the equation from Kuhlman *et al.* (1988). Written in SI units as:

$$\dot{\varepsilon} = 1.5305(10^{-93})\sigma_{eq}^{12.5}e^{\left(\frac{-29840}{T+273}\right)} \tag{6.2.1}$$

with the equivalent stress (σ_{eq}) in Pascal and the temperature (T) in degrees Celsius.

For the composite brake blocks, the material data from Vernersson (2007*a*) were used and is shown in Table 6.1.

Table 6.1: Material properties for composite brake blocks (Vernersson, 2007a)

Temp (°C)	Specific Heat c_p (J/kg.K)	Thermal Conductivity (W/m.K)	Density ρ (kg/m^3)
0	1500	5.0	2670

6.3   Normal Contact Investigation

As discussed in Chapter 3, the common way of dealing with non-Hertzian loads is to find a representative elliptical (Hertzian) contact condition. Contact was simulated on a one-half symmetric model of the wheel by applying a semi-ellipsoidal pressure distribution over a semi-elliptical (due to symmetry) contact area. The location of the contact pressure was controlled through the use of coordinates and the element edges do not line up with the contact patch. Since all the different contact patches that were investigated were slightly different, it would have required a different model for each analysis to have the element edges line up with the contact patch boundary.

Two different equivalent Hertzian approaches were investigated. For both of these, the aspect ratio of the contact patch (taken as the aspect ratio of a rectangle that encloses the contact patch) is kept the same as the contact simulation results from Chapter 3. For the first method, the contact patch area is taken as equal to the contact simulation results while the peak contact pressure is changed to ensure the correct load is applied. In the second method, the peak contact stress is set equal to the contact simulation results and the contact patch size is changed in order to ensure the correct load.

6.3.1   Elastic Response

For the following comparison, the peak equivalent stress is used as the metric. Figure 6.1 (area/stress refers to the parameter that is kept the same as the simulation results) shows that when using an equivalent Hertzian representation of the FEA results, keeping the original peak contact pressure and changing the contact area produces appreciably better results, especially in the flange root. For the results obtained from the boundary element method, there is hardly any difference between the two implementations, suggesting a tendency to produce contact pressures much closer to the Hertzian values than the FEM.

Interestingly, for contact in the flange root, Hertzian contact produces a peak equivalent stress closer to the explicit FEM results than the BEM results do. FEM consistently produced results that are appreciably non-Hertzian, as indicated by the difference between the two equivalent Hertzian approaches. BEM results for contact on the taping line seem to be the furthest from ideal
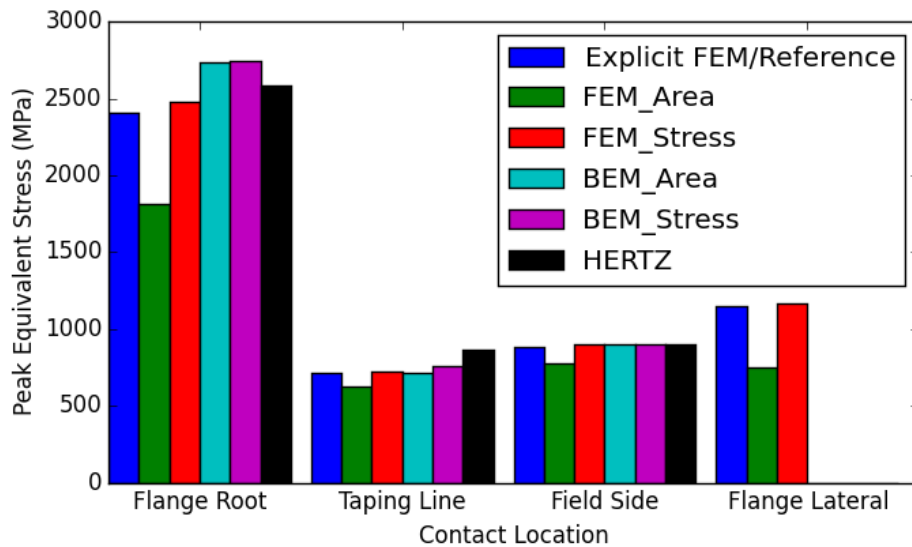
Figure 6.1: Elastic equivalent Hertzian comparison

Hertzian contact. This also accords with the findings in Chapter 3, which is that the transition from the curved inner region to the linear taper of the field side of the profile, causes a clearly non-Hertzian contact condition. For the case of lateral flange contact, where only FEM data is available, using the constant peak contact stress implementation of the equivalent Hertzian method seems to be vastly superior, when judged by the peak equivalent stress at least.

6.3.2   Plastic Response

Incorporating plasticity in the analysis was merely done for qualitative insights, since no account is taken of the geometric and pressure distribution variations resulting from the plastic compliance of the contact zone.

Figure 6.2 shows that for contact in the flange root, there is a vast difference between the full non-linear contact simulation and the equivalent Hertzian method (note that full mesh independence was not achieved for contact in the flange root area due to limited computational power). For contact over the rest of the wheel profile, the equivalent Hertzian method actually emulates the non-linear contact fairly well. In reference to the findings in Chapter 3, it seems that as long as the plasticity does not reach the surface of the wheel rim, the equivalent Hertzian method is conducive to analyses incorporating plasticity.

In contrast to the the elastic response, for plastic behaviour it seems the original area approach produces more accurate results. For lateral flange contact, the original stress approach is necessary to obtain conservative results, albeit considerably less accurate.
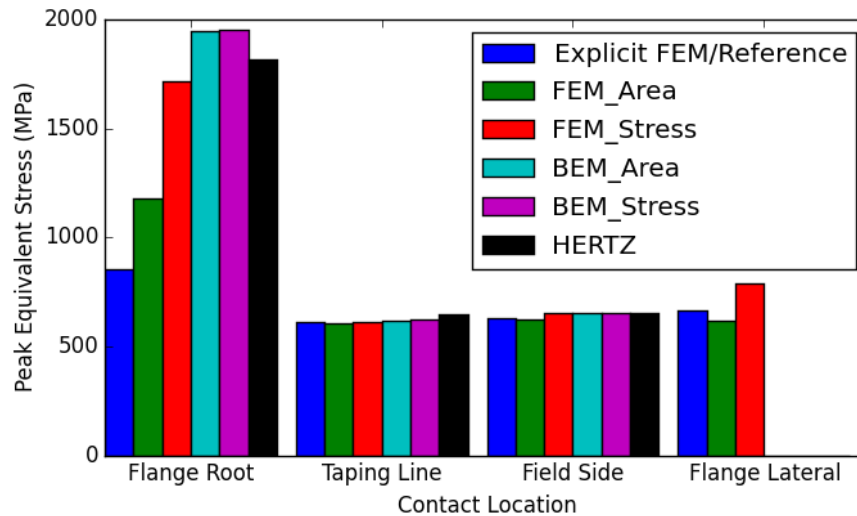
Figure 6.2: Plastic equivalent Hertzian comparison

The equivalent Hertzian approach in conjunction with plasticity is especially useful as the validity of the approach can be appraised without any external reference. Using the data from FEM with the original area (green in Figure 6.1), it is clear from Figure 6.3 that the plasticity reaches the surface at the flange root, but remains completely surrounded by elastic material for all the other locations. It is thus conceivable that the equivalent Hertzian approach can be used for analyses requiring plasticity and then be evaluated on its applicability by checking whether the plastic areas are fully confined. In the cases where it is not, a fully non-linear contact simulation would be required.

Note that with the equivalent Hertzian approach, it is not predicted that the material at the tread surface for lateral flange contact would deform plastically. This contradicts the findings in Chapter 3 from the explicit simulations. The reason for this is simply that, although the constant area implementation provides the closest result to the explicit simulation, it is not conservative with respect to the explicit contact simulations. When using the original stress implementation, the tread surface does indeed deform plastically as shown in Figure 6.4.

(a) Flange root

(b) Taping line

(c) Field side

(d) Flange lateral
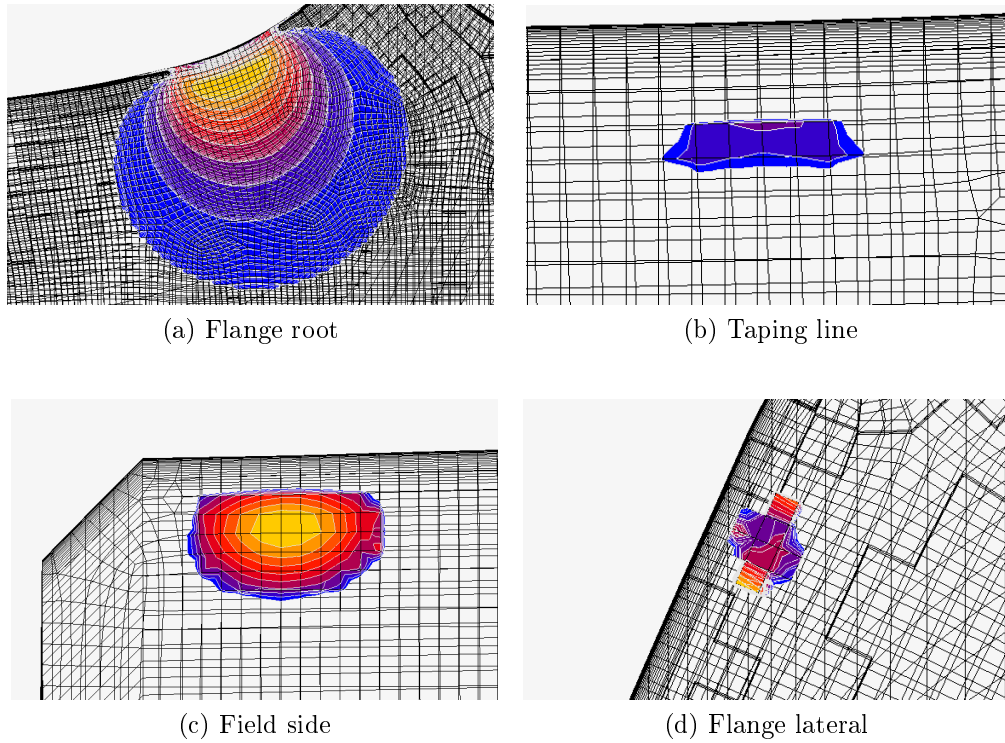
Figure 6.3: 600 MPa von Mises stress boundary
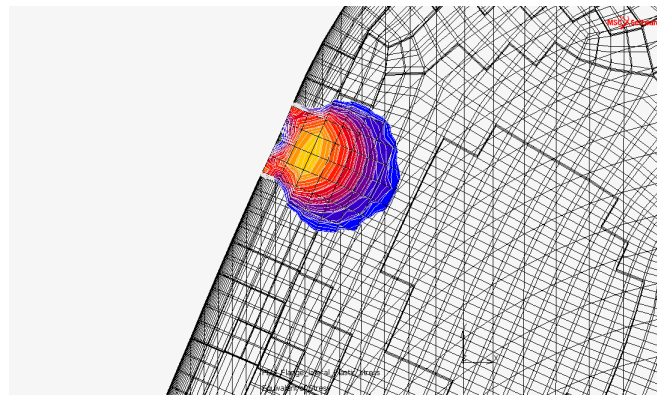
Figure 6.4: Plastic equivalent Hertzian comparison

6.4   Wheel/Axle Interference Fit

The wheel is shrink-fitted onto the axle with a nominal interference of 0.24 mm on the diameter (base diameter being 177.5 mm). To determine the direct effect of this on the wheel, an axisymmetric FEA was performed.

6.4.1   FEA Model

The model consisted of 6 641 elements (predominately 4 node quadrilateral) and 6 916 nodes with the wheel separated into three mesh regions (see Figure 6.5). Instead of simulating the assembly process with the true interference represented by the geometries, the *interference fit* feature of MSC Marc's contact engine was used to force an artificial gap between the two bodies.
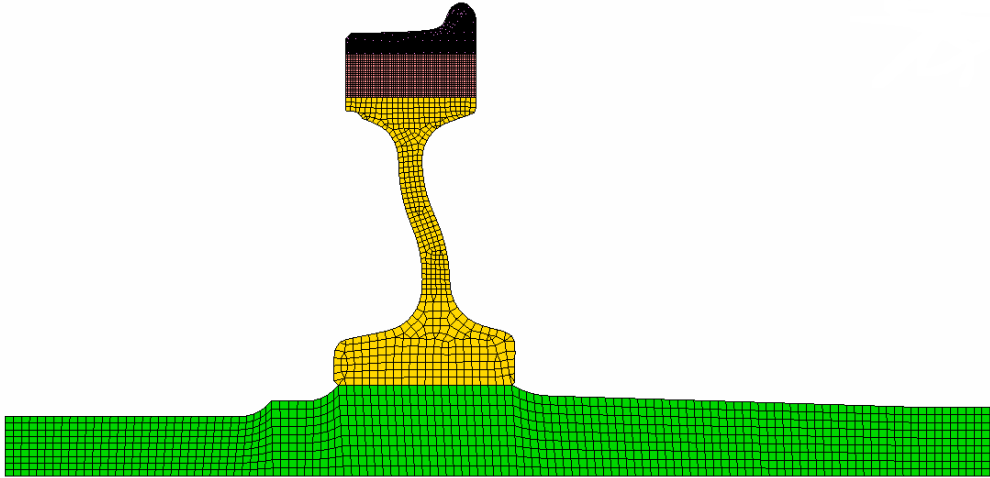
Figure 6.5: Interference simulation mesh

6.4.2   Results

As one would expect, the wheel hub is a lot more compliant in the radial direction than the solid axle, with the wheel accommodating between 73.2% and 84.4% of the total interference (see Figure 6.6). The average radial displacement of the inside hub surface of the wheel is 0.092 mm, which is 76.7% of the nominal interference.

For comparison, calculating the theoretical interference pressure between the axle and a simplified hub of outside diameter 300 mm yields a pressure of 93.6 MPa

6.5   Heat Transfer During Braking

The heat transfer associated with a braking event is dominated by four mechanisms. The first is the ratio of heat division between the brake blocks and the wheels. The second, which also accounts for the majority of the heat transfer, is the convection to the atmosphere. Thirdly, the heat transfer between the hot wheels and the, typically, cold rails also needs to be taken into account.
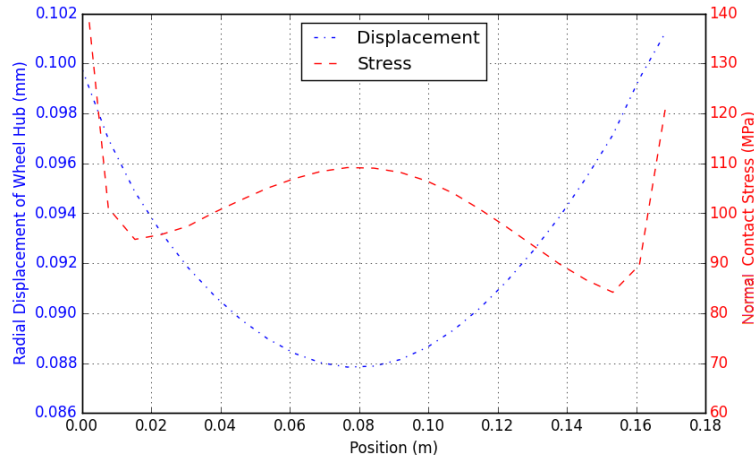
Figure 6.6: Interference fit results

Lastly, if temperatures are high enough, radiative heat transfer also needs to be taken into account.

6.5.1   Heat Partitioning at Braking

It is clear that some of the heat generated during braking will be absorbed by the brake blocks rather than the wheel. The fraction of the generated heat absorbed by the wheel can be estimated by (Vernersson, 2007a):

$$\beta = \left\{ 1 + \frac{k_b A_b}{k_w A_w} \sqrt{\frac{\kappa_w}{\kappa_b}} \right\}^{-1} \tag{6.5.1}$$

where k is the thermal conductivity, A is the swept area, κ is the thermal diffusivity, and subscripts b and w refer to the brake blocks and wheel.

With the dimensions of the contact face of the brake blocks at 280 mm long by 80 mm wide and using the taping line radius of the wheel of 431.5 mm, the heat partitioning can be calculated. Calculating the heat partitioning factor over the temperature range of Table 4.2 yields a maximum value (to the wheel) of 96.85% at 350°C and a minimum of 96.1% at 800°C. Given the small range of only 0.75%, the average value of 96.48% was used throughout the simulation. It is important to note that the Transnet standard specifies composite brake blocks, if the older style cast iron brake blocks were used the partitioning factor could be as low as 81% (Vernersson, 2007a).

6.5.2   Rail Chill

For a Hertzian contact patch of length a(in rolling direction) and width b under purely rolling contact of velocity v, Vernersson (2007a) showed that the upper

limit to the heat transfer from the wheel to the rail is

$$Q_{rc}^{perfect} \approx 6.99 \frac{bk}{\sqrt{\kappa}} \left(T_{w0} - T_{r0}\right) \sqrt{\frac{av}{8\pi}} \qquad (6.5.2)$$

with T_{w0} and T_{r0} the initial (prior to contact) wheel and rail surface temperatures.

The actual rail chill effect would depend on the specific wheel, track, and environmental conditions. Vernersson and Lunden (2007) found that the rail chill effect is very close to the perfect thermal contact levels during dynomometer tests. During two on track tests, they also obtained heat transfer rates of 90% and 70% of the perfect thermal contact.

Rail chill was incorporated in the axisymmetric model using the original area equivalent Hertzian representation of taping line contact from the FEM results. Two loads were also used; 9 tons, which is half of the axle load limit, and the 15 tons as prescribed by the Transnet standard for the mechanical (contact) simulations, which includes transient dynamic loads. For the 9 ton normal load, the heat transfer was also simulated at 70% of the perfect contact rate. Rail temperature was taken as 25°C.

6.6 Axisymmetric Braking Simulations

The braking cycles as described in Section 2.5.2 were applied to axisymmetric simulations where the effect of different simplifications were simulated in the absence of the mechanical contact load. The contact loading was ignored in order to allow axisymmetric simulations due to the extremely high computational cost associated with 3-dimensional simulations and the large number of simplifications investigated. The simplifications can be divided into three categories, these being heat transfer variations, stress state variations and material model variations.

6.6.1 FEA Model

The FEA model of the wheel is the same as in Section 6.4.1. Here the axle was not modelled and the effect of the interference fit was included by simply applying the measured radial displacement of the inside surface to the nodes. The model consisted of 5 327 elements and 5 646 nodes.

The braking flux is applied over an 80 mm wide band, starting at the most extreme field side node of the tread surface. Convection coefficients are calculated based on surface temperature and velocity.

6.6.2 Results

The different simplifications are compared to the nominal load case, which uses the CFD heat transfer data (Equations 5.3.1, 5.3.2, and 5.3.5 from Chapter 5),

96.48% of the braking energy is absorbed by the wheel, rail chill associated with perfect thermal contact and a 9 ton normal load on the taping line is included, the stress and strain state as at the end of the heat treatment is used as the initial state, axle interference is included, and the temperature dependent material model from Gordon and Perlman (with scaled yield stress) is combined with the creep model from Kuhlman *et al.* (1988). Since the only metrics mentioned in the standard are the axial displacement of the rim and the change in residual stress field, these were measured and compared to the nominal load case. The maximum uni-axial equivalent stress, maximum temperatures during the brake cycles, and the change (from the initial state as at the end of the heat treatment simulation) in equivalent plastic strain are also recorded to judge the metallurgical and structural safety of the wheel.

6.6.2.1   Drag-Stop Braking

Table 6.2 shows the effect of various thermal simplifications. The nominal load-case is as described earlier. The 100% loadcase refers to the heat partitioning at the braking interface, where all of the thermal energy is appropriated to the wheel and nothing to the brake block. *15T* refers to the effect of rail chill under an abnormal load of 15 tons, rather than 9 tons. *70% chill* shows the effect of heat transfer between the wheel and rail at 70% of perfect thermal contact rates. *No chill* refers to the absence of rail chill altogether. *Flat plate* refers to the convection coefficients employed where the wheel is modelled as a vertical flat plate in parallel flow only. Worst case thermal (*WCT*) combines the effect of 100% heat partitioning, no rail chill, and flat plate heat transfer coefficients. It also represents the simplest thermal boundary conditions and corresponds to the case most likely to be found in a report where the analyst did not have access to the relevant information.

The results for the drag-stop cycle under variations to the thermal boundary conditions are shown in Table 6.2 (axial displacement of the rim was taken as positive away from field side). From Table 6.2 it can be seen that the effect of omitting the rail chill effect and using the flat plate convection model are by far the most detrimental simplifications. It would stand to reason that the effect of heat partitioning at the braking interface would not have such a big impact on the results given the small fraction of heat extracted by the brake blocks. Assuming that all of the thermal energy is absorbed by the wheel, the maximum error relative to the nominal load case is with the maximum axial displacement, which is only 4.73% greater.

Between the *nominal* and *70% Chill* load cases we have produced a bounded solution of what can realistically be expected in the real world. With 70% of the rail chill, the maximum temperature increased by 6.91%, maximum equivalent stress increased by only 1.54%, and the maximum axial displacement of the rim increased by 11.89% (only 0.136 mm).

Table 6.2: Drag-stop thermal variation results

	Max Temp (°C)		Max σ_{eq} (MPa)		Max Displ. (mm)		$\triangle\epsilon_p(10^{-3})$
Nominal	378.6	% Diff	431.6	% Diff	1.146	% Diff	0.0
100%	391.8	3.49	431.6	0.00	1.200	4.73	0.0
15T	356.3	-5.88	431.5	-0.02	1.027	-10.38	0.0
70% Chill	404.8	6.91	438.3	1.54	1.282	11.89	0.0
No Chill	512.1	35.26	570.7	32.23	1.637	42.91	0.0
Flat Plate	444.4	17.38	501.6	16.22	1.388	21.17	0.0
WCT	631.8	66.88	629.0	45.75	1.936	68.94	0.541

Figure 6.7 shows the evolution of the residual stress due to one complete drag-stop braking cycle for thermal boundary condition variations. Variations with no appreciable effect were omitted from the figure. Figure 6.7 shows that the most simplistic thermal boundary condition, *worst case thermal*, completely wipes out the beneficial compressive residual stress in the rim. If this was a realistic expectation, it would have been a cause for concern as it would render the wheel more susceptible to fatigue fractures in the rim. Worth noting is that *70% chill* produced no discernible difference to the nominal load case, using perfect thermal contact.
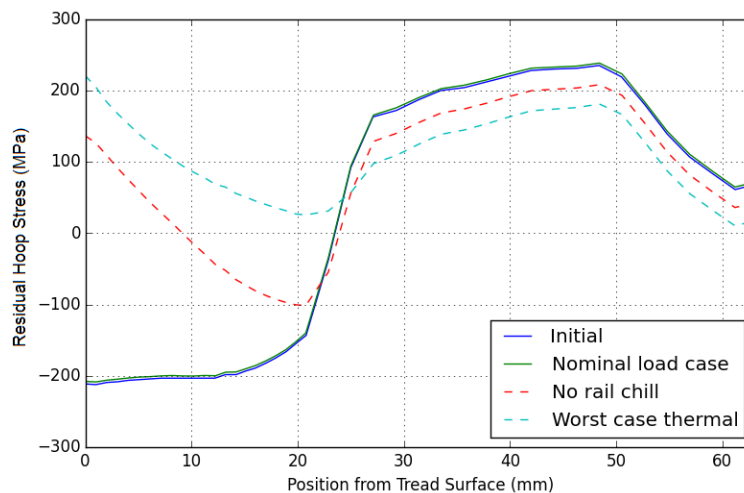
Figure 6.7: Drag-stop thermal variation residual stress evolution

Table 6.3 shows the effect of two mechanical variations. The first being the absence of the initial state (dominated by the residual stress) as found at the end of the heat treatment. The second, *no interference*, refers to the absence of the interference fit between the wheel and the axle. Both simplifications showed a reduction in the maximum uni-axial equivalent (Von Mises) stress encountered during the brake cycle and a slight increase in the axial displacement of the wheel flange.

Table 6.3: Drag-stop stress variation results

	Max σ_{eq} (MPa)		Max Displ. (mm)	
	431.6	**% Diff**	**1.146**	**% Diff**
Nominal	**431.6**	**% Diff**	**1.146**	**% Diff**
No Initial	359.4	-16.73	1.174	2.49
No Interference	421.4	-2.37	1.227	7.06

Figure 6.8 shows the residual stress profile in the rim if the initial stress state is ignored. Only a small tensile stress is developed. The effect of omitting the axle interference on the residual hoop stress in the rim is negligible.

Figure 6.8: Drag-stop mechanical variation residual stress evolution

Table 6.4 shows the effect of various simplifications to the material model. The simplifications shown are all assuming temperature invariance of some parameter of the material model where the values associated with the lowest temperature in Tables 4.1 and 4.2 were used. The CTE values in Table 4.2 are unusual, particularly for the lower temperatures. As such, a value much closer to the higher temperature values and a common value for steel was used, being 12 µm/m.K. *Temp Invariant* shows the results associated with the entire material model being temperature invariant as well as excluding viscoelastic creep.

Due to the relatively low temperatures associated with the nominal load case during the drag-stop cycle, the effect of these were all relatively small. Some simplifications were not included in the table since they showed no effect on the parameters monitored. These were an isotropic hardening model, perfect plastic, temperature invariant yield stress (no effect because of no yielding), no creep (no effect because of the low temperatures at the critical locations), and temperature invariant Poisson's ratio, which had no real

effect because of the small changes to Poisson's ratio at the relatively low temperatures encountered.

None of these simplifications produced an appreciable change to the residual stress profile in the rim.

Table 6.4: Drag-stop material property variation results

	Max Temp (°C)		Max σ_{eq} (MPa)		Max Displ. (mm)		$\triangle\epsilon_p(10^{-3})$
Nominal	**378.6**	**% Diff**	**431.6**	**% Diff**	**1.146**	**% Diff**	**0.0**
Const. CTE	378.6	0.00	621.8	44.07	1.795	56.68	0.0
Const. Cp	392.3	3.61	431.6	0.00	1.205	5.20	0.0
Const. k	348.4	-7.97	431.5	-0.02	1.071	-6.50	0.0
Const. Young's	378.6	0.00	444.7	3.04	1.164	1.62	0.0
Temp Invariant	359.3	-5.10	620.8	43.83	1.797	56.80	0.0

To investigate the sensitivity of these simplifications to the material model at higher temperatures, the simulations were repeated under the *worst case thermal* boundary conditions (see Table 6.5). The results monitored here still seem to be fairly insensitive to simplifications in this model, with the most important parameters to incorporate accurately being the coefficient of thermal expansion and creep. The most detrimental single simplification was a temperature invariant coefficient of thermal expansion, producing an error on the maximum uni-axial equivalent stress (relative to *WCT*) of 8.62% and 33.52% for the maximum axial displacement. This is somewhat expected due to the unusual CTE values listed in Table 4.2 (and the deviation from that with a more realistic constant value). As can be expected, when the material model is completely temperature invariant, the results do deteriorate significantly, with an error on the maximum axial displacement of 66.83% and nearly seven times the maximum additional plastic strain compared to *WCT*. Keeping the Poisson ratio and initial yield stress temperature invariant still did not produce any appreciable effect on the parameters monitored.

Table 6.5: Drag-stop material property variation under WCT conditions

	Max Temp (°C)		Max σ_{eq} (MPa)		Max Displ. (mm)		$\triangle\epsilon_p(10^{-3})$
WCT	**631.8**	**% Diff**	**629.0**	**% Diff**	**1.936**	**% Diff**	**0.541**
Isotropic	631.8	0.00	639.3	1.63	1.934	-0.08	0.453
Perfect Pl	631.8	0.00	626.6	-0.38	1.938	0.13	0.779
No Creep	633.3	0.24	636.7	1.22	2.078	7.34	2.013
Const. CTE	632.0	0.03	683.3	8.62	2.585	33.52	2.150
Const. Cp	675.5	6.92	635.2	0.97	2.043	5.54	0.754
Const. k	563.4	-10.82	626.5	-0.41	1.847	-4.59	0.367
Const. Young's	633.4	0.25	636.6	1.21	1.981	2.32	0.795
Temp Invar.	596.9	-5.52	724.3	15.15	3.171	63.83	3.751

The residual stress evolution for material model simplifications under *WCT* conditions are shown in Figure 6.9. The curves for isotropic hardening, perfect plastic, temperature invariant yield, and constant Poisson's ratio were omitted as they produced no appreciable difference compared to *WCT*. The nominal load case is also shown for comparison with the temperature invariant material model; it is interesting that combining a temperature invariant material model with the simplest thermal condition produced hardly any difference to the residual hoop stress profile when compared to the nominal load case.
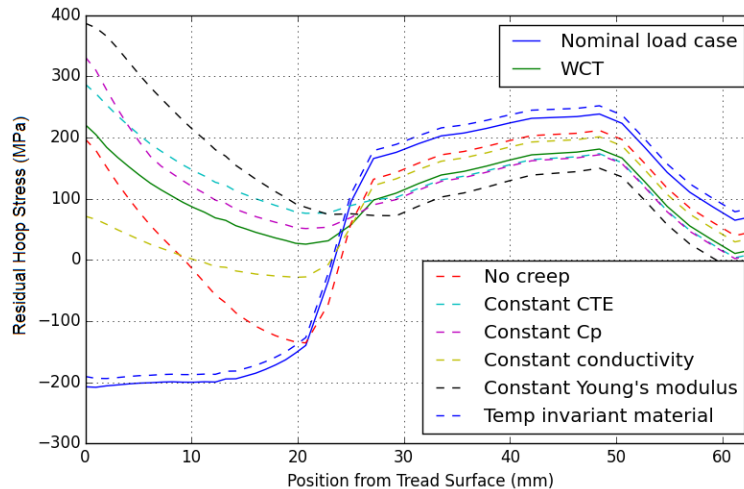
Figure 6.9: Drag-stop material property variation under WCT conditions

6.6.2.2   Drag Braking

The drag braking test is thermally a much more severe test for the wheel than the drag-stop cycle. For these simulations, deficiencies in the model can easily cause spurious concerns over the metallurgical, and by extension structural, integrity of the wheel.

Table 6.6 shows the effect for the thermal simplification under the drag braking cycle. Ignoring the rail chill effect, again, has the single most detrimental effect, followed by the flat plate heat transfer model. The bounded rail chill solution between perfect thermal contact and 70% of that produces a relatively narrow band with a maximum error of 8.12% on the maximum equivalent stress.

Figure 6.10 shows the residual stress evolution during one complete drag braking cycle under thermal boundary condition simplifications. Clearly, *no rail chill* is by far the most detrimental singe simplification in this group. It results in a complete reversal of the compressive residual stress in the rim, with a 200 MPa tensile stress at the tread surface.

Table 6.6: Drag braking thermal variation results

	Max Temp (°C)		Max σ_{eq} (MPa)		Max Displ. (mm)		$\triangle\epsilon_p(10^{-3})$
Nominal	**433.2**	**% Diff**	**549.4**	**% Diff**	**1.524**	**% Diff**	**0.0**
100%	448.1	3.44	567.9	3.37	1.567	2.82	0.0
15T	404.8	-6.56	504.3	-8.21	1.393	-8.60	0.0
70% Chill	466.3	7.64	594.0	8.12	1.635	7.28	0.0
No Chill	603.0	39.20	632.2	15.07	2.025	32.87	0.754
Flat Plate	514.7	18.81	625.3	13.82	1.747	14.63	0.292
WCT	747.9	72.65	650.8	18.46	2.375	55.84	1.354
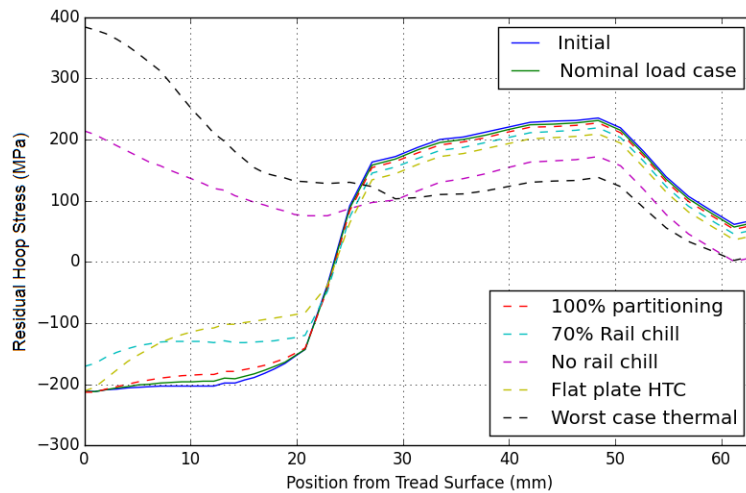
Figure 6.10: Drag braking thermal variation residual stress evolution

Table 6.7 shows the effect of simplifications to the stress state of the wheel. Ignoring the residual stress shows a much smaller influence on the maximum equivalent stress during the drag braking cycle than under drag-stop braking conditions. During the drag braking cycle, neither of these simplifications produced an error of more than 10%.

Table 6.7: Drag braking stress variation results

	Max σ_{eq} (MPa)		Max Displ. (mm)	
Nominal	**549.4**	**% Diff**	**1.524**	**% Diff**
No Initial	538.2	-2.04	1.640	7.61
No Interference	569.9	3.73	1.597	4.79

Figure 6.11 shows the residual stress profile in the rim if the initial stress state is ignored. As with the drag-stop cycle, the effect of omitting the axle interference on the residual stress in the rim is negligible.
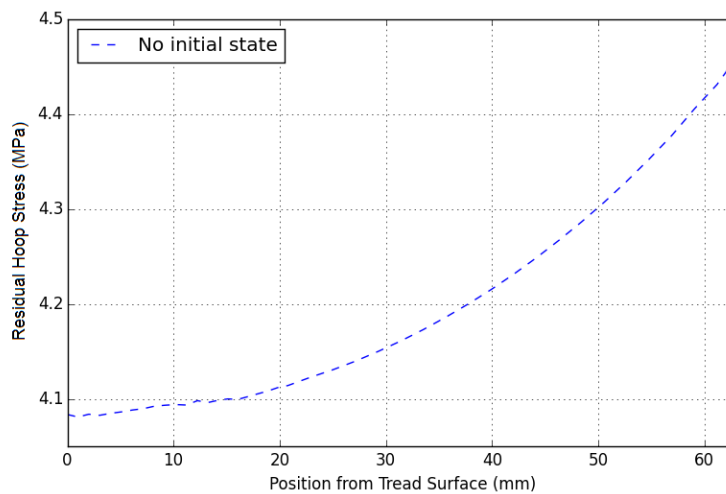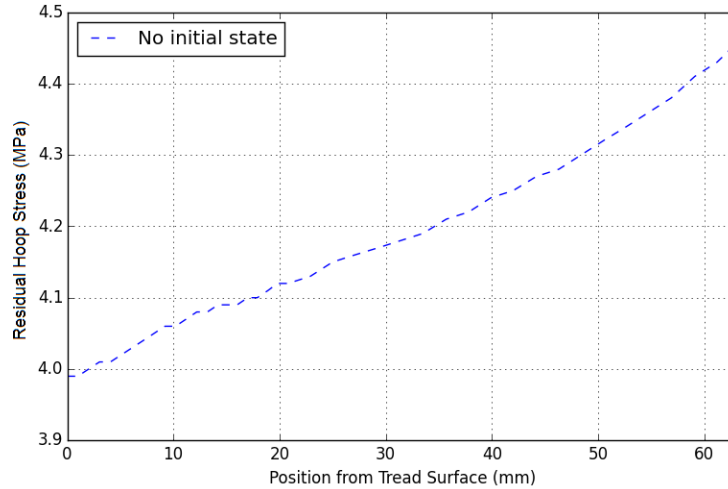
Figure 6.11: Drag braking mechanical variation residual stress evolution

Table 6.8 shows the effects of simplifications to the material model. Despite the higher temperatures than what is seen in the drag-stop cycle, the effect of these simplifications were still relatively minor, except for *constant CTE* which increased maximum equivalent stress by 18.17% and maximum axial displacement by 45.93%. Some simplifications were not included in the table since they showed no effect on the parameters monitored. These were an isotropic hardening model, perfect plastic, temperature invariant yield stress (no effect because of no yielding), and temperature invariant Poisson's ratio, which again had no real effect because of the small changes to Poisson's ratio in the temperature range encountered.

Table 6.8: Drag braking material property variation results

	Max Temp (°C)		Max σ_{eq} (MPa)		Max Displ. (mm)		$\triangle\epsilon_p(10^{-3})$
		% Diff		% Diff		% Diff	
Nominal	**433.2**	**% Diff**	**549.4**	**% Diff**	**1.524**	**% Diff**	**0.0**
No Creep	433.2	0.0	559.8	1.89	1.591	4.40	0.0
Const. CTE	433.2	0.0	649.2	18.17	2.224	45.93	1.249
Const. Cp	433.0	-0.05	567.0	3.20	1.554	1.97	0.0
Const. k	397.4	-8.26	537.9	-2.09	1.453	-4.66	0.0
Const. Young's	433.2	0.0	565.9	3.00	1.524	0.0	0.0
Temp Invariant	406.1	-6.26	656.0	19.40	2.279	49.54	1.551

Unlike under the drag-stop cycle, material model simplifications do produce a slight change to the residual stress pattern after a complete drag braking schedule (see Figure 6.12). The curves relating to changes to the plastic behaviour of the material as well as constant Poisson's ratio were omitted as they are coincident with the *nominal load case* curve.
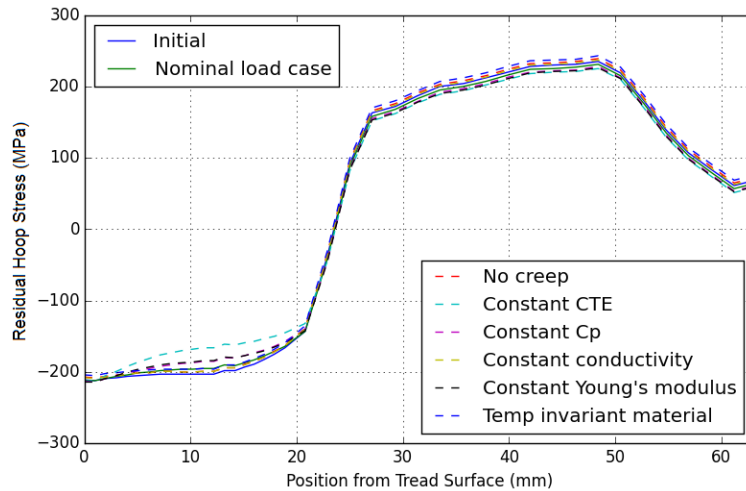
Figure 6.12: Drag braking material variation residual stress evolution

The simulations were repeated under the *worst case thermal* boundary conditions (see Table 6.5) to investigate the effects under higher temperatures. The results remained fairly insensitive to simplifications in this model with the effect of *constant CTE* actually reducing.

Table 6.9: Drag braking material property variation under WCT conditions

	Max Temp (°C)		Max σ_{eq} (MPa)		Max Displ. (mm)		$\triangle\epsilon_p(10^{-3})$
		% Diff		% Diff		% Diff	
WCT	747.9		650.8		2.375		1.354
Isotropic	747.9	0.00	663.0	1.87	2.379	-0.05	1.327
Perfect Pl	747.9	0.00	618.5	-4.96	2.389	0.05	1.882
No Creep	747.9	0.00	668.2	2.67	2.335	14.00	3.163
Const. Yield	747.9	0.00	648.6	-0.34	2.412	1.56	1.414
Const. CTE	748.2	0.04	676.8	4.00	2.972	35.40	2.133
Const. Cp	781.3	4.47	624.3	-4.07	2.366	5.21	1.414
Const. k	665.5	-11.02	651.7	0.14	2.358	-5.21	1.253
Const. Young's	747.9	0.00	658.6	1.20	2.489	1.54	1.428
Const. Poisson	747.9	0.00	651.1	0.05	2.383	0.22	1.357
Temp Invar.	695.4	-7.02	819	25.85	4.094	54.72	4.640

The residual stress evolution for material model simplifications under *WCT* conditions are shown in Figure 6.13. The curves for isotropic hardening, perfect plastic, and constant Poisson's ratio were omitted as they produced no appreciable difference compared to *WCT*.
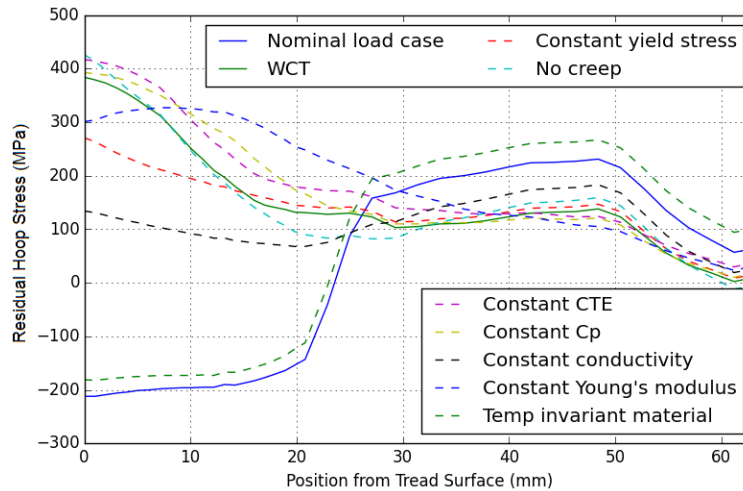
Figure 6.13: Drag braking material property variation under WCT conditions

6.7 3D Braking Simulations

To include the contact loads in the analysis, some of the simulations were repeated on a one-half symmetrical three dimensional model. This was also used as an opportunity to compare the axisymmetric results with the 3D results.

6.7.1 FEA Model

As with the axisymmetric investigation, the axle was not modelled and the effect of the interference fit was included by applying a radial displacement to the inside surface of the hub. Contact loads were also not simulated explicitly as contact with a rail, but rather applied as a pressure loading corresponding to the original area equivalent Hertzian load corresponding to the FEM results. This was done to achieve a much needed reduction in computational cost, but it should be noted that in the presence of plastic deformation at the surface, this method cannot provide quantitative results. Futhermore, the effect of the lower Young's modulus at higher temperatures on the contact mechanics is not taken into account with this method.

The model consisted of 999 930 elements (predominately 8 noded hexahedral) and 1 060 706 nodes.

6.7.2 Results

In order to reduce the required storage, not every increment of the temporal non-linear simulation was saved. For this reason, it is not practical to compare the maximum values achieved throughout the entire process. Instead, for the drag-stop simulation the comparison is made at 5 470 seconds, which

coincides with the point at the end of the last drag braking section just before the deceleration starts. For drag braking, the comparison is made at 18 900 seconds, which is the point when the last brake application terminates.

6.7.2.1   3-Dimensional to Axisymmetric Comparison

Firstly, the correlation between the 3-dimensional and axisymmetric models were investigated. For this purpose, the braking analyses were performed with the 3-dimensional model without the contact loads applied. Since the residual stress pattern was mapped to the 3-dimensional model from axisymmetric results, the comparison was done with the initial state included and excluded to ascertain if there are any marked discrepancies. The results are shown in Table 6.10.

Table 6.10: Axisymmetric to 3-dimensional comparison

	Load Case	Max Temp (°C)		Max σ_{eq} (MPa)		Max Displ. (mm)	
Drag-Stop	Axi - No Initial	314.7	% Diff	323.4	% Diff	1.000	% Diff
	3D - No Initial	312.8	-0.61	319.2	-1.30	0.990	-1.00
	Axisymmetric	314.7	% Diff	390.8	% Diff	0.976	% Diff
	3D	314.3	-0.13	369.2	-5.53	1.005	2.97
Drag	Axi - No Initial	433.2	% Diff	538.2	% Diff	1.640	% Diff
	3D - No Initial	428.8	-1.02	528.3	-1.84	1.616	-1.46
	Axisymmetric	433.2	% Diff	549.0	% Diff	1.524	% Diff
	3D	428.2	-1.15	555.8	1.24	1.602	5.12

Table 6.10 shows that the inclusion of the initial state does degrade the correlation slightly. The largest discrepancies can be seen with the stress and displacement results for the drag-stop cycle, and the displacement results for the drag braking cycle. Notwithstanding this, the largest error is only 5.53% (using axisymmetric results as reference), associated with the maximum uniaxial equivalent stress during the drag-stop cycle.

6.7.2.2   Drag-Stop Braking

Next, the effect of the contact loads were investigated during the drag-stop braking schedule. The different load cases are compared to the 3-dimensional simulation without any contact (annotated as *3D No Contact* in Table 6.11). Note that the other contact conditions prescribed in the standard are generally transient. For this reason, the rail chill was still applied on the taping line, as if the wheel has been running on tangent track and then transitioned to one of the other contact conditions.

Table 6.11: Drag-stop contact results

	Max σ_{eq} (MPa)	Max Displ. (mm)	$\triangle\epsilon_p(10^{-3})$
3D No Contact	**369.2**	**1.005**	**0.0**
Flange Root	1238.0	1.372	22.31
Taping Line	427.9	1.067	0.0
Field Side	562.7	1.113	0.37
Flange Lateral	518.7	1.509	0.0

The contact loads did not have any discernible effect on the residual stress field, at least at the taping line where we have so far measured. The reason the taping line contact did not have any impact is simply due to the lack of yielding. The taping line contact is the contact condition resulting in the lowest stress state and in this simulation is also acting on the coldest part of the tread (due to rail chill remaining on the taping line). The presence of the residual stress and plastic strain fields seems to suppress the slight plastic deformation seen in the contact simulations for all contact locations except flange root contact.

The change in the residual hoop stress below the flange root and field side contact patches (the only contact loads that produce plastic deformation) is shown in Figure 6.14. Note that this does not necessarily represent a stable final residual stress (shakedown state) since the load is not traversed repeatedly but simply applied at a stationary point during the braking cycles and for flange root contact, free surface plastic deformation is present. Notwithstanding this, it can be seen that the contact loads increase the residual hoop stress directly beneath the contact loads.

6.7.2.3 Drag Braking

The contact loads were also applied to a drag braking cycle and the results are shown in Table 6.12. As with the drag stop cycle, the contact loads had no impact on the residual stress field at the taping line.

Table 6.12: Drag braking contact results

	Max σ_{eq} (MPa)	Max Displ. (mm)	$\triangle\epsilon_p(10^{-3})$
3D No Contact	**555.8**	**1.602**	**0.0**
Flange Root	1236.0	0.9088	20.38
Taping Line	567.6	1.675	0.0
Field Side	574.3	1.724	1.811
Flange Lateral	602.4	2.14	0.0

Similarly as with the drag-stop cycle, the plastic deformation caused by the contact is slightly suppressed by the residual stress and plastic strain fields, albeit less than with the drag-stop cycle. The residual hoop stress below the flange root and field side contact loads is shown in Figure 6.14.

(a) Flange root   (b) Field side
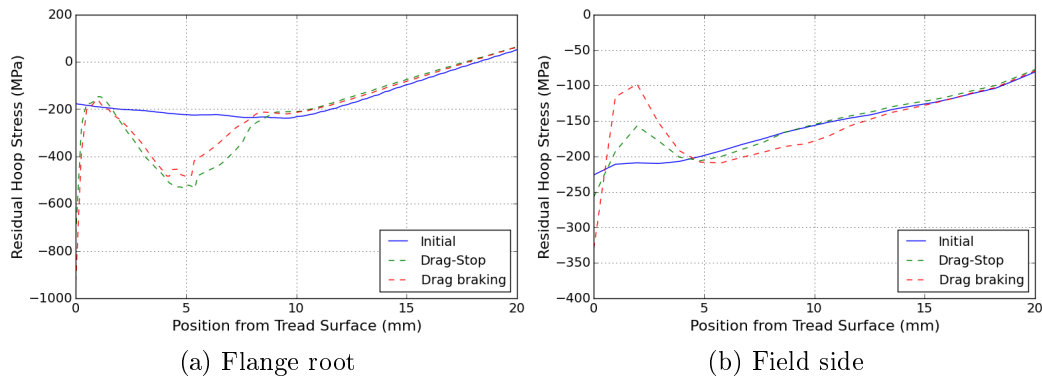
Figure 6.14: Change in residual hoop stress beneath contact

6.8   Conclusion

This chapter investigates the assumptions and simplifications sometimes encountered in finite element analyses of railway wheels. It also involved amalgamating all of the data gathered in the previous chapters to build a reference model where the contact stress is taken into account by using equivalent Hertzian representations, the residual stress produced by the heat treatment process is used as the initial state, and the heat transfer model as derived from CFD simulations is used to calculated the heat transfer due to convection.

By only looking at the equivalent stresses produced by the normal contact, we investigated which of the equivalent Hertzian methods replicate the original contact with the greatest fidelity. Judging by the elastic simulations, the BEM results appear to be closer to Hertzian than the FEM results and there is no appreciable difference between the two equivalent Hertzian implementations tested. When using the FEM results for elastic contact, keeping the contact stress equal to the source data provided better results, especially in the flange root and for lateral flange contact. From the simulations that included plasticity, it could be seen that the equivalent Hertzian contact still produced good results providing that the yielded volume remain fully surrounded by elastic material. When using the FEM results for plastic contact, retaining the original area provided better results.

The interference fit between the wheel and the axle was investigated next. As one would expect, the wheel is a lot more compliant that the solid axle and,

on average, accommodates 76.7% of the radial interference. When ignoring the edge effects, the maximum contact stress is just under 110 MPa.

Finally, the brake schedules from the Transnet standard were simulated with selected simplifications applied to the FEM model with each simulation. From the thermal boundary perspective, omitting the rail chill is by far the most detrimental simplification, followed by the use of the flat plate heat transfer coefficients instead of that obtained from the CFD simulations. As for mechanical variations, omitting the initial state shows an appreciable impact on the maximum equivalent stress encountered during drag-stop braking (much less during drag braking) and is of course crucial to the study of residual stress evolution. Ignoring the interference between the wheel and the axle is much less severe, but still causes an error of 7.06% on the maximum axial displacement of the rim during drag-stop braking.

Chapter 7

Concluding Remarks

7.1   Project Summary

The project investigated the effects of various simplifications and assumptions commonly employed when performing finite element (FE) analysis of railway wheels. The FE analysis focussed on was the analysis mandated by the Transnet Freight Rail (TFR) RS/ME/SP/008 and RS/ME/SP/021 standards. Before this analysis could be performed, the data required to obviate the usual simplifications and assumptions first had to be gathered.

The normal wheel/rail contact was simulated using both the FE method as well as the boundary element method (BEM). The BEM was furthermore used to gather data on the contact between the Transnet no. 22 wheel profile and the SAR 57 kg rail. This data was used to build a simple meta-model which can be used to determine equivalent Hertzian contact parameters for contact between the Transnet no. 22 profile and the SAR 57-kg rail under any reasonable normal load and wheel diameter.

In order to obtain the initial stress state from which the mandated FE analyses should start, the heat treatment process of the wheel had to be simulated. To my knowledge, the only standard for the validation of railway wheels explicitly calling for the residual stress to be considered is the AAR S-669 standard. To aid in the future use of that standard, as well as more prudent application of the other standards, the effect of various assumptions and simplifications were also investigated in relation to the heat treatment simulation itself.

The heat transfer from the wheel to the atmosphere was also investigated through computational fluid dynamics (CFD) simulations. The CFD data was compared to various published heat transfer models to ascertain whether some of these models provide a feasible alternative to CFD simulations. The CFD data was also fitted to a non-dimensional heat transfer model which allows the data to be used with more ease in any future work.

Finally, with all of the supporting data produced, the effects of various as-

79

sumptions and simplifications were investigated with respect to the FE analysis mandated by the TFR RS/ME/SP/008 and RS/ME/SP/021 standards.

7.2 Recommendations for Numerical Analysis of Railway Wheels

When performing the FEA as set out in the Transnet standard, it is recommended to apply an equivalent Hertzian load to avoid any spurious results from an arbitrarily applied load. Furthermore, it allows us to trust the analysis results much closer to the contact load. In the case of an elastic/plastic analysis, it is important to establish whether the plastic volume reaches the tread surface of the wheel. If this is the case, a non-linear FEA with explicit contact between the wheel and the rail should be done. The different equivalent Hertzian methods were evaluated using the peak equivalent stress as metric. When using the contact results from FE simulations, the original stress implementation produced more accurate results when an elastic response is assumed. For an elastic/plastic material model, the original area implementation produced superior results. When using the contact results from the BEM simulations, the two implementations produced much more similar results, with the original area implementation slightly more accurate for both elastic and elastic/plastic simulations.

It is also recommended that the standard considers the fatigue life of the wheel, in which case the residual stress from the heat treatment process should be included to properly account for the mean stress offset associated with it. Furthermore, it is important to include the residual stress state as the initial stress state for the braking simulations in order to predict whether the compressive stress is in any danger of being wiped out.

For the heat treatment simulations, phase transformation effects appeared to have the greatest impact on the residual stress field with the only unimportant effect being transformation induced plasticity. A complete temperature dependent material model with accurate strain hardening and creep behaviour is also important. Furthermore, the quenching heat transfer boundary condition and radiation showed a marked influence on the residual stress results.

Considering the convective heat transfer, the CFD work shows that the only viable published heat transfer model was that of a flat rotating disc in parallel flow. The agreement between that model and the CFD data also suggest that the specifics of the flow field is more important to capture than the specifics of the geometry. This would suggest it likely that the heat transfer model obtained in this project (and also that of a flat rotating disc in parallel flow) can be used for other axisymmetric railway wheels as well.

Finally, the effects of rail chill and a temperature dependent material model (including creep) are very important to the braking simulations as prescribed

by the Transnet standard.

7.3 Future Work

In order to improve the certainty of these simulations, it would be advisable to perform the simulations again using material data from one source (a specific material), preferably for the actual wheel being analysed. This holds especially true for the heat treatment simulations due to the complexities of the material model.

Since the TFR standards also call for the analyses to be performed on a worn wheel (at the condemning limit), a similar study should be done to determine whether the findings of this project hold for a worn wheel. When studying worn wheels, it would also be advisable to perform research on the shakedown behaviour of the residual stress field. This would ensure a realistic stress field is considered instead of assuming the stress field will still be as it was after heat treatment.

Due to the importance of the Young's modulus in the contact behaviour, it is desirable to perform a similar study as shown in Chapter 3 while taking the temperature dependence of the Young's modulus into account as well. This could allow more accurate representation of the contact load during the braking simulations where the wheel temperature can increase dramatically.

To improve the fidelity of the convective heat transfer model, it would be beneficial to study and preferably develop a predictive model that can capture the difference in train velocity and the free stream velocity experienced by the wheel.

Finally, fatigue should be used as one of the metrics to judge the differences between the different equivalent Hertzian implementations as well as the effect of omitting (or incorrectly simulating) the residual stress field.

Appendices

Appendix A

Contact Parametric Study Results

Table A.1: Contact parameterisation results

Contact Position		38.05	38.26	38.56	39	39.74	41.22	42.72	63.57	69.79
Contact Half-Length	m	0.018013	0.018081	0.018181	0.017915	0.01813	0.017941	0.017032	0.005443	0.005622
	n1	0.337011	0.336935	0.336468	0.336954	0.334159	0.334483	0.337082	0.332927	0.331828
	n2	0.401841	0.401055	0.400602	0.401794	0.404593	0.404346	0.406921	0.515727	0.512346
Contact Half-Width	m	0.081987	0.081904	0.080441	0.081537	0.080486	0.087438	0.078173	0.52024	0.516832
	n1	0.333872	0.334131	0.335863	0.335859	0.336454	0.331941	0.382094	0.334208	0.334641
	n2	-0.19683	-0.19677	-0.19642	-0.19749	-0.19477	-0.19704	-0.26205	-0.15346	-0.15262
Contact Area	m	0.004938	0.004952	0.004978	0.004934	0.004972	0.005013	0.005014	0.009301	0.0092
	n1	0.665142	0.665287	0.665132	0.665874	0.665762	0.664391	0.682707	0.665078	0.665188
	n2	0.207554	0.207168	0.20703	0.207663	0.207737	0.210821	0.181314	0.361125	0.362867
Peak Stress	m	309.525	308.524	304.4325	308.6102	307.4492	306.2527	296.9476	165.4025	165.7013
	n1	0.33315	0.332823	0.33289	0.332894	0.332722	0.332486	0.333295	0.333366	0.333512
	n2	-0.20674	-0.20572	-0.20418	-0.2069	-0.20697	-0.20803	-0.20696	-0.36179	-0.36264
Contact Position		**72.91**	**79.17**	**82.51**	**85.43**	**87.41**	**90.41**	**93.41**	**96.41**	**99.41**
Contact Half-Length	m	0.005409	0.005135	0.006777	0.007885	0.007822	0.007869	0.007822	0.007731	0.007731
	n1	0.334071	0.347228	0.331535	0.331234	0.336683	0.337179	0.336683	0.336503	0.336503
	n2	0.514254	0.502339	0.499074	0.488237	0.480523	0.47872	0.480523	0.482819	0.482819
Contact Half-Width	m	0.517554	0.615904	0.403047	0.248133	0.315234	0.357608	0.346278	0.346278	0.358306
	n1	0.32595	0.300096	0.342237	0.386365	0.352025	0.334421	0.337168	0.337168	0.33444
	n2	-0.13819	-0.13815	-0.16738	-0.20615	-0.19364	-0.18358	-0.1833	-0.1833	-0.18375
Contact Area	m	0.009365	0.011265	0.008776	0.007127	0.008856	0.009256	0.009197	0.00919	0.009254
	n1	0.661395	0.641255	0.670597	0.698118	0.673279	0.664978	0.665545	0.665498	0.665368
	n2	0.366562	0.361751	0.333431	0.29104	0.294692	0.301941	0.301996	0.302227	0.301349
Peak Stress	m	165.8365	107.317	147.4228	178.0851	165.7669	165.183	165.2006	165.2436	165.3999
	n1	0.333768	0.375774	0.339357	0.323211	0.332444	0.333427	0.333312	0.333322	0.333303
	n2	-0.36328	-0.36115	-0.31674	-0.2964	-0.30024	-0.30164	-0.30147	-0.30154	-0.30164
Contact Position		**102.41**	**105.41**	**108.42**	**111.42**	**114.4**	**116.42**	**118.42**	**120.38**	**121.32**
Contact Half-Length	m	0.007701	0.007701	0.007701	0.007701	0.007815	0.007815	0.007768	0.007061	0.007305
	n1	0.336159	0.336159	0.336159	0.336159	0.334874	0.334874	0.337447	0.349442	0.360578
	n2	0.484015	0.484015	0.484015	0.484015	0.483883	0.483883	0.480431	0.476199	0.453995
Contact Half-Width	m	0.358306	0.358306	0.356057	0.356057	0.35482	0.357597	0.437029	0.61875	0.468382
	n1	0.33444	0.33444	0.334582	0.334582	0.333918	0.339556	0.28591	0.243071	0.268911
	n2	-0.18375	-0.18375	-0.18304	-0.18304	-0.18126	-0.19232	-0.13434	-0.1346	-0.15262
Contact Area	m	0.009234	0.009236	0.009241	0.00921	0.009243	0.009401	0.00988	0.014917	0.012842
	n1	0.66549	0.665481	0.665411	0.665598	0.664898	0.666004	0.643338	0.59728	0.611857
	n2	0.301453	0.301405	0.301432	0.301641	0.302407	0.297684	0.327816	0.330248	0.315066
Peak Stress	m	165.4629	165.5206	165.5115	165.6195	165.6777	164.5679	175.6946	22.42122	67.15874
	n1	0.333301	0.333301	0.333348	0.333304	0.333334	0.333995	0.34026	0.577623	0.465017
	n2	-0.30167	-0.30171	-0.30178	-0.30179	-0.30202	-0.30226	-0.32276	-0.37097	-0.30775

Units of N, mm and MPa

Appendix B

LeBlond's Transformation Induced Plasticity Models

The different TRIP models (as summarised in Leblond (1989)) as used in this project is given below. Capital symbols show global or volume averaged values, while small symbols show microscopic values. E^{xx}/ε^{xx} show strain while E shows Young's modulus. Σ/σ represent stress, S is the global deviatoric stress tensor, and z is the product phase fraction. $h\left(\frac{\Sigma^{eq}}{\Sigma^{u}}\right)$ is defined in equation B.0.12 and $g(z)$ in Table A.1. Superscripts *th* relates to *thermal, eq* shows *equivalent* stress, *u* shows *ultimate* stress, and *y* relates to *yield*.

Perfect plastic:

$$\dot{E}^z = -\frac{3\Delta\varepsilon_{1\to2}^{th}}{\sigma_1^y}Sh\left(\frac{\Sigma^{eq}}{\Sigma^u}\right)(\ln z)\dot{z} \quad \text{if } z \leq 0.03 \tag{B.0.1}$$

$$\dot{E}^\Sigma = \frac{3(1-z)}{2\sigma_1^y}\frac{g(z)}{E}S\dot{\Sigma}^{eq} \tag{B.0.2}$$

$$\dot{E}^T = \frac{3(\alpha_1 - \alpha_2)}{\sigma_1^y}(\ln z)zS\dot{T} \tag{B.0.3}$$

Isotropic hardening:

$$\dot{E}^z = -\frac{3\Delta\varepsilon_{1\to2}^{th}}{\sigma_1^y(E_1^{eff})}Sh\left(\frac{\Sigma^{eq}}{\Sigma^y}\right)(\ln z)\dot{z} \quad \text{if } z \leq 0.03 \tag{B.0.4}$$

$$\dot{E}^\Sigma = \frac{3(1-z)}{2\sigma_1^y(E_1^{eff})}\frac{g(z)}{E}S\dot{\Sigma}^{eq} \tag{B.0.5}$$

$$\dot{E}^T = \frac{3(\alpha_1 - \alpha_2)}{\sigma_1^y(E_1^{eff})}(\ln z)zS\dot{T} \tag{B.0.6}$$

where E_1^{eff} is the effective (uniaxial equivalent) plastic strain of the first phase.

Kinematic hardening:

$$A_{1/2} = H_{1/2}(T)E^p_{1/2} \qquad\qquad \text{(B.0.7)}$$

$$A = (1-z)A_1 + zA_2 \qquad\qquad \text{(B.0.8)}$$

$$\dot{E}^z = -\frac{3\Delta\varepsilon^{th}_{1\to2}}{\sigma^y_1}(S-A)\,h\left(\frac{\Sigma^{eq}}{\Sigma^y}\right)(\ln z)\,\dot{z} \quad \text{if } z \le 0.03 \qquad\qquad \text{(B.0.9)}$$

$$\dot{E}^\Sigma = \frac{3\,(1-z)}{2\sigma^y_1}\frac{g(z)}{E}(S-A)\,\dot{\Sigma}^{eq} \qquad\qquad \text{(B.0.10)}$$

$$\dot{E}^T = \frac{3\,(\alpha_1-\alpha_2)}{\sigma^y_1}(\ln z)\,z\,(S-A)\,\dot{T} \qquad\qquad \text{(B.0.11)}$$

where A is the back stress tensor and $H(T)$ is the strain hardening slope at
the given temperature.

Additional information:

$$h\left(\frac{\Sigma^{eq}}{\Sigma^u}\right) = \begin{cases} 1 & \text{for } \frac{\Sigma^{eq}}{\Sigma^u} \le 0.5 \\ 1 + 3.5\left(\frac{\Sigma^{eq}}{\Sigma^u} - 0.5\right) & \text{for } \frac{\Sigma^{eq}}{\Sigma^u} > 0.5 \end{cases} \qquad\qquad \text{(B.0.12)}$$

Table B.1: Values to $g(z)$

z	0	0.125	0.25	0.5	0.75	1.0
g(z)	0	2.53	4.0	2.76	1.33	1.0

Linear interpolation should be used
between data points.

Appendix C

MSC Marc User Defined Subroutines

C.1   Plastic Reset

The NEWSV subroutine was used to set the temperature at which the plastic strain tensor and equivalent plastic strain scalar are reset. It was also used for keeping track of the equivalent stress state at the end of the previous increment to calculate stress increment for the TRIP calculations.

```
      subroutine newsv(sv,layers,intpts,m,id)
#ifdef _IMPLICITNONE
      implicit none
#else
      implicit logical (a-z)
#endif
c     ** Start of generated type statements **
      integer id, intpts, layers, m, ii, kc, nn, iof
      real*8 sv, temp, OldPhase, stemp, prevsv, eqstrs
c     ** End of generated type statements **
      dimension sv(layers,intpts)

      include "elmcom.cmn"
      include "space.cmn"
      include "array2.cmn"
      include "heat.cmn"

c     * * * * * *

c     user routine for state variables

c     sv                  is the array of new values of this state variable;
c                         to be defined by you.

c     layers         is the number of layers through the thickness if
c                         this is a shell element,
c                         the number of points in the cross-section if it
c                         is a beam element.
c                         it is equal to 1 for a continuum element.

c     intpts         is the number of integration points in this element.

c     m                   is the user element number.
c                         the internal element number is obtained as
```

86

```
c                                      mint=ielint(m)

c        id                            is the state variable number as defined in the input.

c        * * * * * *

         if (id .EQ. 2) then
            do nn=1,intpts
               do kc=1,layers
c                 29 for second state variable
                  call elmvar(29,m,nn,kc,prevsv)
c                 9 for temperature
                  call elmvar(9,m,nn,kc,temp)
                    if (temp .LT. prevsv) then
                       sv(kc,nn) = 20.d0
                       iof=ieplas+lofr+(kc-1)+(nn-1)*nstrm2
                       varselem(iof)=0.d0
                       do ii=1,ndi+nshear
c                          CHECK THAT ENTIRE INDEX IS DEFINED!!!
c                          values beyond col-73 are cut off
                           iof=iepl+lofr+(kc-1)*(ndi+nshear)+(nn-1)*nstrm1*nstrm2+ii-1
                           varselem(iof)=0.d0
                       end do
                    else
                       sv(kc,nn) = prevsv
                    end if
               end do
            end do
         end if

         if (id .EQ. 3) then
            do nn=1,intpts
               do kc=1,layers
c                 47 for Equivalent Couchy Stress
                  call elmvar(47,m,nn,kc,eqstrs)
                  sv(kc,nn) = eqstrs
               end do
            end do
         end if

         return
         end
```

C.2   Transformation Induced Plasticity

Marc's ANEXP subroutine was used to implement the TRIP model developed by Leblond *et al.*. All three models (perfect plastic, isotropic hardening, kinematic hardening) were implemented. Due to the similarity of these models, only kinematic hardening is shown below.

```
      subroutine anexp(m,nn,kcus,t,tinc,coed,ndi,nshear,eqexp)
#ifdef _IMPLICITNONE
      implicit none
#else
      implicit logical (a-z)
#endif

c        ** Start of generated type statements **
      real*8 coed, eqexp, temp, rstr, rhyd, S, h, g, frac, fracinc, E
```

```
          real*8 t, tinc, tup, tlow, tdel, its, eqstrs, ystrs, trstrain, Ay
          real*8 transpl, strspl, tpl, texp, alpha1, alpha2, strsinc, A
          real*8 thstrn, expan, plstrn
          integer kcus, m, ndi, nn, nshear, i
c         ** End of generated type statements **
          dimension eqexp(6), coed(ndi), m(2), kcus(2), t(*), tinc(*)
          dimension rstr(6), S(6), transpl(6), strspl(6), tpl(6), texp(6)
          dimension expan(2), A(6), thstrn(6), plstrn(6)

      include "concom"
c         * * * * * *
c         user subroutine to define thermal expansion strain increments

c         m(1)         user element number
c         m(2)         internal element number
c         nn           integration point number
c         kcus(1)      layer number
c         kcus(2)      internal layer number
c         t            temperature
c         tinc         temperature increment
c         coed         thermal expansion coefficients for this point:
c                      - for isotropic (including hyperelastic) materials,
c                        coed(1) to coed(3) are all equal to the coefficient
c                        of thermal expansion given in the input file
c                      - for orthotropic materials, coed(1) to coed(3) are
c                        the coefficients of thermal expansion given in
c                        the input file
c                      - for anisotropic materials, coed(1) to coed(6) are
c                        the coefficients of thermal expansion given in
c                        the input file
c         ndi          number of direct components
c         nshear       number of shear components
c         eqexp        array of thermal expansion strain increments

c         **** USER CREATED VARIABLES ****
c         temp         temparory variable
c         rstr         Couchy stress
c         rhyd         Couchy hydrostatic stress
c         S            Couchy srtess deviator
c         h            Correction factor - LeBlond 1989_Part-1 eq.26
c         g            Correction factor - LeBlond 1986_Part-2 table 3
c         frac         product phase fraction
c         fracinc      product phase fraction increment
c         E            Elasticity modulus - LeBlond 1986 Hypothesis-1; elastic
c                      compliance of phases the same as the global
c         tup          upper temp of phase transformation
c         tlow         lower temp of phase transformation
c         tdel         temperature range of phase transformation
c         its            isotropic thermal strain component (classical
c                      thermal expansion)
c         eqstrs       equivalent (Cauchy) stress
c         ystrs        (Global) yield stress
c         trstrain     (spherical) transformation strain
c                      (linearised volume strain)
c         Ay           Auestenite yield stress
c         transpl      TRIP proportional to transformation rate
c         strspl       TRIP proportional to stress rate
c         tpl          TRIP proportional to temperature rate
c         exp          Thermal expansion (spherical tensor)
c         alpha1       Coefficient of thermal expansion, Austenite
c         alpha2       Coefficient of thermal expansion, Pearlite
c         strsinc      equivalent stress increment
c         plstrn       "Standard" equivalent plastic strain
```

```
c        A              Back stress tensor
c        thstrn         Thermal Strain tensor - Also used as TRIP tensor
c        expan          Vector containing upper and lower bound of
c                       linear expansion (CTE integral over temp)
c        plstrn         Plastic strain tensor

c        * * * * * *

         tup = 750.d0
         tlow = 700.d0
         tdel = tup-tlow
         frac = (tup-t(1))/(tdel)
         fracinc = -tinc(1)/tdel
         if (frac .GT. 0.03 .AND. frac .LE. 1) then
c        Prelimenaries
c          341 for Couchy stress tensor
           call elmvar(341,m,nn,kcus(2),rstr)
           rhyd = (rstr(1)+rstr(2)+rstr(3))/3.d0
           S = rstr - (/ rhyd, rhyd, rhyd, 0, 0, 0 /)
c          321 for plastic strain tensor
           call elmvar(321,m,nn,kcus(2),plstrn)
c          47 for equivalent Couchy stress
           call elmvar(47,m,nn,kcus(2),eqstrs)
c          7 for Plasticity table
c          For kinematic haredening the yield stress does not change with
c          plastic strain; plasticity is supressed by the backstress
           call tabva2((/ t(1), 0.d0 /), ystrs, 7, 0, 0)
           ystrs = ystrs*1e6
c        Austenitic yield stress and back stress calculated at upper
c        transformation temperature
c          371 for thermal strain tensor
           call elmvar(371,m,nn,kcus(2),thstrn)
c        Total 'genuine' thermal strain:
c          16 for integrated CTE
           call tabva2(t(1), expan(1), 16, 0, 0)
           call tabva2(870, expan(2), 16, 0, 0)
           temp = (expan(1)-expan(2))/1e6
           thstrn = thstrn - (/ temp, temp, temp, 0, 0, 0 /)
           thstrn = thstrn/(1.d0-(frac-fracinc))
c          7 for Plasticity table
           call tabva2((/ tup, 0.d0 /), Ay, 7, 0, 0)
           Ay = Ay*1e6
c          Aproximate A2 = A1 for eqstrs>ystrs
           do i=1,ndi+nshear
c            7 for Plasticity table
             call tabva2((/ tup, thstrn(i)+plstrn(i) /), A(i), 7, 0, 0)
             A(i) = A(i)*1e6-Ay
           end do
           if (eqstrs .LE. ystrs) then
             A = (1.d0-(frac-fracinc))*A
           end if

c        Transformation rate plasticity
           if (eqstrs .LE. 0.5*ystrs) then
             h = 1.d0
           else
             h = 1.d0 + 3.5*((eqstrs/ystrs)-0.5)
           end if
c          16 for integrated CTE
           call tabva2(tup, temp, 16, 0, 0)
           call tabva2(tlow, trstrain, 16, 0, 0)
           trstrain = trstrain - temp
c          Unit correction for CTE (1e-6)
```

```fortran
            transpl = -3*trstrain/Ay*(S-A)*h*LOG(frac)*fracinc/1e6

c        Stress rate plasticity
c           17 for LeBlond g(z)
            call tabva2(frac, g, 17, 0, 0)
c           3 for Elasticity modulus
            call tabva2(t, E, 3, 0, 0)
            E = E*1e9
c           39 for third state variable
c           call elmvar(39,m,nn,kcus(2),temp)
            strsinc = eqstrs-t(3)
            strspl = 3.d0/2.d0*(1-frac)/Ay*g/E*(S-A)*strsinc

c        Temperature rate plasticity
c           14 for Transformation CTE
c           room temperature (below 700) for pearlite and some
c           temp above 750 for austenite
            call tabva2(800, alpha1, 14, 0, 0)
            call tabva2(25, alpha2, 14, 0, 0)
c           Unit correction for CTE (1e-6)
            tpl = 3*(alpha1-alpha2)/Ay*frac*LOG(frac)*(S-A)*tinc(1)/1e6

c        Standard (spherical) thermal expansion
            its = coed(1)*tinc(1)
            texp = (/ its, its, its, 0, 0, 0 /)

c        Total Strain
            eqexp = texp - transpl - strspl - tpl
         end if
         return
         end
```

Appendix D

Spray Quenching Heat Transfer Correlations

Table D.1: Spray quenching heat transfer correlations from Hall *et al.* (1997)

Quenching (Boiling) Regime	Correlation
Film Boiling Regime	$q'' = 63.25\,\Delta T^{1.691}\,Q'^{-0.264}\,d_{32}^{-0.062}$
Point of Departure from Film Boiling	$\Delta T_{DFB} = 886.2\,Q'^{-0.192}\,U_m^{0.144}\,d_{32}^{0.0367}$ $q''_{DFB} = q''_{film\,boiling}\big|_{DFB} = 63.25\,\Delta T_{DFB}^{1.691}\,Q'^{-0.264}\,d_{32}^{-0.062}$ $= 6.100\times10^6\,Q'^{-0.589}\,U_m^{0.244}$
Film Wetting Regime	If $\Delta T_{DFB} \leq \Delta T_{MHF}$ or $q''_{MHF} \leq q''_{film\,boiling}\big|_{MHF}$, then film wetting regime does not exist. $q'' = q''_{MHF} + \dfrac{q''_{DFB} - q''_{MHF}}{\left(\Delta T_{DFB} - \Delta T_{MHF}\right)^3}\Big[\left(3\,\Delta T_{DFB} - \Delta T_{MHF}\right)\Delta T_{MHF}^2$ $- 6\,\Delta T_{DFB}\,\Delta T_{MHF}\,\Delta T + 3\left(\Delta T_{DFB} + \Delta T_{MHF}\right)\Delta T^2 - 2\,\Delta T^3\Big]$ $+ \dfrac{\partial q''}{\partial \Delta T}\Big|_{DFB}\dfrac{1}{\left(\Delta T_{DFB} - \Delta T_{MHF}\right)^2}\Big[-\Delta T_{DFB}\,\Delta T_{MHF}^2$ $+ \left(2\,\Delta T_{DFB} + \Delta T_{MHF}\right)\Delta T_{MHF}\,\Delta T - \left(\Delta T_{DFB} + 2\,\Delta T_{MHF}\right)\Delta T^2 + \Delta T^3\Big]$ $\dfrac{\partial q''}{\partial \Delta T}\Big|_{DFB} = \dfrac{\partial q''_{film\,boiling}}{\partial \Delta T}\Big|_{DFB} = 107.0\,\Delta T_{DFB}^{0.691}\,Q'^{-0.264}\,d_{32}^{-0.062}$ $= 1.164\times10^4\,Q'^{-0.397}\,U_m^{0.0995}\,d_{32}^{-0.0366}$
Point of Minimum Heat Flux	$\Delta T_{MHF} = 204.9\,Q'^{-0.066}\,U_m^{0.138}\,d_{32}^{-0.035}$ $q''_{MHF} = 3.324\times10^6\,Q'^{-0.544}\,U_m^{0.324}$ If film wetting regime does not exist, then $q''_{MHF} = q''_{film\,boiling}\big|_{MHF} = 63.25\,\Delta T_{MHF}^{1.691}\,Q'^{-0.264}\,d_{32}^{-0.062}$ $= 5.127\times10^5\,Q'^{-0.376}\,U_m^{0.233}\,d_{32}^{-0.121}$
Transition Boiling Regime	$q'' = q''_{CHF} - \dfrac{q''_{CHF} - q''_{MHF}}{\left(\Delta T_{CHF} - \Delta T_{MHF}\right)^3}\Big[\left(\Delta T_{CHF} - 3\,\Delta T_{MHF}\right)\Delta T_{CHF}^2$ $+ 6\,\Delta T_{CHF}\,\Delta T_{MHF}\,\Delta T - 3\left(\Delta T_{CHF} + \Delta T_{MHF}\right)\Delta T^2 + 2\,\Delta T^3\Big]$
Point of Critical Heat Flux	$\Delta T_{CHF} = 18.0\left[\left(\rho_g\,h_{fg}\,Q''\right)\left(\dfrac{\sigma}{\rho_f\,Q''^2\,d_{32}}\right)^{0.198}\right]^{1/5.55}$ $\dfrac{q''_{CHF}}{\rho_g\,h_{fg}\,Q''} = 122.4\left[1 + 0.0118\left(\dfrac{\rho_g}{\rho_f}\right)^{1/4}\left(\dfrac{\rho_f\,c_{p,f}\,\Delta T_{sub}}{\rho_g\,h_{fg}}\right)\right]\left(\dfrac{\sigma}{\rho_f\,Q''^2\,d_{32}}\right)^{0.198}$
Nucleate Boiling Regime	$q'' = 1.87\times10^{-5}\left(\Delta T\right)^{5.55}$
Onset of Single-Phase Cooling	$\Delta T_{OSP} = 13.43\,Re_{32}^{0.167}\,Pr_f^{0.123}\left(\dfrac{k_f}{d_{32}}\right)^{0.220}$
Single-Phase Cooling Regime	$Nu_{32} = 2.512\,Re_{32}^{0.76}\,Pr_f^{0.56}$

Units of the parameters: q'' [W m^{-2}], $\Delta T = T_s - T_f$ [°C], Q'' [m^3 s^{-1} m^{-2}], U_m [m s^{-1}], d_{32} [m], h [W m^{-2} K^{-1}], ρ_f [kg m^{-3}], ρ_g [kg m^{-3}], h_{fg} [J kg^{-1}], $c_{p,f}$ [J kg^{-1} K^{-1}], k_f [W m^{-1} K^{-1}], μ_f [N s m^{-2}], σ [N m^{-1}].

Dimensionless parameters: $Nu_{32} = h\,d_{32}/k_f$, $Pr_f = c_{p,f}\,\mu_f/k_f$, $Re_{32} = \rho_f\,Q''\,d_{32}/\mu_f$

Range of validity of the correlations:

$T_f = 23$ °C, $Q'' = 0.58\times10^{-3} - 9.96\times10^{-3}$ m^3 s^{-1} m^{-2}, $U_m = 10.1 - 29.9$ m s^{-1}, $d_{32} = 137\times10^{-6} - 1350\times10^{-6}$ m.

Properties: The fluid properties used in the correlations for the onset of single-phase cooling and the single-phase cooling regime are evaluated at the film temperature, $T_{film} = 0.5\left(T_s + T_f\right)$. The fluid properties used in the CHF correlations are evaluated at the fluid saturation temperature (Ref 17).

91

Appendix E

Non-Dimensional Heat Transfer Formulations

E.1 Combined Laminar/Turbulent Flow Over a Flat Plate

Consider

$$Nu_x = \frac{xh}{k} = CRe_x^m Pr^n$$

$$Re_x = \frac{\rho v x}{\mu}$$

The average heat transfer coefficient in a flow changing from laminar to turbulent at x_{cr}, corresponding to Re_{cr}, is given as:

$$h = \frac{1}{L}\left(\int_0^{x_{cr}} h_{x,lam}dx + \int_{x_{cr}}^{L} h_{x,turb}dx\right) \tag{E.1.1}$$

For local Nusselt numbers corresponding to laminar (subscript 1) and turbulent (subscript 2) heat transfer E.1.1 can be written as:

$$h = \frac{k}{L}\left(\int_0^{x_{cr}} \frac{1}{x}C_1 Re_x^{m_1} Pr^{n_1}dx + \int_{x_{cr}}^{L} \frac{1}{x}C_2 Re_x^{m_2} Pr^{n_2}dx\right) \tag{E.1.2}$$

Substituting for Reynolds number and collecting x yields:

$$h = \frac{k}{L}\left(C_1\left(\frac{\rho v}{\mu}\right)^{m_1} Pr^{n_1}\int_0^{x_{cr}} x^{(m_1-1)}dx + C_2\left(\frac{\rho v}{\mu}\right)^{m_2} Pr^{n_2}\int_{x_{cr}}^{L} x^{(m_2-1)}dx\right)$$

$$h = \frac{k}{L}\left(C_1\left(\frac{\rho v}{\mu}\right)^{m_1} Pr^{n_1}\frac{x_{cr}^{m_1}}{m_1} + C_2\left(\frac{\rho v}{\mu}\right)^{m_2} Pr^{n_2}\frac{L^{m_2}-x_{cr}^{m_2}}{m_2}\right) \text{ for } m_1,m_2 > 0$$

$$h = \frac{k}{L}\left(\frac{C_1}{m_1}Re_{cr}^{m_1}Pr^{n_1} + \frac{C_2}{m_2}\left(Re_L^{m_2}-Re_{cr}^{m_2}\right)Pr^{n_2}\right) \tag{E.1.3}$$

92

The average Nusselt over length L for flow changing from laminar to turbulent at Re_{cr} can thus be given as:

$$Nu_L = \frac{C_1}{m_1} Re_{cr}^{m_1} Pr^{n_1} + \frac{C_2}{m_2} \left(Re_L^{m_2} - Re_{cr}^{m_2} \right) Pr^{n_2} \qquad \text{(E.1.4)}$$

E.2 Combined Laminar/Turbulent Flow Over a Rotating Disk

Consider

$$Nu_r = \frac{rh}{k} = C Re_r^m Pr^n$$

$$Re_r = \frac{\rho \omega r^2}{\mu}$$

The average heat transfer coefficient in a flow changing from laminar to turbulent at r_{cr}, corresponding to Re_{cr}, is given as:

$$h = \frac{1}{R} \left(\int_0^{r_{cr}} h_{r,lam} dr + \int_{r_{cr}}^{R} h_{r,turb} dr \right) \qquad \text{(E.2.1)}$$

For local Nusselt numbers corresponding to laminar (subscript 1) and turbulent (subscript 2) heat transfer E.2.1 can be written as:

$$h = \frac{k}{R} \left(\int_0^{r_{cr}} \frac{1}{r} C_1 Re_r^{m_1} Pr^{n_1} dr + \int_{r_{cr}}^{R} \frac{1}{r} C_2 Re_r^{m_2} Pr^{n_2} dr \right) \qquad \text{(E.2.2)}$$

Substituting for Reynolds number and collecting r yields:

$$h = \frac{k}{R} \left(C_1 \left(\frac{\rho \omega}{\mu} \right)^{m_1} Pr^{n_1} \int_0^{r_{cr}} r^{(2m_1-1)} dr + C_2 \left(\frac{\rho \omega}{\mu} \right)^{m_2} Pr^{n_2} \int_{r_{cr}}^{R} r^{(2m_2-1)} dr \right)$$

$$h = \frac{k}{R} \left(C_1 \left(\frac{\rho \omega}{\mu} \right)^{m_1} Pr^{n_1} \frac{r_{cr}^{2m_1}}{2m_1} + C_2 \left(\frac{\rho \omega}{\mu} \right)^{m_2} Pr^{n_2} \frac{R^{2m_2} - r_{cr}^{2m_2}}{2m_2} \right) \quad \text{for} \quad m_1, m_2 > 0$$

$$h = \frac{k}{R} \left(\frac{C_1}{2m_1} Re_{cr}^{m_1} Pr^{n_1} + \frac{C_2}{2m_2} \left(Re_L^{m_2} - Re_{cr}^{m_2} \right) Pr^{n_2} \right) \qquad \text{(E.2.3)}$$

The average Nusselt over Radius R for flow changing from laminar to turbulent at Re_{cr} can thus be given as:

$$Nu_R = \frac{C_1}{2m_1} Re_{cr}^{m_1} Pr^{n_1} + \frac{C_2}{2m_2} \left(Re_R^{m_2} - Re_{cr}^{m_2} \right) Pr^{n_2} \qquad \text{(E.2.4)}$$

Appendix F

CFD Mesh Independence Study

F.1   CFD Validation Problem

The first step in the validation problem was to investigate the mesh independence of FloEFD, in particular its ability to accommodate very coarse meshes. Given the flow conditions listed in Table F.1, the boundary layer is expected to start transitioning from laminar to turbulent more or less midway down the flow path (based on $Re_{cr} \approx 5(10^5)$).

Table F.1: Mesh independence study flow conditions

Description	Value
Ambient Temperature (T_{inf})	20 °C
Wall Temperature (T_w)	30 °C
Free Stream Velocity (v)	15 m.s^{-1}
Turbulence Intensity (T)	1%
Turbulence Length Scale (l)	0.01 m

Eight different meshes were tested. The most coarse was 2x80 cells with each mesh refinement halving the nominal edge length to 16x640 cells for the fourth mesh. Thereafter all meshes contained 1000 cells in the flow direction (due to an initial mesh limit) from 32x1000 to 256x1000 cells. Figure F.1 shows that the meshes consisting of 160, 640, and 2 560 cells produce very similar results while the number of cells increase by a factor of 16. Continued refinement first produce seemingly plausible results, with only a lower critical Reynolds number than what is expected. Using finer meshes still, it can be seen that the critical Reynolds number does not achieve a second convergent point; instead the heat transfer characteristics significantly deviate from what is expected, given the experimental model.

FloEFD seems to produce more accurate results (at least when judged relative to published models) with the coarse meshes rather than very fine
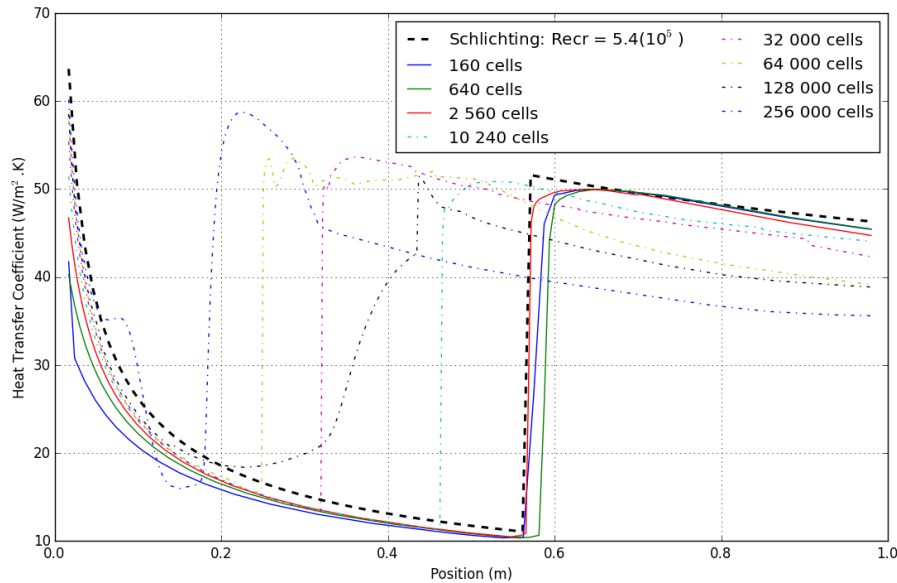
94

Figure F.1: Mesh independence for validation problem

meshes. Given that with the first three meshes, the number of cells increased by a factor of 16 without an appreciable difference in the results, it is clear that the solution is mesh independent for those three meshes.

Calculating the y^+ value of the wall adjacent cells shows that it is with the transition from the thin-boundary-layer approach to the thick-boundary-layer approach (at $y^+ \approx 300$ for the turbulent region) that the mesh independence is lost for the laminar/turbulent transition model. Unfortunately the technical reference does not elaborate on the specifics of how boundary layer transition is treated. Based on these results, care should be taken not to refine the mesh excessively as the thin-boundary-layer approach seems to produce much more accurate results and excessive mesh refinement (leading to the activation of the thick-layer model) could lead to erroneous data. Of course, the performance and validity of the mesh depends on the boundary layer thickness, or the y^+ value, and would not necessarily work for different flow conditions. Mesh independence needs to be reinvestigated if marked changes are made to flow conditions.

The third mesh, with 2 560 cells, was used for the validation problem work.

F.2   RailWay Wheel Study

Unlike with the two-dimensional validation problem, the spatial distribution of the heat transfer coefficient is not available and only the average heat transfer coefficient is available. Also the software cannot report the y^+ value directly and cannot be calculated for the 3D case based on the reported data.

Mesh independence was tested at two extreme values of turbulence in-

tensity, 1% and 50%. This was chosen to have a wide band around typical atmospheric conditions of 10 to 20% (Baldocchi, 2014). This wide band will serve to show whether the free stream turbulence intensity has a marked effect on the heat transfer. This is a pertinent question in that the free stream turbulence is *artificially* reduced by the superposition of the constant velocity of the train on the mean air velocity (increasing the determinant in equation 5.2.7). The free stream turbulence is then also expected to increase down the length of the train as the air stream is increasingly disturbed.

Three different velocities were tested. A stationary wheel, one travelling at low speed (20 km/h), and one travelling at high speed (80 km/h). Two extreme values of wall temperatures were also tested, 343 K ($\triangle T = 50°$C) and 993 K ($\triangle T = 700°$C). This was done to see whether there is one mesh that would be valid for the entire spectrum of simulations planned.

In terms of mesh refinement, three different basic meshes were used. Each refinement to the basic mesh constituted a halving of the edge length in all directions, thus an eight fold increase in the number of cells. On top of the basic mesh, fluid/solid interface cell refinement was also applied. Each level of interface refinement splits an original interface (boundary) cell in eight. For the mesh independence study, five different interface refinement levels were tested, level 0 (no refinement) through to level four (split four times). The mesh independence results are shown in Figure F.2.

In Figure F.2, each graph shows the average heat transfer coefficient for different simulations where only the mesh was altered. Thus, a clear deviation in the result of one simulation from the other simulations would suggest a mesh dependency problem. Similar to the validation problem, it seems that too much refinement causes spurious results. This can be seen by the sudden increases in the average HTC to the right of the graphs, showing higher levels of interface refinement.

Figures F.2c through F.2f show that there are only small differences in the HTC for the two extreme values of turbulence intensity, except where clear mesh dependency issues are present. As can be seen from the validation problem and Section 5.2.2.1, the influence of the free stream turbulence intensity on the heat transfer coefficient (through its effect on the critical Reynolds number) is much more severe at the low end of the spectrum than at the high end. Therefore, at the high turbulence intensity values encountered under atmospheric conditions, the heat transfer coefficient becomes almost independent from the turbulence intensity. This is a very useful property as it negates the need to account for the large variability in the turbulence intensity of atmospheric conditions as well as the fact that the last wheel on a train would encounter a more turbulent free stream than the first.

A turbulence intensity of 10% on the 80x60x20 grid with one level of fluid/solid interface refinement was used for the study. This mesh was chosen for its robust performance (resolving all flow conditions without any convergence difficulties) and relatively low computational cost.
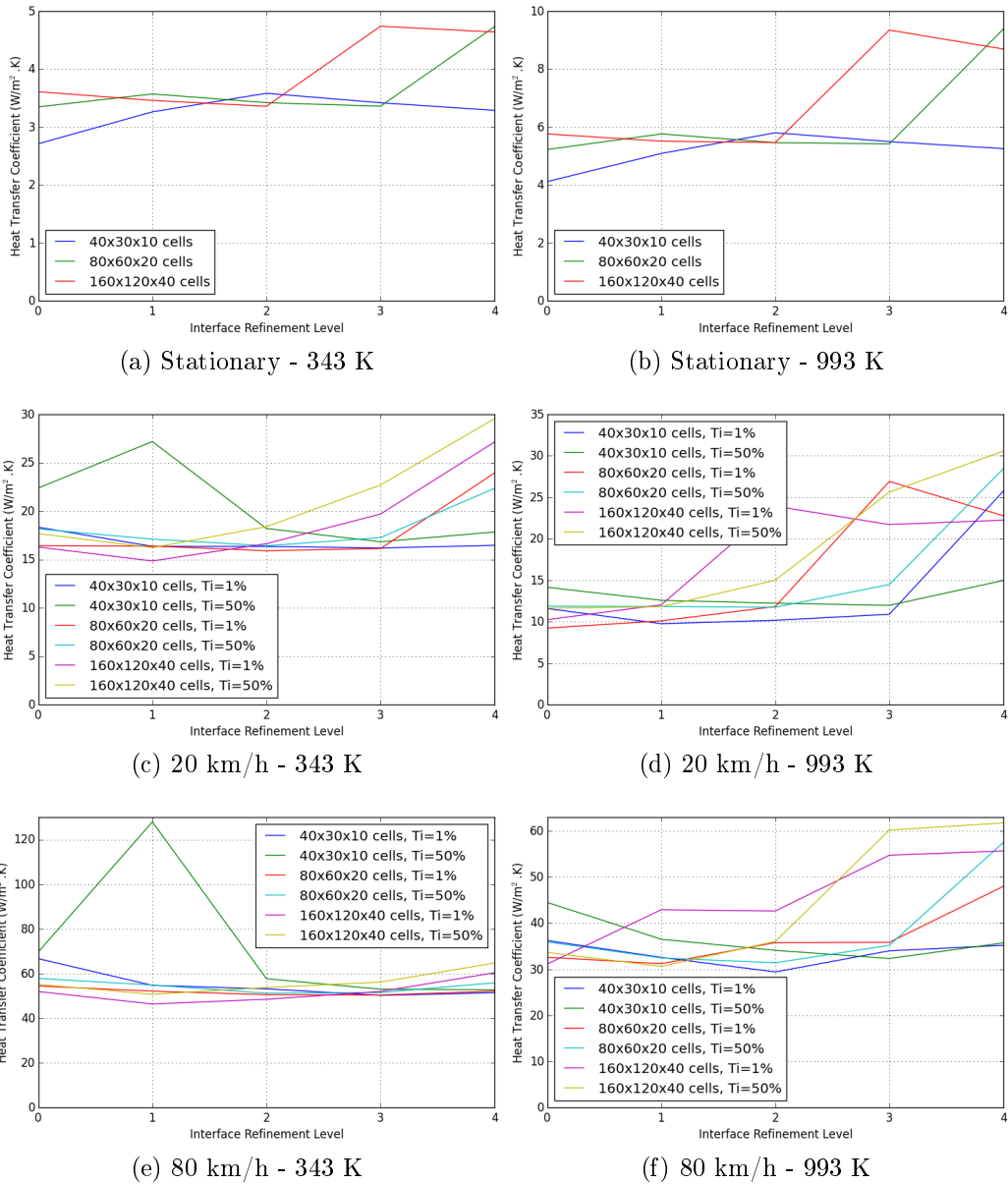
(a) Stationary - 343 K

(b) Stationary - 993 K

(c) 20 km/h - 343 K

(d) 20 km/h - 993 K

(e) 80 km/h - 343 K

(f) 80 km/h - 993 K

Figure F.2: Mesh independence

List of References

Aamir, M., Liao, Q., Hong, W., Xun, Z., Sihong, S. and Sajid, M. (2016). Transient heat transfer behavior of water spray evaporative cooling on a stainless steel cylinder with structured surface for safety design application in high temperature scenario. *Heat and Mass Transfer*, pp. 1–10.

Ariza, E.A., Martorano, M.A., De Lima, N.B. and Tschiptschin, A.P. (2014). Numerical simulation with thorough experimental validation to predict the build-up of residual stresses during quenching of carbon and low-alloy steels. *ISIJ International*, vol. 54, no. 6, pp. 1396–1405.

ASM International (1990). *ASM Handbook, Volume 01 - Properties and Selection: Irons, Steels, and High-Performance Alloys*. ASM International.

Association of American Railroads (2009). Standard s-660: Wheel design, locomotive and freight car - analytic evaluation.

Association of American Railroads (2011). Standard s-669: Analytical evaluation of locomotive wheel designs.

Aus der Wiesche, S. (2007). Heat transfer from a rotating disk in a parallel air crossflow. *International Journal of Thermal Sciences*, vol. 46, pp. 745–754.

Ayasse, J. and Chollet, H. (2005). Determination of the wheel rail contact patch in semi-hertzian conditions. *Vehicle System Dynamics*, vol. 43, no. 3, pp. 161–172.

Baldocchi, D. (2014). ESPM 129 biometeorology class notes - wind and turbulence, part 4.

Bromley, L.A. (1950). Heat transfer in stable film boiling. *Chem. Eng. Prog.*, vol. 46 (5), pp. 221–227.

BS EN 13979-1 (2011). Railway applications - wheelsets and bogies - monobloc wheels - technical approval procedure - part 1: Forged and rolled wheels.

Carter, F.W. (1926). On the action of a locomotive driving wheel. In: *Proc. R. Soc. Lond. A 1926 112*, pp. 151–157.

Cheng, W.-L., Zhang, W.-W., Chen, H. and Hu, L. (2016). Spray cooling and flash evaporation cooling: The current development and application. *Renewable and Sustainable Energy Reviews*, vol. 55, pp. 614–628.

Cobb, E.C. and Saunders, O.A. (1956). Heat transfer from a rotating disk. *Proceedings of the Royal Society A*, vol. 236, pp. 343–351.

Cuperus, J.L. and Venter, G. (2016*a*). Finite element analysis of the tread quenching of railway wheels. In: Kruger, J.-H. (ed.), *Proceedings of the 10th South African Conference on Computational and Applied Mechanics*.

Cuperus, J.L. and Venter, G. (2016*b*). Numerical simulation and parameterisation of rail/wheel normal contact. *Proceedings of the Institution of Mechanical Engineers, Part F: Journal of Rail and Rapid Transit*.

Dorfman, L.A. (1963). *Hydrodynamic Resistance and the Heat Loss of Rotating Solids*. Oliver & Boyd.

Dryden, H.L. (1936). Air flow in the boundary layer near a plate. Report 562, NACA.

Çengel, Y.A. and Ghajar, A.J. (1998). *Heat and Mass Transfer - Fundamentals and Applications*. McGraw-Hill.

Gaugler, R. (1966). *An experimental study of spray cooling of high temperature surfaces*. Ph.D. thesis, Carnegie Institute of Technology, Pittsburgh.

Gordon, J. and Perlman, A.B. (1998). Estimation of residual stresses in railroad commuter car wheels following manufacture. *Proceedings of the International Mechanical Engineering Congress and Exhibition, ASME RTD*, vol. 15, pp. 13–18.

Greenwood, G.W. and Johnson, R.H. (1965). The deformation of metals under small stresses during phase transformations. *Proceedings of the Royal Society A*, vol. 283, no. 1394, pp. 403–422.

Guo, R., Wu, J., Fan, H. and Zhan, X. (2016). The effects of spray characteristic on heat transfer during spray quenching of aluminum alloy 2024. *Experimental Thermal and Fluid Science*, vol. 76, pp. 211–220.

Ha, M.-T. and Kang, C.-G. (2012). Fatigue analysis of railway wheels according to uic standards. In: *12th International Conference on Control, Automation and Systems*.

Hall, D.D., Mudawar, I., Morgan, R.E. and Ehlers, S.L. (1997). Validation of a systematic approach to modeling spray quenching of aluminum alloy extrusions, composites, and continuous casting. *Journal of Materials Engineering and Performance*, vol. 6, no. 1, pp. 77–92.

Hertz, H. (1881). Über die berührung fester elastischer körper (on the contact of elastic solids). *Journal für die reine und angewandte Mathematik*, vol. 92, pp. 156–171.

Hettasch, G. and Fröhling, R. (2011). Geometric requirements for new, reprofiled and in-service wheelsets.

Johnson, K. (1989). The strength of surfaces in rolling contact. *Proceedings of the Institution of Mechanical Engineers*, vol. 203, pp. 151–163.

Johnson, K.L. (1982). One hundred years of hertz contact. *Proceedings of the Institution of Mechanical Engineers*, vol. 196, pp. 363–378.

Jung, M., Kang, M. and Lee, Y.-K. (2012). Finite-element simulation of quenching incorporating improved transformation kinetics in a plain medium-carbon steel. *Acta Materialia*, vol. 60, pp. 525–536.

Kalker, J.J. (1973). Simplified theory of rolling contact. *Delft Progress Report*, pp. 1–10.

Kalker, J.J. (1982). Two algorithms for the contact problem in elastostatics. In: *Proc. Int. Symp. on Contact Mechanics and Wear of Rail-Wheel Systems I Vancouver BC*.

Kalker, J.J. (1990). *Three-Dimensional Elastic Bodies in Rolling Contact*. Solid Mechanics and Its Applications. Springer.

Kalker, J.J. (1991). Wheel-rail rolling contact theory. *Wear*, vol. 144, pp. 243–261.

Kays, W., Crawford, M. and Weigand, B. (1966). *Convective Heat and Mass Transfer*. 4th edn. McGraw-Hill.

Kuhlman, C., Sehitoglu, H. and Gallagher, M. (1988). The significance of material properties on stresses developed during quenching of railroad wheels. *Proceedings of the Joint ASME IEEE Railroad Conference*, pp. 55–63.

Leblond, J.B. (1989). Mathematical modelling of transformation plasticity in steels ii: Coupling with strain hardening phenomena. *International Journal for Plasticity*, vol. 5, pp. 573–591.

Leblond, J.B., Devaux, J. and Devaux, J.C. (1989). Mathematical modelling of transformation plasticity in steels i: Case of ideal-plastic phases. *International Journal for Plasticity*, vol. 5, pp. 551–572.

Leblond, J.B., Mottet, G. and Devaux, J.C. (1986a). A theoretical and numerical approach to the plastic behaviour of steels during phase transformations - i. derivations of general relations. *Journal of the Mechanics and Physics of Solids*, vol. 34, no. 4, pp. 395–409.

Leblond, J.B., Mottet, G. and Devaux, J.C. (1986b). A theoretical and numerical approach to the plastic behaviour of steels during phase transformations - ii. study of classical plaplastic for ideal-plastic phases. *Journal of the Mechanics and Physics of Solids*, vol. 34, no. 4, pp. 411–432.

Lement, B.S. (1959). *Distortion in tool steels*. American Society for Metals.

Mackerle, J. (2003). Finite element analysis and simulation of quenching and other heat treatment processes - a bibliography (1976-2001). *Computational Material Science*, vol. 27, pp. 313–332.

Matjeke, V.J. and Mabaso, F.G. (2011). Transnet freight rail specification for the supply of cast wheel for trailing stock.

Mentor Graphics (2011). Enhanced turbulent modeling in floefd. Tech. Rep..

Mentor Graphics (2013). *FloEFD Technical Reference - Software Version 13.* Mentor Graphics.

MG-Valdunes (nd). Mg-valdunes plaquette. Online.

Nukiyama, S. (1934). The maximum and minimum values of heat trasnmitted from metal to boiling water under atmospheric pressure. *Journal of Japan Society of Mechanical Engineers*, vol. 37, pp. 367–374.

Okagata, Y. (2013). Design technologies for railway wheels and future prospects. Tech. Rep., Nippon Steel & Sumitomo Metal.

Pascal, J. and Sauvage, G. (1992). New method for reducing the multicontact wheel/rail problem to one equivalent contact patch. *Vehicle System Dynamics*, vol. 20:sup1, pp. 475–489.

Piotrowski, J. and Kik, W. (2008). A simplified model of wheel/rail contact mechanics for non-hertzian problems and its application in rail vehicle dynamic simulations. *Vehicle System Dynamics*, vol. 46, pp. 27–48.

Pohlhausen, E. (1921). Der wärmeaustausch zwischen festen körpern und flüssigkeiten mit kleiner reibung und kleiner wärmeleitung. *Zeitschrift für Angewandte Mathematik und Mechanik (Journal of Applied Mathematics and Mechanics)*, vol. 1 (2), pp. 115–121.

Portesi, M., Gallo, R. and Lombardo, F. (2005). Solid wheel for metro - south africa spoornet ringrollers - fem calculation report. Tech. Rep., Lucchini Sidermeccanica.

PRASA Rail Chair for Maintenance and Engineering Management (2012). Test report for chinese wheels R&D project part 1 - trailer coach wheels. Tech. Rep., PRASA.

Rammerstorfer, F.G., Fischer, D.F., Mitter, W., Bathe, K.J. and Snyder, M.D. (1981). On thermo-elastic-plastic analysis of heat-treatment processes including creep and phase changes. *Computers & Structures*, vol. 13, pp. 771–779.

Schlichting, H. (1955). *Boundary-Layer Theory.* 6th edn. McGraw-Hill.

Schubauer, G.B. and Skramstad, H.K. (1943). Laminar boundary layer oscilations and transition on a flat plate. Advanced confidential report, NACA.

Simsir, C. and Gür, C.H. (2008). 3D FEM simulation of steel quenching and investigation of the effect of asymmetric geometry on residual stress distribution. *Journal of Materials Processing Technology*, vol. 207, pp. 211–221.

Song, K., Wei, Y., Dong, Z., Mac, R., Zhan, X., Zheng, W. and Fang, K. (2014). Constitutive model coupled with mechanical effect of volume change and transformation induced plasticity during solid phase transformation for ta15 alloy welding. *Applied Mathematical Modelling*.

Spoornet (1997). Specification for the supply of wrought wheels for tractive and trailing stock.

Suid-Afrikaanse Spoorpendelkorporasie Beperk (2000). *Handleiding vir Spoorbaanin-standhouding*.

TFR Chair in Railway Engineering (2015). *Introduction to Multi-Disciplinary Consepts in Railway Engineering*.

UIC 510-5 (2003). Technical approval of solid wheels.

Van der Hegge Zijnen, B.G. (1924). *Measurements of the velocity distribution in the boundary layer along a plane surface*. Ph.D. thesis, Delft.

Vasauskas, V., Bazaras, Z. and Capas, V. (2005). Strength anisotropy of railway wheels under contact load. *Mechanika*, vol. 51, pp. 31–38.

Vernersson, T. (2007*a*). Temperatures at railway tread braking. part 1: modelling. *Proceedings of the Institution of Mechanical Engineers, Part F: Journal of Rail and Rapid Transit*, vol. 221, pp. 167–182.

Vernersson, T. (2007*b*). Temperatures at railway tread braking. part 2: calibration and numerical examples. *Proceedings of the Institution of Mechanical Engineers, Part F: Journal of Rail and Rapid Transit*, vol. 221, pp. 429–442.

Vernersson, T. and Lunden, R. (2007). Temperatures at railway tread braking. part 3: wheel and block temperatures and the influence of rail chill. *Proceedings of the Institution of Mechanical Engineers, Part F: Journal of Rail and Rapid Transit*, vol. 221, pp. 443–454.

Vollebregt, E., Weidemann, C. and Kienberger, A. (2011). Use of "contact" in multi-body vehicle ddynamic and profile wear simulation: Initial results. In: *22nd International Symposium on Dynamics of Vehicles on Roads and Tracks*.

Vollebregt, E.A.H. (2013 September). *User guide for CONTACT, Vollebregt & Kalker's rolling and sliding contact model*. VORtech Computing, 13th edn.

Wheels World (2012). Metro wheel. Online.
Available at: `http://www.wheels-world.com/Wheels/?Show=Photos&AlbumID=5`